The Shape Synthesis of Non-Planar and Closely-Spaced Electrically-Small Conducting Surface Antennas

Anas Mohammad Ishaq Alakhras

Thesis submitted in partial fulfillment of the requirements for the
Doctorate in Philosophy degree
in Electrical and Computer Engineering

Ottawa-Carleton Institute for Electrical and Computer Engineering

School of Electrical Engineering and Computer Science

Faculty of Engineering

University of Ottawa

ABSTRACT

Antennas are needed in wireless communications of any kind and are key to the quality of any wireless link, irrespective of its use. There remains a need for electrically-small antennas that can fit on/in a restricted physical surface/volume for use in sensors (eg. Internet-of-Things) that need to "talk" to some data centre via the wireless network. The design issues associated with electrically-small antennas are well-known, and thus it will be appreciated that it would be advantageous to be able to design the above antennas in a way that exploits as much of the space allotted to them, as well the proximity of other objects present, to arrive at functioning antennas. Antennas of conventional shape do not necessarily do this. It might thus be best to perform a shape synthesis of an antenna that lets the electromagnetics decide on the shape of the final antenna in order to obtain the performance desired under the geometrical restrictions mentioned. Such shape synthesis has only been done for planar (2D) conducting surface antennas. In this thesis we develop the machinery for a computational electromagnetics-based tool capable of performing the shape synthesis of 3D conducting surface antennas for the first time. It has purposefully been developed in a way that allows it to capitalize on commercially available software for both the computational electromagnetics (CEM) and the genetic optimization algorithm (GA). A comprehensive 'shaping manager' software tool has been developed that controls the whole shaping process and communicates with the commercial software, in so doing implementing a desired shaping prescription. It is a complex tool whose development is based on a considerable amount of software engineering. The advantage of being able to utilize the commercial codes is that the work becomes accessible to others, such codes are more powerful and flexible than in-house codes, and they are also able to export files describing the complicated shaped geometries for fabrication. The shaping manager utilizes the characteristic mode concept so that one only needs to select the feed point once the shape synthesis has been completed. Fully 3D electrically-small conducting surface antenna examples are then successfully shape synthesized subject to various geometry restrictions. The validity of the modelling process is experimentally validated. The shape synthesis procedure is then extended to apply to the design of two closely-spaced electrically-small antennas operating at different frequencies, again with some experimental validation. Such shape synthesis has also not been done before. These procedures can be extended to the case where the two antennas in question are mounted on some electrically-large platform. However, if such platforms are electrically very large the full-wave computational burden may become prohibitive. We show that the characteristic modes for the antennas under shaping in such situations can in fact be found using hybrid method of moment / geometrical theory of diffraction (MM/GTD) methods, with only the antenna proper needing to be MM-meshed. An example is provided to demonstrate the computation of characteristic modes in this way. This possibility for characteristic mode computation has not yet been explicitly stated elsewhere (and so perhaps not realised), nor example computations provided. We believe this realisation might widen the scope of application of characteristic mode analysis.

Keywords:

Antenna shape synthesis, characteristic modes, sub-structure, perfect conductors, method of moments, geometrical theory of diffraction, electrically-small antennas.

Acknowledgements

I thank God for blessing me with the knowledge I have attained and I pray that my work be of benefit for those who come after me.

I am especially grateful to my supervisor, Professor Derek McNamara, for his support, guidance, advice, and many suggestions throughout the course of my research, and allowing me to liberally garner review material for Chapter 2 from the notes of the various courses he presents at the University of Ottawa.

In addition, I would like to thank my PhD Advisory Committee members for their insightful and constructive advice on my thesis proposal.

Finally, I am very grateful to my family (specially my father) for extending their patience, support and love to me. Without them, this work would never have come into existence.

TABLE OF CONTENTS

List of Figures

Glossary

Computational Electromagnetics (CEM)	Section 1.1
Antenna Shape Synthesis	Section 1.2
Electrically Small Antenna	Section 2.2.2
Far-Zone Fields & Radiation Patterns	Section 2.2.3
Bandwidth	Section 2.2.4
Input Reflection Coefficient	Section 2.2.5
Radiation Efficiency	Section 2.2.6
Directivity and Gain	Section 2.2.7
S-Parameters	Section 2.2.8
Mean Effective Gain (MEG)	Section 2.2.9
Electrically-Small Antenna Performance Measures	Section 2.2.10
Electric Field Integral Equation Model	Section 2.3.2
Method of Moment (MoM) Solution of an Integral Equation (IE)	Section 2.3.3
Expansion Functions	Section 2.3.4
Hybrid Moment-Method / Geometrical-Theory-of-Diffraction (MM-GTD) Methods	Section 2.3.5
Characteristic Modes	Section 2.4
Sub-structure Characteristic Modes	Section 2.4.3
Optimization Algorithms	Section 2.5
Antenna Shape Synthesis Techniques	Section 2.6

List of Tables

List of Acronyms

1D	One-Dimensional
3D	Three-Dimensional
EFIE	Electric-Field Integral Equation
IE	Integral Equation
MS	Modal Significance
TE	Transverse Electric
CEM	Computational Electromagnetic
CM	Characteristic Mode
DMM	Direct Matrix Manipulation
ESA	Electrically Small Antenna
GA	Genetic Algorithm
MIMO	Multiple-input Multiple-output
MOM	Method of Moments
PEC	Perfect Electrical Conductor
RWG	Rao-Wilton-Glisson expansion functions
UWB	Ultrawideband
VNA	Vector Network Analyzer
MED	Mean Effective Directivity
MEG	Mean Effective Gain
AoA	Angle-of-Arrival
PAS	Power Angular Spectrum
XPR	Cross-Polarisation Ratio
Q	Quality Factor
VSWR	Voltage Standing Wave Ratio
GTD	Geometrical Theory of Diffraction
MM-GTD	Moment-Method / Geometrical-Theory-of-Diffraction
ASCII	American Standard Code for Information Interchange

List of Symbols

P_{inc}	Incident Power
P_{refl}	Reflected Power
P_{in}	Accepted Power
P_{rad}	Radiated Power
P_{loss}	Power Losses
f	Frequency
f_L	Upper Frequency
f_U	Lower Frequency
a	Spherical Volume Radius
λ	Wavelength
k	Wavenumber
$\bar{E}$	Electric Field
$\bar{H}$	Magnetic Field
$\bar{S}$	Time-Averaged Power Density
$\bar{r}$	Observation Point
η_o	Free-Space Intrinsic Impedance
μ_o	Permeability
ε_o	Permittivity
U	Radiation Intensity
Δf	Absolute Bandwidth
f_o	Self-Resonant Frequency
Γ_{in}	Input Reflection Coefficient
Z_{in}	Input Impedance
Z_o	Characteristic Impedance
R_{in}	Input Resistance
X_{in}	Input Reactance
R_{rad}	Radiated Power
R_{loss}	Power Dissipated
η_{rad}	Radiation Efficiency
D	Directivity
G	Gain
$G_{realized}$	Realized Gain
$[Z]$	Impedance Matrix
$[S]$	Scattering Matrix
G_θ	Partial Gain
$\mathscr{P}_\theta$	Angular Power Density Function

$\mathscr{P}_{\phi}$	Angular Power Density Function
Q	Quality Factor
λ_1	Eigenvalue of Mode#1
Q_z	Quality Factor Estimated from the Frequency Derivative of the Input Impedance
σ	Conductivity
S_c	Surface of the Scatterer
$\bar{E}_{\tan}^{scat}$	Scattered Field
$\bar{J}^{imp}$	Impressed Electric Source Current Densities
$\bar{M}^{imp}$	Impressed Magnetic Current Densities
$\bar{J}_s$	Electric Surface Current Density
$\mathbb{G}$	Kernel (Green's Function)
$f_n(z)$	Expansion Functions
$\Psi_n(z)$	z-Dependent Function
$\left[V^{inc}\right]$	Incident Voltage
$\mathbb{G}^{fs}$	Green's Function In Free Space
λ_n	CM Eigenvalues
$[J_n]$	CM Eigenvectors (Eigencurrents)
$[R]$	Real Part of the Impedance Matrix
$[X]$	Imaginary Part of the Impedance Matrix
δ_{mn}	Kronecker Delta
α_n	Weighting Coefficient
$\bar{E}_n$	Eigenfield
MS	Modal Significance Factor
λ_n^{sub}	Sub-Structure CMs
$[J_n^{Asub}]$	Sub-Structure Eigencurrents
N_{pop}	Population Size
F_{obj}	Objective Function
N_{gen}	Number of Generations
N_{bit}	Number of Bits in a Chromosome
N_{Δ}	Number of Triangles in the Mesh
$.out$	FEKO Output File
$.cfm$	FEKO Geometry File
N_{dof}	Number of Expansion Functions
C_{init}	Initial Chromosome
$B\eta_{rad}$	Bandwidth-Efficiency Product

CHAPTER 1

Introduction

1.1 ANTENNA DESIGN

Prior to the availability of computational electromagnetics (CEM), antenna analysis had severe limitations. The quantity that dictates the form of the radiation pattern, namely the current distribution on the antenna, had to be approximated, and input reflection coefficients at the antenna terminals could not be calculated accurately. No doubt this hampered design innovation on the antenna front; but then the constraints on the antenna design (eg. amount of room allocated for the antenna; the bandwidth required of the antenna; and so on) were often not prohibitive and quite standard antenna shapes were useable and so communications system development as a whole was not hampered. The availability of CEM changed the way antennas are designed, and commercial CEM software arrived on the scene in a timely manner just when wireless communications began to boom, and demands for improved antennas increased, along with constraints on the real estate they may occupy. CEM analysis now allows us to actually compute the current distributions on antennas no matter what their shape, and hence also find their port properties more accurately than was previously the case. We need no longer only use a straight wire dipole or circular loop. During the design process we can bend it to fit on some device and accurately determine what the performance consequences are. We can determine what the effect of the chassis (or platform) is, on which the antenna is mounted. And much more. This ability has moved antenna design into the domain of most RF designers who work on other RF “circuit” aspects, and creativity has flourished. The rapid expansion of what can be done wirelessly is proof of this. However, by nature engineers always “push the envelope”, and so antenna topics remain that are in need of research.

1.2 ANTENNA SYNTHESIS

Antennas are essential in all wireless communications, being key to the quality of any radio link, irrespective of its use. Transmitting antennas transform electrical signals in a transmitter into an electromagnetic wave that is radiated into space. Similarly, receiving antennas capture power from incident electromagnetic waves and deliver the induced electrical signals to a receiver. In most cases the same antenna is used for transmitting and receiving. Depending on the application, an antenna may take one of several different geometrical forms. Widely-used handbooks [VOLA 07], [BALA 08] discuss conducting wire geometries, slot radiators, patch radiators, dielectric resonator antennas, and horn radiators, for low (broad radiation patterns) or medium directivity performance[1]. If high directivity (narrow radiation pattern) is needed and cannot be achieved using the above-mentioned antenna types, engineers then use a properly shaped reflector (or reflectarray), or a lens-like arrangement (or transmitarray), with one of the above-mentioned antennas used as a feed radiator to illuminate the reflector or lens. Or several of the above-mentioned radiators (in which case they are called radiating elements) are correctly arranged in space to form an array antenna.

The shape synthesis approach in antenna design is to not select a particular antenna geometry beforehand, but to "let the electromagnetics tell us what the shape must be". This is a tall order. We are rightfully[2] warned that the ideal antenna synthesis procedure would allow one to "start with a set of electrical, mechanical, and system specifications that would lead to a particular antenna together with its specific geometry and material specification", but that "this ideal general antenna synthesis method does not exist". Nevertheless, progress in antenna shape synthesis has been made[3]. In order to clarify what we mean by shape synthesis, we can group antenna design optimization approaches as follows:

■ Excitation optimization: This includes the determination of the complex excitations of an array of known radiating elements required to provide some desired radiation pattern performance, usually called array pattern synthesis.

■ Size optimization: This is essentially the adjustment of the values of a pre-determined set of feature dimensions with the feature shapes determined from physical insight and experience. The majority of antenna design procedures fall into this category; it has been very successful.

■ Shape optimization: In this category the shape of the final antenna structure is an outcome of the synthesis process, although there is usually some starting structure that is perturbed by the synthesis procedure to result in the final antenna shape. It is already used for microstrip and wire antennas, with only the conductor geometry undergoing shaping through the removal or retention of conducting pixels/segments into which the

---

[1] The most important antenna performance indices are reviewed in Section 2.2.

[2] W.Stutzman and S.Licul, "Synthesis Methods for Antennas" in C.A.Balanis (Edit.), *Modern Antenna Handbook* (Wiley, 2008).

[3] This is reviewed in Section 2.6.

starting shape is divided. It will be reviewed in Section 2.6. This approach is related to topology optimisation in structural engineering4 (where it has been used for some years), and inverse design in photonics (where its use appears to be relatively recent). In the antenna field it includes shaping of planar elements for frequency selective surfaces and reflectarrays.

■ Material optimization: In this technique a rectangular parallelepiped starting shape is divided into voxels, each of whose material properties can individually be selected (during the shaping process) to be conducting or consist of dielectric/magnetic material. This resembles the inverse design methods that are coming into use in the photonics area.

The goal of the shape synthesis methods to be developed in this thesis is not to ‘break existing performance records’ of antennas designed by more standard approaches. Instead, the aim is to extend, to a wider range of problems, those methods that begin with some “starting shape” and then through automated shaping arrive at an antenna that has some desired performance, subject constraints both on the electrical performance and on the space the final antenna may occupy.

1.3 SUMMARY OF THE CONTRIBUTIONS OF THE THESIS

The principal contributions of this thesis are as follows:

■ The development of a computational tool for the shape synthesis of three-dimensional conducting antennas. This has previously not been available.

■ Use of the tool for the shape synthesis of 3D conducting electrically small antennas using a “shape-first feed-next” approach. This is the first time that characteristic mode concepts have been utilized in this way to shape synthesize 3D conducting surface antennas (with constraints on the surface/volume that may be occupied), and that directivity-related requirements have been incorporated into such an approach by expressing mean effective directivity in terms of characteristic mode quantities.

■ Use of the tool for the shape synthesis of closely-spaced antennas that operate at two different frequencies, using sub-structure characteristic modes to permit a “shape-first feed-next” approach. This sort of shape synthesis has previously not been reported elsewhere.

---

[4] But the pixelation approach is not used there.

■ Demonstration of sub-structure characteristic mode computation using a field-based hybrid MM/GTD method. This does not yet appear to have been explicitly stated elsewhere (and so perhaps not realised), nor example computations provided.

1.4 OVERVIEW OF THE THESIS

The research described in this thesis lies in the area of antenna shape synthesis. It deals exclusively with the shape synthesis of antennas whose principal radiation mechanism is an electric current density on conducting surfaces[5].

Chapter 2 assembles the key technical concepts that are needed to conduct the research described in the thesis, and upon which it builds. This includes the definition of antenna performance measures, as well as reviews of the method of moments for radiation/scattering from conducting objects, characteristic mode concepts, and (briefly) the optimization methods available, in particular that used in this thesis. We also recognize and review what has been achieved by others on the topic of the shape synthesis of conducting antennas, and clarify some aspects that we believe have not yet been adequately dealt with in the literature.

Chapter 3 describes the development of the computational tool that permits one to perform certain types of antenna shape syntheses for the first time. This development is thus, in its own right, an important contribution. A chapter of this sort might be found to be a rather tedious one, but is necessary from the standpoint of a reader who might want to repeat this work. It will also serve to remove any vagueness as to exactly how things are done in the remaining chapters, and indeed allow descriptions in the remaining chapters to be more concise and to the point. Importantly, it establishes a structured way to use the multitude of parameter settings when using the GA in antenna shaping.

Chapters 4 and 5 describe two classes of shape synthesis problem. Chapter 4 demonstrates the implementation of the shape synthesis process for fully 3D conducting surface structures. Chapter 5 considers the shape synthesis of conducting surface antennas that operate in each other's presence, at different frequencies. Both these classes of shape synthesis problem are being described here for the first time. Chapter 6 contributes to the theory of sub-structure characteristic modes by demonstrating how these

---

[5] Thus, for example, we do not consider dielectric resonator antennas (DRAs), whose principal radiation mechanism (for non-hybrid DRAs at least) is electric polarisation current in the dielectric material.

can be found using field-based hybrid methods. This would allow characteristic mode based shape synthesis methods to be used even when the antenna’s platform is electrically too large (for even reasonable high-performance computing facilities) to be completely modelled using the method of moments.

Finally, some general conclusions are drawn in Chapter 7, and the research reported in the thesis put into perspective.

CHAPTER 2

Review of Key Background Concepts & Techniques

2.1 INTRODUCTION

We are interested in the shape synthesis of antennas that are electrically-small[6] or of intermediate size. In order to place the work of this thesis in the context of previous works on the topic, and so to demonstrate that it has made measurable contributions to the field, a review of the state of the art of such shape synthesis is necessary. This is provided in Section 2.6. Before this can be done with clarity, it is necessary to first summarize the computational electromagnetics methods that have been used; this is done in Section 2.3. As mentioned in Chapter 1, computational electromagnetics provides superb tools for antenna analysis. The source densities and electromagnetic fields from such modelling incorporate all the physics associated with a particular configuration. The difficulty is to extract and exploit the "hidden information" in the solutions presently not always used to the full. The characteristic mode analysis of a structure, which is found using computational electromagnetics modelling, will be used in this thesis as a way of doing this, and so is reviewed in Section 2.4. The shaping tool to be developed in the thesis needs to use some optimization algorithms, and so these are briefly put in context in Section 2.5. Section 2.2 defines the essential antenna performance measures that will be used in the thesis. Section 2.7 concludes the chapter with a summary of shape synthesis problems for electrically small antennas that have not been adequately dealt with in the literature, and which form the subject of this thesis.

2.2 ANTENNA PERFORMANCE MEASURES

2.2.1 Introductory Comments

Antennas form the transducers between the electrical signals in the circuitry of transmitters and receivers, and the electromagnetic waves (in the surrounding space) that are radiated or absorbed, respectively. Any antenna has a set of terminals (a port) at which the desired signals are input (in the transmitting situation) or extracted (in the receiving situation). Fig.2.2-1(a) shows a transmission line that connects an antenna to the

---

[6] By which is meant those whose dimensions are a fraction of the free space wavelength at the operating frequency.

transmitter[7]. A certain amount of power P_{inc} is incident on the antenna terminals. Due to mismatch between the transmission line and the antenna some of this power P_{refl} is reflected back towards the transmitter while the remainder P_{in} is accepted by the antenna (i.e. actually enters the antenna terminals). Thus we have

$$P_{in} = P_{inc} - P_{refl} \tag{2.2-1}$$

Of the power (2.2-1), a portion P_{loss} is dissipated on the antenna structure due to material losses, and the rest P_{rad} is radiated. In other words

$$P_{rad} = P_{in} - P_{loss} \tag{2.2-2}$$

The antenna designer's task, for a given P_{inc}, is to maximize P_{rad} by minimizing P_{refl} and P_{loss}. In addition, the antenna is normally required to radiate most of P_{rad} in preferred directions. The electromagnetic wave transporting P_{rad} is in many cases also required to be of a certain polarization. And all the above requirements must be met at frequencies f over a specific frequency band $f_L \le f \le f_U$ between lower frequency f_L and upper frequency f_U. In order to minimize P_{refl} it is often necessary to use a matching network between the transmission line and the radiator, as shown in Fig.2.2-1(b). The antenna then consists of the radiator plus the matching network, and P_{loss} then consists of losses in the matching network[8] *and* the radiator.

---

[7] As is often the case, we will always discuss antennas as if they are transmitting. All of the antennas in this thesis are composed of isotropic linear materials, and so the performance in the receiving situation will always be the same as in the transmitting (that is, reciprocity holds).

[8] Because the matching network must be considered part of the antenna.

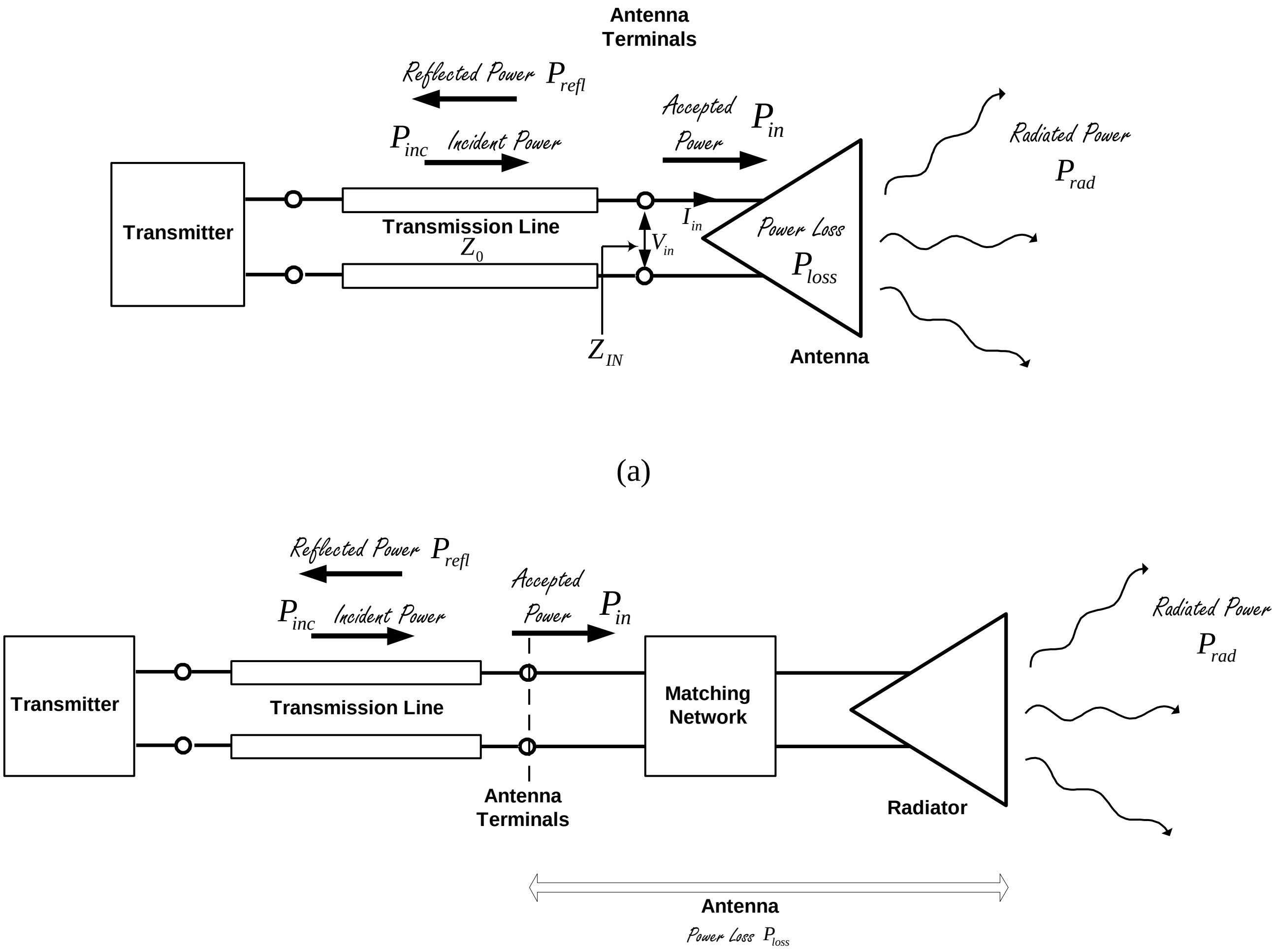

(a)

(b)

Fig.2.2-1 : Power budget for an antenna without (a), and with (b), a matching network. (After [MCNA 17])

2.2.2 Antenna Electrical Size Classification

As originally defined by Wheeler [WHEE 47], an electrically small antenna is any antenna that fits within a spherical volume with radius a less than $\lambda/2\pi$, or as Wheeler stated it, any antenna that can fit within the radiansphere. This can be stated as

$$a < \frac{\lambda}{2\pi} \tag{2.2-3}$$

Recalling that the free space wavenumber $k = 2\pi / \lambda$, this can be rewritten as the condition[9]

---

[9] Some prefer to define an electrically small antenna to be one for which $ka < 0.5$, but we will use the more common (2.2-4).

$$ka < 1 \tag{2.2-4}$$

The properties of electrically small antennas are restrictive : narrow bandwidth, low radiation efficiency, high reactive energies, and small radiation resistance. The design of electrically small antennas centres around trying to overcome these properties. A half-wavelength dipole has $ka = 1.57$, and is not considered to be electrically small. Further discussion on electrically small antennas will follow in Section 2.2.10 after the various antenna performance metrics mentioned above have been defined.

2.2.3 Far-Zone Fields & Radiation Patterns

Any electromagnetic field, and hence the electromagnetic field of *any* antenna can be written (with respect to the chosen coordinate origin) as

$$\bar{E}(r,\theta,\phi) = E_\theta(r,\theta,\phi)\,\hat{\theta} + E_\phi(r,\theta,\phi)\,\hat{\phi} + E_r(r,\theta,\phi)\,\hat{r} \tag{2.2-5}$$

and

$$\bar{H}(r,\theta,\phi) = H_\theta(r,\theta,\phi)\,\hat{\theta} + H_\phi(r,\theta,\phi)\,\hat{\phi} + H_r(r,\theta,\phi)\,\hat{r} \tag{2.2-6}$$

where (r,θ,ϕ) specifies an observation point in the three-dimensional space surrounding the antenna. The pair of angles (θ,ϕ) gives the direction of the observation point and r its distance from the origin of the coordinate system. The first two components in each of the above expressions are the *transverse* components of the antenna's electromagnetic field. The last component in each of (2.2-3) and (2.2-4), namely $E_r(r,\theta,\phi)$ and $H_r(r,\theta,\phi)$, are the *radial* components of the electromagnetic field. The magnetic field $\bar{H}(r,\theta,\phi)$ can be found from $\bar{E}(r,\theta,\phi)$ using Maxwell's equations, and vice versa.

The time-averaged power density at any point (r,θ,ϕ), at which the antenna fields are $\bar{E}(r,\theta,\phi)$ and $\bar{H}(r,\theta,\phi)$, is given by the (time-averaged) Poynting vector

$$\bar{S}(r,\theta,\phi) = ½\ \mathrm{Re}\left\{ \bar{E}(r,\theta,\phi) \times \bar{H}^*(r,\theta,\phi) \right\} \tag{2.2-7}$$

and is measured in Watts/metre^2. If we think of an imaginary spherical surface S_{ant} that encloses the antenna entirely, as illustrated in Fig.2.2-2, then the time-averaged power (in Watts) passing through surface S_{ANT} is given from Poynting's theorem as the integral of $\bar{S}(r,\theta,\phi)$ over the closed surface S_{ANT}, namely

$$P_{rad} = \oiint_{S_{ANT}} \bar{S}(r,\theta,\phi)\cdot\overline{dS} = \oiint_{S_{ANT}} \bar{S}(r,\theta,\phi)\cdot\hat{r}dS = \int_0^{2\pi}\int_0^{\pi}\left\{\bar{S}(r,\theta,\phi)\cdot\hat{r}\right\} r^2\sin\theta\, d\theta\, d\phi \qquad (2.2\text{-}8)$$

The physical space around an antenna (in fact this is all of space) can be broadly classified as the *near-zone*[10] in the immediate vicinity of the antenna where the variation of the fields with observation point $\bar{r} = (r,\theta,\phi)$ is very complicated and sensitive to the geometrical details of the structure, and the *far-zone* region that is distant from the antenna. In the far-zone region the fields are found to have the following properties:

▪ The *radial* components of the fields (namely E_r and H_r) are negligible compared to the transverse components, so that we can assume

$$E_r(r,\theta,\phi) = \hat{r}\cdot\bar{E}(r,\theta,\phi) \approx 0 \qquad (2.2\text{-}9)$$

and

$$H_r(r,\theta,\phi) = \hat{r}\cdot\bar{H}(r,\theta,\phi) \approx 0 \qquad (2.2\text{-}10)$$

▪ The components of the *transverse* fields take the forms

$$E_\theta(r,\theta,\phi) = F_\theta(\theta,\phi)\frac{e^{-jkr}}{r} \qquad (2.2\text{-}11)$$

and

$$E_\phi(r,\theta,\phi) = F_\phi(\theta,\phi)\frac{e^{-jkr}}{r} \qquad (2.2\text{-}12)$$

so that the transverse electric field as a whole is

$$\bar{E}(r,\theta,\phi) = \bar{F}(\theta,\phi)\,\frac{e^{-jkr}}{r} \qquad (2.2\text{-}13)$$

with

$$\bar{F}(\theta,\phi) = F_\theta(\theta,\phi)\hat{\theta} + F_\phi(\theta,\phi)\hat{\phi} \qquad (2.2\text{-}14)$$

▪ In other words, in the far-zone region the fields decay as $1/r$. If we set E_r and H_r to zero, then from the Maxwell curl equations we find that the electric and magnetic fields *in the far-zone of an antenna* are related through

$$\bar{H}(r,\theta,\phi) = \frac{1}{\eta_o}\hat{r}\times\bar{E}(r,\theta,\phi) = \frac{1}{\eta_o}\,\hat{r}\times\bar{F}(\theta,\phi)\frac{e^{-jkr}}{r} \qquad (2.2\text{-}15)$$

---

[10] Some prefer to divide this near-zone region into the reactive near-zone region, and the radiating near-zone region (also called the Fresnel region). The far-zone region is also called the Fraunhofer region.

with $\eta_o = \sqrt{\mu_o / \varepsilon_o}$. The result is that, in the far-zone, expression (2.2-7) becomes

$$\bar{S}(r,\theta,\phi) = S(r,\theta,\phi)\ \hat{r} \tag{2.2-16}$$

The radiation intensity $U(\theta,\phi)$ of an antenna, in a specific direction (θ,ϕ) is defined by the IEEE as the power radiated from the antenna per unit solid angle in that direction. Radiation intensity is a far-zone quantity, as emphasised by the fact that it is purposefully denoted as a function of the angular coordinates θ and ϕ only. The relation between the radiation intensity and the far-zone power density is simply

$$U(\theta,\phi) = r^2\ S(r,\theta,\phi) \tag{2.2-17}$$

Note that although $S(r,\theta,\phi)$ is a function of r, in the far-zone its r-dependence is always the $1/r^2$ decay, and hence the radiation intensity $U(\theta,\phi)$ is indeed independent of r, being

$$U(\theta,\phi) = \frac{\left|\bar{F}(\theta,\phi)\right|^2}{2\eta_o} \tag{2.2-18}$$

Graphical representations of $U(\theta,\phi)$ are represented in either polar or rectangular form. The radiation intensity is usually maximum in some direction, say (θ_o,ϕ_o), and the radiation pattern is most often plotted in deciBels in normalised form, namely

$$U_{dB}(\theta,\phi) = 10\log\left\{\frac{\left|\bar{F}(\theta,\phi)\right|^2}{\left|\bar{F}(\theta_o,\phi_o)\right|^2}\right\} = 20\log\left\{\frac{\left|\bar{F}(\theta,\phi)\right|}{\left|\bar{F}(\theta_o,\phi_o)\right|}\right\} = 20\log\left\{\left|\bar{F}_N(\theta,\phi)\right|\right\} = \left|\bar{F}_N(\theta,\phi)\right|_{dB} \tag{2.2-19}$$

This is usually called the radiation pattern of the antenna.

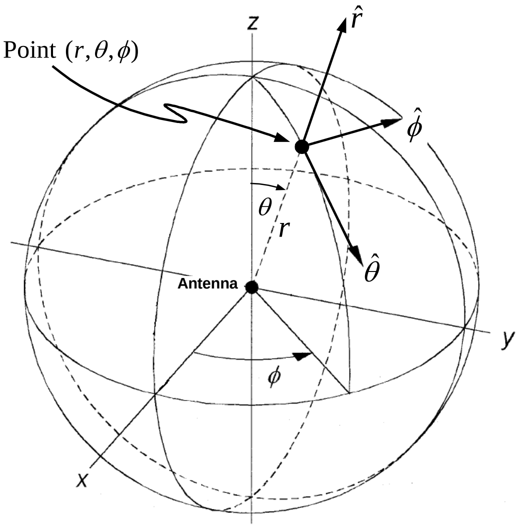

Fig.2.2-2 : Spherical coordinate system (After [MCNA17])

2.2.4 Fractional Bandwidth

The bandwidth of an antenna is defined as the range of frequencies within which the performance of the antenna, with respect to some characteristic, conforms to a specified standard. The bandwidth can be considered to be the range of frequencies, from lower frequency f_L to upper frequency f_U, namely $f_L \leq f \leq f_U$ on either side of some center frequency f_o, over which the required antenna characteristics are within acceptable values. The various characteristics of an antenna will not necessarily have the same frequency dependence. For instance, the input reflection coefficient might be within acceptable values over a smaller frequency range than are the sidelobe levels. Thus there is no unique definition for bandwidth. We can talk about the impedance bandwidth (also referred to as the reflection coefficient bandwidth), the pattern bandwidth, and so forth. If an antenna satisfies a required set of specifications over the frequency band

$$\Delta f = f_U - f_L \tag{2.2-20}$$

the quantity Δf is called the *absolute bandwidth*. Given the above absolute bandwidth, the *center-frequency* is

$$f_o = f_L + \frac{\Delta f}{2} = \frac{1}{2}\left(f_U + f_L \right) \tag{2.2-21}$$

All the above quantities are of course measured in Hertz (Hz). The *fractional bandwidth* of the antenna is defined as

$$Fractional\ Bandwith = \frac{\Delta f}{f_o} \qquad (2.2\text{-}22)$$

It is dimensionless and usually expressed as a percentage.

2.2.5 Input Reflection Coefficient of an Isolated Antenna

Consider once more the set-up shown in Fig.2.2-1(a), which shows an antenna of input impedance Z_{in} fed by a transmission line of characteristic impedance Z_o. The reflection coefficient at the antenna input terminals is

$$\Gamma_{in} = \frac{Z_{in} - Z_o}{Z_{in} + Z_o} \qquad (2.2\text{-}23)$$

Denoting the power *incident* at the antenna terminals by P_{inc}, the power actually *accepted* by the antenna is

$$P_{in} = \left\{ 1 - |\Gamma_{IN}|^2 \right\} P_{inc} \qquad (2.2\text{-}24)$$

At any frequency ω we have an input impedance

$$Z_{in}(\omega) = R_{in}(\omega) + jX_{in}(\omega) \qquad (2.2\text{-}25)$$

Resistance $R_{in}(\omega)$ models the energy that is input from the source and is not returned to the source. In the case of the antenna it thus represents two physical effects, namely power that is radiated by the antenna and power that is dissipated on the antenna structure itself. We can write

$$R_{in}(\omega) = R_{rad}(\omega) + R_{loss}(\omega) \qquad (2.2\text{-}26)$$

The portion R_{rad} models the radiated power, and $R_{loss}(\omega)$ the power dissipated (eg. Ohmic loss in conducting material; dielectric loss in printed circuit substrates, and so on). We have purposefully shown the frequency dependence explicitly to emphasise the fact that the values of these quantities are not the same at all frequencies of interest[11].

If $X_{in}(\omega_o) \approx 0$ without the need for a matching network we say the antenna is self-resonant at $\omega_o = 2\pi f_o$. If an antenna is self-resonant, the matching network can often be dispensed with or need be of a much simpler design (an impedance transformer).

2.2.6 Radiation Efficiency

The *radiation efficiency* of an antenna is defined as the ratio of the total power radiated by the antenna to the power accepted by the antenna from the connected transmission line, namely

---

[11] In what follows we will not always show this frequency dependence explicitly, but it should always be kept in mind.

$$\eta_{\text{rad}} = \frac{P_{\text{rad}}}{P_{\text{in}}} \tag{2.2-27}$$

It follows that we can rewrite this as

$$\eta_{\text{rad}} = \frac{P_{\text{rad}}}{P_{\text{rad}} + P_{\text{loss}}} = \frac{R_{\text{RAD}}}{R_{\text{RAD}} + R_{\text{LOSS}}} \tag{2.2-28}$$

We observe that η_{rad} is not affected by Γ_{in}. However, the quantity $\left(1-\left|\Gamma_{in}\right|^2\right)\eta_{\text{rad}}$ is sometimes referred to as the "total radiation efficiency".

2.2.7 Directivity and Gain

A. Directivity

It is usually desired that an antenna increase the amount of radiation in particular directions and minimise it in others. A measure of the ability of an antenna to do this is its *directivity*. The directivity[12] D(θ,ϕ) of an antenna in direction (θ,ϕ) is officially defined as

$$D(\theta,\phi) = \frac{\text{Radiation Intensity in Direction } (\theta,\phi)}{\text{Spatially Averaged Radiation Intensity}} \tag{2.2-29}$$

Hence it follows that we can express directivity as

$$D(\theta\,,\phi) = \frac{4\pi\, U(\theta\,,\phi)}{P_{rad}} \tag{2.2-30}$$

where P_{rad} the total power *radiated* by the antenna, as described in Section 2.2.1. Directivity is typically expressed in deciBels, namely

$$D^{dBi}(\theta,\varphi) = 10\log\left\{D(\theta,\varphi)\right\} \tag{2.2-31}$$

It is said to be in dBi, the "i" standing for "isotropic radiator". An isotropic radiator is a non-physical radiator that radiates equally well in all directions. If it were physically possible to make such an antenna its directivity would be 1, and so we imagine any directivity as being measured relative to it.

Due to (2.2-16) and (2.2-17), the expression for the power radiated by an antenna can be shown to be

$$P_{\text{rad}} = \frac{1}{2\eta_o}\int_0^{2\pi}\int_0^{\pi} U(\theta,\phi)\; r^2 \sin\theta \; d\theta\, d\phi \tag{2.2-32}$$

---

[12] Also called the *total* directivity.

If we write

$$U_\theta(\theta,\phi) = \frac{\left|E_\theta(\theta,\phi)\right|^2}{2\eta_o} \tag{2.2-33}$$

and

$$U_\phi(\theta,\phi) = \frac{\left|E_\phi(\theta,\phi)\right|^2}{2\eta_o} \tag{2.2-34}$$

we can define associated partial directivities

$$D_\theta(\theta\,,\phi) = \frac{4\pi\, U_\theta(\theta\,,\phi)}{P_{rad}} \tag{2.2-35}$$

and

$$D_\phi(\theta\,,\phi) = \frac{4\pi\, U_\phi(\theta\,,\phi)}{P_{rad}} \tag{2.2-36}$$

Due to the way these are defined, we of course have

$$D(\theta\,,\phi) = D_\theta(\theta\,,\phi) + D_\phi(\theta\,,\phi) \tag{2.2-37}$$

and also

$$\int_0^{2\pi}\int_0^{\pi} \left\{ D_\theta(\theta,\phi) + D_\phi(\theta,\phi) \right\} \sin\theta \; d\theta\, d\phi = 4\pi \tag{2.2-38}$$

B. Gain

The gain of an antenna is related to the directivity as

$$G(\theta,\phi) = \eta_{\mathrm{rad}} D(\theta,\phi) \tag{2.2-39}$$

The *realized* gain of the antenna is defined as

$$G_{realized}(\theta,\phi) = \left(1 - \left|\Gamma_{in}\right|^2\right)\eta_{\mathrm{rad}} D(\theta,\phi) \tag{2.2-40}$$

Similarly, we have the partial gains $G_\theta(\theta,\phi) = \eta_{\mathrm{rad}} D_\theta(\theta,\phi)$ and $G_\phi(\theta,\phi) = \eta_{\mathrm{rad}} D_\phi(\theta,\phi)$, and the associated *realized* partial gains of the antenna are defined as $\left(1 - \left|\Gamma_{in}\right|^2\right)\eta_{\mathrm{rad}} D_\theta(\theta,\phi)$ and $\left(1 - \left|\Gamma_{in}\right|^2\right)\eta_{\mathrm{rad}} D_\phi(\theta,\phi)$.

2.2.8 Mutual Coupling Between Two Antennas

Any two antennas can be regarded as a two-port network, in terms of voltages and current defined at the ports of the two antennas, as indicated in Fig.2.2-3. If we number the ports as #1 and #2 as shown, these are related as

$$V_1 = Z_{11}I_1 + Z_{12}I_2 \tag{2.2-41}$$

and

$$V_2 = Z_{21}I_1 + Z_{22}I_2 \tag{2.2-42}$$

These apply no matter how the 2-port network is excited. The access transmission lines are only shown for emphasis. The characteristic impedances Z_{01} and Z_{02} are assumed to be real. The elements Z_{ij} of the impedance matrix $[Z]$ of the two-port are defined by the relations

$$Z_{11} = \left.\frac{V_1}{I_1}\right|_{I_2=0} \qquad Z_{12} = \left.\frac{V_1}{I_2}\right|_{I_1=0} \qquad Z_{21} = \left.\frac{V_2}{I_1}\right|_{I_2=0} \qquad Z_{22} = \left.\frac{V_2}{I_2}\right|_{I_1=0} \tag{2.2-43}$$

The input impedance of antenna#1 in the presence of antenna#2 is

$$Z_{\text{in}}^{(1)} = \left.\frac{V_1}{I_1}\right|_{Z_{L2}} \tag{2.2-44}$$

where Z_{L2} is the load placed at the terminals of antenna#2, and similarly

$$Z_{\text{in}}^{(2)} = \left.\frac{V_2}{I_2}\right|_{Z_{L1}} \tag{2.2-45}$$

Normally, Z_{L1} and Z_{L2} are the reference impedances. Impedance matrix $[Z]$ is related to the scattering matrix $[S]$ of the two-port by

$$S_{11} = \frac{(Z_{11} - Z_{01})(Z_{22} + Z_{02}) - Z_{12}Z_{21}}{(Z_{11} + Z_{01})(Z_{22} + Z_{02}) - Z_{12}Z_{21}} \qquad S_{12} = \frac{2Z_{12}\sqrt{Z_{01}Z_{02}}}{(Z_{11} + Z_{01})(Z_{22} + Z_{02}) - Z_{12}Z_{21}}$$

(2.2-46)

$$S_{21} = \frac{2Z_{21}\sqrt{Z_{01}Z_{02}}}{(Z_{11} + Z_{01})(Z_{22} + Z_{02}) - Z_{12}Z_{21}} \qquad S_{22} = \frac{(Z_{11} + Z_{01})(Z_{22} - Z_{02}) - Z_{12}Z_{21}}{(Z_{11} + Z_{01})(Z_{22} + Z_{02}) - Z_{12}Z_{21}}$$

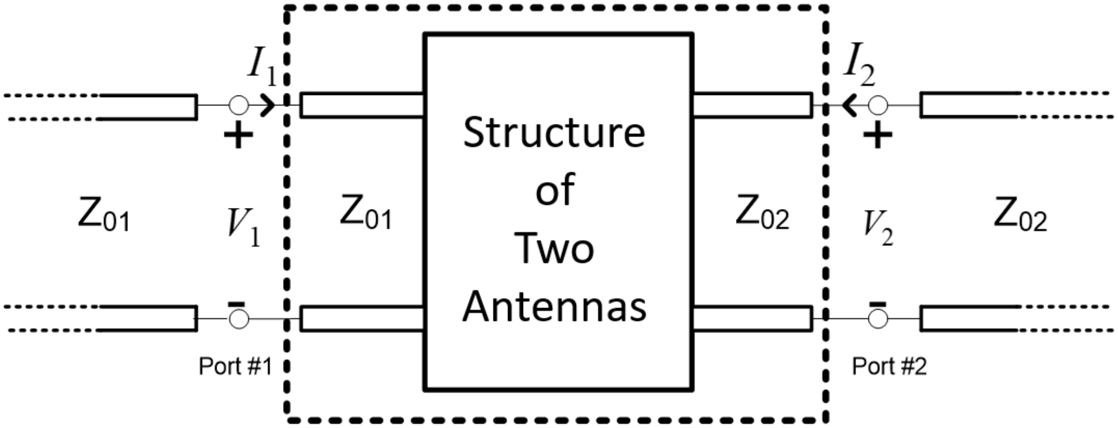

Fig.2.2-3 : Two-port network representation of two coupled antennas (After [MCNA17])

2.2.9 Mean Effective Gain (MEG)

The sensors we will refer to in Section 4.1 will, like mobile devices, usually be surrounded by scattering objects that are physically spread over a wide range of angles around the device. The question that arose in early wireless systems work was what value of antenna gain was to be used when calculating link budgets in such circumstances. The concept of a mean effective gain (MEG) was therefore introduced and defined in [TAGA90] to be

$$MEG = \int_0^{2\pi}\int_0^{\pi} \left\{ \frac{XPR}{1+XPR} G_\theta(\theta,\phi)\mathscr{P}_\theta(\theta,\phi) + \frac{1}{1+XPR} G_\phi(\theta,\phi)\mathscr{P}_\phi(\theta,\phi) \right\} \sin\theta \, d\theta d\phi \tag{2.2-47}$$

Terms $G_\theta(\theta,\phi)$ and $G_\phi(\theta,\phi)$ are the partial gains defined in Section 2.2.7. The other terms will be explained below. Clearly, if we wish to show radiation efficiency explicitly, this can be written as

$$MEG = \eta_{\text{rad}} \int_0^{2\pi}\int_0^{\pi} \left\{ \frac{XPR}{1+XPR} D_\theta(\theta,\phi)\mathscr{P}_\theta(\theta,\phi) + \frac{1}{1+XPR} D_\phi(\theta,\phi)\mathscr{P}_\phi(\theta,\phi) \right\} \sin\theta \, d\theta d\phi \tag{2.2-48}$$

Some authors interpret $G_\theta(\theta,\phi)$ and $G_\phi(\theta,\phi)$ as the *realized* partial gains[13] of the antenna, and in this case we would need to write (2.2-48)

$$MEG = \left(1-\left|\Gamma_{in}\right|^2\right)\eta_{\text{rad}}\int_0^{2\pi}\int_0^{\pi}\left\{\frac{XPR}{1+XPR}D_\theta(\theta,\phi)\mathscr{P}_\theta(\theta,\phi)+\frac{1}{1+XPR}D_\phi(\theta,\phi)\mathscr{P}_\phi(\theta,\phi)\right\}\sin\theta\, d\theta d\phi \quad (2.2\text{-}49)$$

Of course, if the antenna is well matched then the 'mismatch loss' $1-\left|\Gamma_{in}\right|^2$ will be almost unity anyway. The terms in the expressions for the MEG are discussed in [KILD 07], [SAUN 08], [HUAN 08], [DOUG 98] and [KALL 02]. These can be summarized as follows:

■ XPR is known as the cross-polarisation[14] ratio of the wireless environment (or channel). It is determined/estimated as follows : The received signal level in two orthogonal polarisations (eg. θ- and ϕ-polarisations) are measured as the receive probe moves in the environment over random paths, and then averaged. The ratio (usually of the vertical over the horizontal[15] polarisation levels) is the XPR. This is determined experimentally. [KALL 02] reports that the value of XPR has been found to range between 0dB and 9dB, depending on the particular environment (eg. indoor, suburban outdoor, urban, dense urban, medium-density urban, and so on).

■ $\mathscr{P}_\theta(\theta,\phi)$ and $\mathscr{P}_\phi(\theta,\phi)$ are known as the angular power density functions, probability distributions of the angle-of-arrivals (AoA) of the incident waves, or the power angular spectrum (PAS). They are a description of the probability that an incident signal[16] will be incident on the antenna (whose MEG is being determined) from direction (θ,ϕ). They must satisfy the conditions

$$\int_0^{2\pi}\int_0^{\pi}\mathscr{P}_\theta(\theta,\phi)\sin\theta\, d\theta d\phi = 1 \quad (2.2\text{-}50)$$

and

$$\int_0^{2\pi}\int_0^{\pi}\mathscr{P}_\phi(\theta,\phi)\sin\theta\, d\theta d\phi = 1 \quad (2.2\text{-}51)$$

---

[13] Defined in Section 2.2.7.

[14] Unrelated to the antenna whose MEG is being calculated.

[15] This will be the θ-polarised over the ϕ-polarised levels with the coordinate systems defined as we do here, with the z-axis vertical.

[16] That is θ-polarised or ϕ-polarised, respectively.

These functions are either established through measurement campaigns, or are conjectured from arguments based on wireless systems experience. Examples given in [KALL 02] include the Gaussian function and double exponential functions (of which a special case is the so-called Laplacian function [PEDE 97]).

■ The *MEG* clearly depends on the far-zone patterns of the antenna, the orientation of the antenna, its polarization, the AoA distributions of the wireless environment, and the XPR of the environment.

■ In an environment where there is equal probability of a wave to be incoming from any direction[17] with any polarisation, we have $\mathscr{P}_\theta(\theta,\phi)=1/4\pi$, $\mathscr{P}_\phi(\theta,\phi)=1/4\pi$ and $\mathrm{XPR}=1$. The integral in (2.2-49) then evaluates to one-half, and we have $MEG=0.5\left(1-\left|\Gamma_{in}\right|^2\right)\eta_{\mathrm{rad}}$, or in other words *MEG* is equal to half the 'total' radiation efficiency. The maximum value of MEG is $4\pi\eta_{\mathrm{rad}}$ [GLAZ 09].

■ Some [VOLA 07] have defined the mean effective directivity (*MED*) as $MEG=0.5\eta_{\mathrm{rad}}\left(1-\left|\Gamma_{in}\right|^2\right)MED$, because *MED* then only depends on the environment and the radiation pattern.

2.2.10 Performance Metric of Particular Importance for Electrically Small Antennas

We first defined the term "electrically small antenna" in Section 2.2.2. Much theoretical and practical work has been reported on the topic; interest in the subject has increased over the past 15 years because antennas need to be used on physically small mobile communications devices. The works [YAGH 05] and [SIEV 12] provide a particularly concise and to-the-point examination of what is important on the subject[18], and has been used as a guide in this work.

A. Antenna Quality Factor (Q)

The narrow bandwidth of antennas that are electrically small comes as a surprise when one has only had experience with antennas that are electrically much larger, but it is fundamental. As [COLL 19] relates : "It is very disappointing to measure a complete device[19], contained in a smart, expensively-designed case, that has an efficiency[20] of only 15%, but this is not unusual". This narrow bandwidth has resulted in engineers viewing such antennas as resonators (which they are, albeit ones where the portion of the loss, due r

---

[17] Sometimes (perhaps misleadingly, in the light of definitions used in antenna engineering) referred to as an "isotropic" environment.

[18] [SIEV 12] remains a yardstick in spite of having been published 7 years before the writing of this thesis.

[19] Antenna on its host platform.

[20] The total radiation efficiency defined in Section 2.2.6.

radiation, is desirable). And like resonators their bandwidth can be assessed from the value of their quality factor (Q).

B. Bounds on the Q of an Antenna

A useful formula for a lower bound for the Q of an antenna is [SIEV 12], when the polarisation is unconstrained, is

$$Q(\omega) = \frac{1}{ka} + \frac{1}{2(ka)^3} \tag{2.2-52}$$

Here k is the free space wavenumber at frequency ω, and a the radius of the minimum sphere enclosing the antenna. If an antenna is a single-mode[21] one in the sense of characteristic modes, then [ETHI 14] the Q at a self-resonance frequency of the antenna can be found from purely characteristic mode parameters as

$$Q_{\text{cm}}(\omega_o) = \frac{\omega_o}{2}\left|\frac{d\lambda_1}{d\omega}\right|_{\omega=\omega_o} = \frac{f_o}{2}\left|\frac{d\lambda_1}{df}\right|_{f=f_o} \tag{2.2-53}$$

C. Approximate Computation of the Quality Factor of an Actual Antenna

Yaghjian and Best [YAGH 05] derived an approximate expression for antenna quality factor that permits this quantity to be found, at frequency ω_o, for an actual antenna from its input impedance properties as

$$Q_z(\omega_o) \approx \frac{\omega_o\sqrt{\left(R'_{in}(\omega_o)\right)^2 + \left(X'_{in}(\omega_o) + \left|X_{in}(\omega_o)\right| / \omega_o\right)^2}}{2R_{in}(\omega_o)} \tag{2.2-54}$$

The expression is valid for single-resonance antennas in their resonant or anti-resonant regimes, and so are valid for all frequencies. It allows the bandwidth of an antenna to be estimated from the frequency derivative of the input impedance at the desired frequency. We will always denote the quality factor determined in this manner by the symbol Q_z, as has become common practice. The bandwidth for a voltage standing wave ratio no larger than the value VSWR can be estimated as [YAGH 05]

---

[21] This is defined in Section 2.6.3.

$$B \approx \frac{1}{Q}\left(\frac{VSWR-1}{\sqrt{VSWR}}\right) \qquad (2.2\text{-}55)$$

where of course

$$VSWR = \frac{1+|\Gamma_{in}|}{1-|\Gamma_{in}|} \qquad (2.2\text{-}56)$$

2.3 ANTENNA ANALYSIS USING COMPUTATIONAL ELECTROMAGNETICS

2.3.1 Initial Remarks

In the present thesis there is just one CEM method that will be used, namely the method of moments (MM), because it enables us both to find the characteristic modes (CMs) of an object, and can be used to model the driven antenna. The CM concept will be reviewed in Section 2.4. But in order to do that properly we need to set down set down some ideas on integral equation models for conducting antennas, and their solution using the MM. Also mentioned in the thesis is the asymptotic method known as the geometrical theory of diffraction (GTD), and so this will be also be touched on in the present section.

2.3.2 Electric Field Integral Equation Model

The most widely used integral equation in CEM is the electric-field integral equation (EFIE) that models scattering from a perfectly conducting (PEC) object [PETE97], a situation sketched in Fig.2.3-1. We have an arbitrarily shaped perfectly conducting (PEC) scatterer, situated in unbounded space of permittivity ε, permeability μ and zero conductivity ($\sigma = 0$). The surface of the scatterer is denoted S_c. Although we show a single scatterer, there could be more than one, with S_c the union of the surfaces of the individual scatterers. The EFIE can be written as

$$\bar{E}_{\tan}^{scat}\left\{\bar{r}, \bar{J}_s, \mathbb{G}^{fs}\right\} = -\bar{E}_{\tan}^{inc}\left\{\bar{r}, \bar{J}^{imp}, \bar{M}^{imp}, \mathbb{G}^{fs}\right\} \qquad \bar{r} \in S_c \qquad (2.3\text{-}1)$$

■ The subscript “tan” on a quantity implies the component of the quantity tangential to the surface S_c of the PEC object.

- $\bar{J}^{imp}\left(\bar{r}\right)$ and $\bar{M}^{imp}\left(\bar{r}\right)$ are impressed electric and magnetic source current densities exterior to surface S_c. Recall that by impressed is meant that these are unaffected by the electromagnetic fields themselves, and that if all the impressed sources were turned off there would be no fields whatsoever.
- In the absence of the scatterer these sources generate fields $\bar{E}^{inc}\left(\bar{r}\right)$ and $\bar{H}^{inc}\left(\bar{r}\right)$ at all points $\bar{r}$ in free space; these are of course the incident fields. Recall that an incident field is by definition that which exists when the object identified as the scatterer is removed, and that this incident field exists at all points (even within the scatterer).
- Because of the incident field there will be an induced electric surface current density $\bar{J}_s$ on S_c. This will give rise to additional electromagnetic fields, namely the scattered fields $\bar{E}^{scat}\left(\bar{r}\right)$ and $\bar{H}^{scat}\left(\bar{r}\right)$.
- The total field will at all observation points[22] $\bar{r}$ be the sum of the incident and scattered fields, namely $\bar{E}\left(\bar{r}\right)=\bar{E}^{inc}\left(\bar{r}\right)+\bar{E}^{scat}\left(\bar{r}\right)$.
- $\bar{E}^{inc}\left\{\bar{r},\bar{J}^{imp},\bar{M}^{imp},\mathbb{G}^{fs}\right\}$ is the incident electric field, which is a known quantity. It can be found using the known impressed current densities and the free space Greens function (identified by the superscript "*fs*").
- $\bar{E}^{scat}\left\{\bar{r}_s,\bar{J}_s,\mathbb{G}^{fs}\right\}$ is the tangential scattered electric field, and is an integral involving the *unknown* electric surface current density $\bar{J}_s$ on S_c, and a free space Green's function.
- The boundary condition on a PEC object requires

$$\hat{n}\left(\bar{r}\right)\times\bar{E}\left(\bar{r}\right)=\hat{n}\left(\bar{r}\right)\times\left\{\bar{E}^{inc}\left(\bar{r}\right)+\bar{E}^{scat}\left(\bar{r}\right)\right\}=0 \qquad \bar{r}\in S_c \qquad (2.3\text{-}2)$$

and results in the EFIE in (2.3-1)

---

[22] Both inside and outside the PEC scatterer.

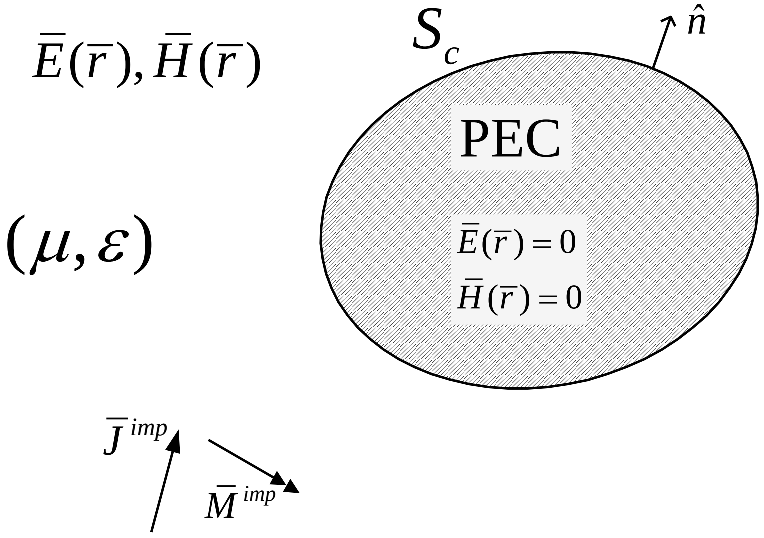

Fig.2.3-1 : Scattering of the fields, from impressed sources, from a perfectly conducting (PEC) object.

2.3.3 Method of Moment (MoM) Solution of an Integral Equation (IE)[23]

The method of moment is a numerical method for solving integral equations. The approach is best appreciated by considering a simple one-dimensional (1D) integral equation and not the 3D one in (2.3-1). The 1D integral equation can be written as

$$\int_{z_L}^{z_U} f(z')\mathbb{G}(z,z')\,dz' = g(z) \qquad z_L \le z \le z_U \tag{2.3-3}$$

The qualifier $z_L \le z \le z_U$ means that the equation (2.3-3) applies only for points in space with z in the interval $z_L \le z \le z_U$. The function $f(z)$ is the *unknown*[24]. The $g(z)$ is a *known* function[25]. The function $\mathbb{G}(z,z')$, is called the *kernel*[26] of the integral equation, is also a *known* function, of two variables z and z'. In such integral equations we need to be able to evaluate $f(z)$ and $g(z)$ at different z values in the same equation. Thus we need to use the primed and unprimed notation, with $z_L \le z' \le z_U$ also. Note that the integration is with respect to z'.

---

[23] Portions of this section have been taken, with permission, from [MCNA 16].

[24] Such as an induced current density.

[25] Related to the incident field.

[26] In the case of CEM-related integral equations this kernel will be some appropriate Green's function.

In order to find an approximate solution for $f(z)$ we first expand $f(z)$ in terms of some selected (and hence *known*) *expansion functions* $f_n(z)$, N_{dof} of them in total[27], as

$$f(z) \approx \sum_{n=1}^{N} a_n \; f_n(z) \tag{2.3-4}$$

Since $f(z)$ is the unknown, the coefficients a_n, $n = 1, 2, ..., N_{\text{dof}}$ are of course unknown at this stage. If we can find them, then (2.3-4) constitutes an approximation to the solution. If we substitute the series expansion (2.3-4) into the original integral equation (2.3-3) we get

$$\int_{z_L}^{z_U} \left(\sum_{n=1}^{N_{\text{dof}}} a_n \; f_n(z') \right) \mathbb{G}(z,z')\, dz' \approx g(z) \tag{2.3-5}$$

The linearity of the integral operation next allows us to move the summation from under the integral sign, giving

$$\sum_{n=1}^{N} a_n \underbrace{\left(\int_{z_L}^{z_U} f_n(z') \mathbb{G}(z,z')\, dz' \right)}_{\Psi_n(z)} = g(z) \tag{2.3-6}$$

Since the $f_n(z')$ are known expansion functions, the z-dependent function $\Psi_n(z)$ can be evaluated[28] for any value of z.

We next select a second set of N_{dof} functions[29] $\{g_1(z), g_2(z), ..., g_m(z), ..., g_{N_{\text{dof}}}(z)\}$. We need to select them and thus they are *known*. These are conventionally called the *weighting* or *testing* functions. We can then multiply both sides of (2.3-6) by *each* of these weighting functions *in turn*, each time integrating the products on the left and right hand sides with respect to z (as opposed to with respect to z') over the interval $z_L \le z \le z_U$. This process yields

---

[27] The subscript in the symbol N_{dof} denotes “degrees of freedom”.

[28] If not in closed form, then at least numerically.

[29] It is called a Galerkin Method of Moment approach if $g_n(z) = f_n(z)$ for all $n = 1, 2, ..., N_{\text{dof}}$.

$$\sum_{n=1}^{N_{\text{dof}}} a_n \left(\int_{z_L}^{z_U} \Psi_n(z)\, g_m(z)\, dz \right) = \int_{z_L}^{z_U} g(z)\, g_m(z)\, dz \tag{2.3-7}$$

$$m = 1, 2, ..., N_{\text{dof}}$$

where $m = 1, 2, ..., N_{\text{dof}}$ indicates that (2.3-7) holds for each *m* in turn. We can tidy (2.3-7) up to read

$$Z_{mn} = \int_{z_L}^{z_U} \Psi_n(z)\, g_m(z)\, dz \tag{2.3-8}$$

and

$$b_m = \int_{z_L}^{z_U} g(z)\, g_m(z)\, dz \tag{2.3-9}$$

so that the set of linear equations represented by (2.3-7) can be written in matrix notation as

$$[Z]\,[I] = \left[V^{inc}\right] \tag{2.3-10}$$

where the *known* method of moment matrix is

$$[Z] = \begin{bmatrix} Z_{11} & Z_{12} & \cdot & \cdot & Z_{1N} \\ Z_{21} & Z_{22} & \cdot & \cdot & Z_{2N} \\ \cdot & \cdot & \cdot & \cdot & \cdot \\ \cdot & \cdot & \cdot & \cdot & \cdot \\ Z_{N1} & Z_{N2} & \cdot & \cdot & Z_{NN} \end{bmatrix} \tag{2.3-11}$$

The *known* column matrix (also referred to as the excitation matrix)

$$\left[V^{inc}\right] = \begin{bmatrix} b_1 \\ b_2 \\ \cdot \\ \cdot \\ b_N \end{bmatrix} \tag{2.3-12}$$

while the column matrix

$$[I] = \begin{bmatrix} a_1 \\ a_2 \\ \cdot \\ \cdot \\ a_N \end{bmatrix} \tag{2.3-13}$$

is the matrix of *unknown* coefficients. Solution of the matrix equation (2.3-10) then yields $[I]$, and the approximate solution is known through (2.3-4).

2.3.4 The Surface Patch Method of Moment Formulation (MoM) Solution of an Integral Equation (IE)

Consider the PEC object shown in Fig.2.3-2. It has been meshed into triangular elements. A set of expansion functions $\bar{J}_n(\bar{r})$, $n = 1, 2, ..., N_{\text{dof}}$ can be defined over this surface, with each $\bar{J}_n(\bar{r})$ associated with the n-th common edge between all pairs of triangles, as indicated in Fig.2.3-3. The expansion functions were developed by Rao, Wilton and Glisson [RAO 82], and have thus become known as RWG expansion functions. They are cleverly defined in sense that continuity of the current density component normal to any edge is guaranteed, as is physically required. This is true even if the two triangles to which the common edge belongs do not lie in the same plane. Note that the number of expansion functions N_{dof} is not equal to the number of triangles N_{Δ} . Any triangle that is connected to three other triangles will have three expansion functions defined on it, one for each of its three edges that are connector to the other triangles. An isolated single triangle has no expansion function defined on it (because it has no edge in common with another triangle) on it, and hence as far as the CEM analysis is concerned does not exist[30]. Details of the formulation can be found in [RAO 82] and [JOHN 90]. Higher-order versions of the RWG expansion functions have also been developed [GRAG 97]. These RWG expansion functions can be used [PETE 97] in a MM formulation to discretize the EFIE in (2.3-1) to a matrix equation[31] of the form (2.3-10) that can be solved for coefficients a_n , $n = 1, 2, ..., N_{\text{dof}}$ (in other words, column vector $[I]$) and hence the current density

$$\bar{J}_s(\bar{r}) = \sum_{n=1}^{N_{\text{dof}}} a_n \, \bar{J}_n(\bar{r}) \qquad (2.3\text{-}14)$$

This current density can be used to find all the associated electromagnetic fields. In the case of the EFIE the expression (2.3-8) for the terms in the MM impedance matrix $[Z]$ becomes

$$Z_{mn} = C_o \iint_{S_m} \bar{J}_m(\bar{r}) \cdot \bar{E}_n \left\{ \bar{r}, \bar{J}_n, \mathbb{G}^{fs} \right\} dS \qquad (2.3\text{-}15)$$

---

[30] More will be said about this in Section 3.10.

[31] Column vector $[I]$ is also often written as $[J]$.

Quantity $\bar{E}_n\left\{\bar{r}, \bar{J}_n, \mathbb{G}^{fs}\right\}$ is[32] the field due to expansion function $\bar{J}_n(\bar{r})$, obtained using the free-space Green's function $\mathbb{G}^{fs}$; the integration is over the region S_m occupied by the m-th expansion function; C_o is a known constant. In essence, Z_{mn} can be interpreted is the mutual impedance between the m-th and n-th expansion functions. The impedance matrix $[Z]$ will be of size $N_{\text{dof}} \times N_{\text{dof}}$. The number of degrees of freedom N_{dof} must be large enough so that (2.3-14) is an accurate representation of the true $\bar{J}_s(\bar{r})$. This means that there must be a sufficient number of triangles in the mesh[33]. Another way of stating this is that dimensions of the sides of the triangles must be small enough in terms of wavelength. Most commercial codes based on the MM use RWG expansion functions.

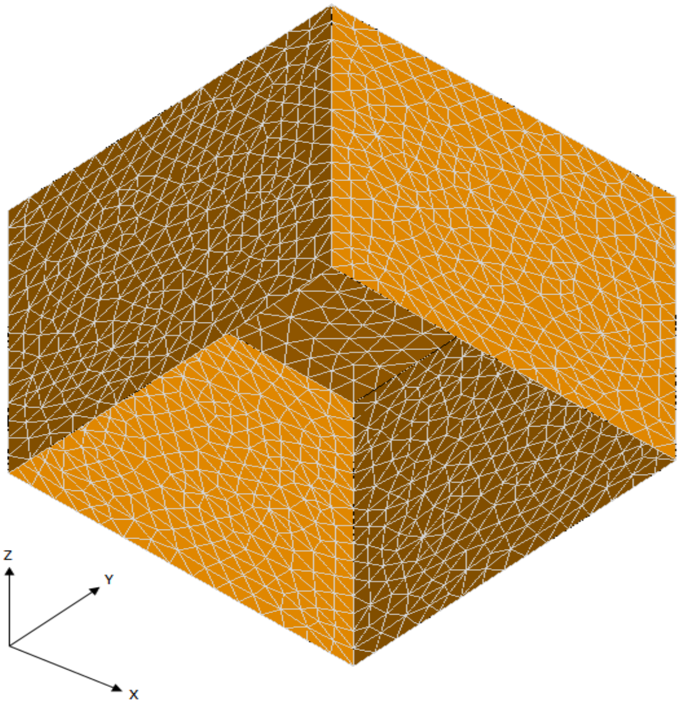

Fig.2.3-2 : PEC object (cubic bottomless rectangular box) meshed into triangular elements.

---

[32] Its 1D equivalent is $\Psi_n(z)$ in expression (2.3-6).

[33] The mesh must be fine (or dense) enough.

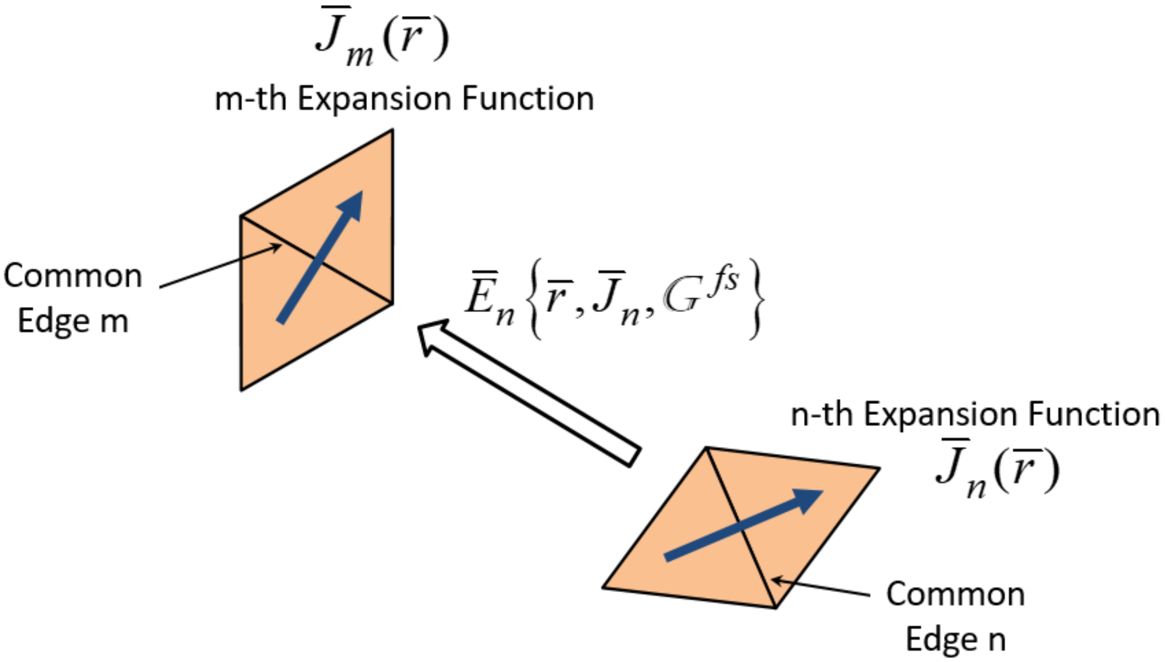

Fig.2.3-3 : Four of the triangles from the mesh in Fig.2.3-2, shown exaggerated in relative size.

2.3.5 Hybrid Moment-Method / Geometrical-Theory-of-Diffraction (MM-GTD) Methods

If a scattering object is electrically very large, then the field scattered from it can be found in terms of rays[34] that reflect or diffract from key features of the object's geometry. The details are beyond the scope of this review chapter, but can be found in [MCNA 91] and [PAKN 16], and are known as the geometrical theory of diffraction (GTD). Often the overall electrical size of the PEC object, such as the situation shown in Fig.2.3-4, is such that N_{dof} would need to be too large for feasible computation. In such cases a hybrid approach can be used, as will next be briefly outlined. The original PEC object is meshed as usual with N_{dof} expansion functions, but the very large additional object is not. The impedance matrix is still of size $N_{\text{dof}} \times N_{\text{dof}}$. However, the presence of the very large object will alter the values of the matrix terms Z_{mn} from what they would be if the very large object were not present. This perturbation of each matrix element is found using the GTD. The term $\bar{E}_n\left\{\bar{r},\bar{J}_n,G^{fs}\right\}$ in (2.3-5) is altered by adding the term $\bar{E}_{GTD}\left\{\bar{r},\bar{J}_n\right\}$ to it, as we try to illustrate in Fig.2.3-5. The pioneering work is described in [EKEL 80], with a subsequent review

---

[34] Ray-based methods are only accurate when the scattering objects are large in terms of wavelength.

provided in [MEDG 91]. More recent improvements have been described in [THER 00], [JAKO 10] and [JAKO 97].

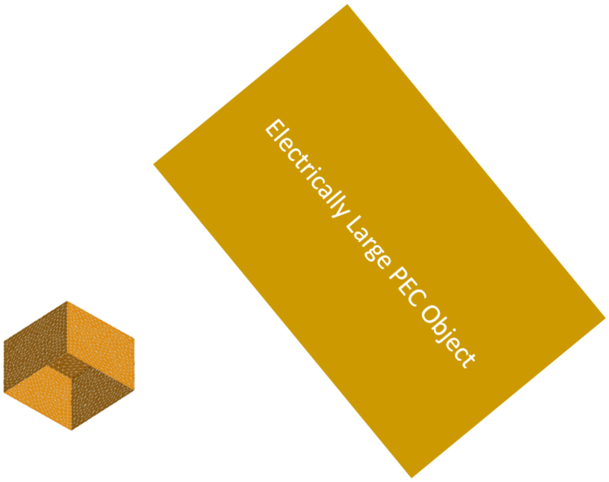

Fig.2.3-4 : "Original" PEC object from Fig.2.3-2, but now in the presence of an electrically very large additional PEC object.

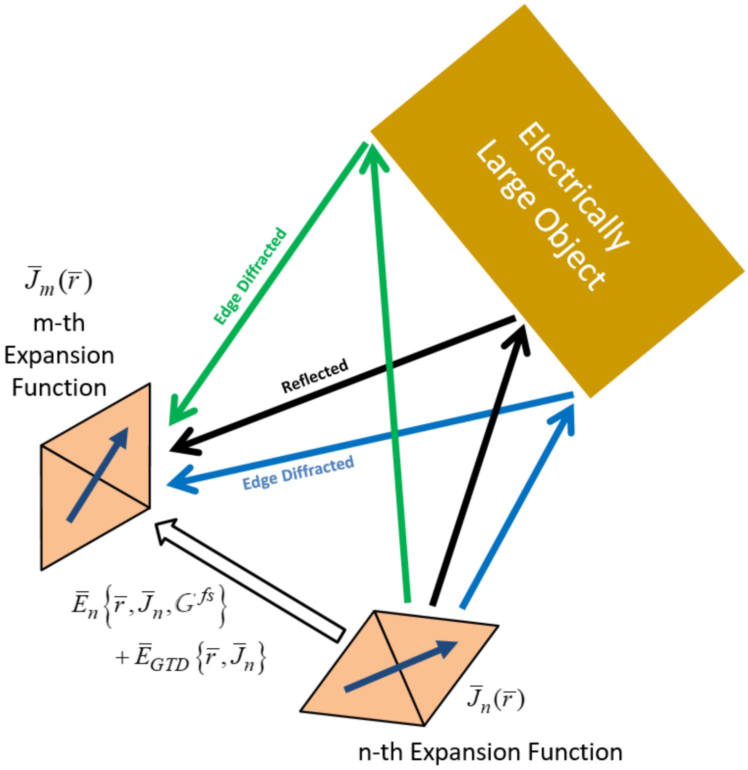

Fig.2.3-5 : Perturbation of the values of the MM matrix accounted for using the GTD.

2.4 CHARACTERISTIC MODES

2.4.1 Introductory Remarks

The theory of characteristic modes was first introduced by Garbacz [GARB 65], but their determination for conducting objects was reformulated by Harrington and Mautz [HARR 71a] in terms of integral equations. It was the last-mentioned work that made it possible to compute the characteristic modes (CMs) of an arbitrary conducting object through the numerical solution of an integral equation using the method of moments [HARR 71b]. A few years after its introduction, a means of computing the CMs of penetrable objects [HARR72] [CHAN77] was published. This work is now also described in a recent textbook [CHEN 15b]. In this thesis we are concerned with antennas composed of conducting material only, and thus the CM formulations reviewed below are for this case only.

2.4.2 Conventional[35] Characteristic Modes of Conducting Objects

As stated in Section 2.3, the EFIE modelling of a conducting object[36] is most often a driven problem, with an impressed source (responsible for the incident field) specified. This allows us to solve for the resulting induced current density on the PEC object using (2.3-1). Characteristic mode analysis on the other hand involves an eigenvalue problem, independent of any excitation, and provides information dependent on the scattering object itself. This eigenvalue problem is [HARR 71b]

$$[X][J_n] = \lambda_n [R][J_n] \tag{2.4-1}$$

where λ_n and $[J_n]$ are the CM eigenvalues and eigenvectors (eigencurrents), respectively. The matrices $[R]$ and $[X]$ are defined via $[Z]=[R]+j[X]$. The $[Z]$ is the MM matrix from Section 2.3.4. Note that $[J_n]$ is a column vector of length N_{dof}; the subscript "*n*" identifies the mode and not an element in the column vector. Both $[R]$ and $[X]$ must be symmetric [HARR 71a] in order to obtain real eigenvalues and eigenvectors for a lossless (eg. PEC) case, and so a Galerkin MM approach[37] must be used. The eigenvalues can be shown to be the ratio of the reactive power to the radiated power in the modes. So, an eigenvalue is equal to zero when the associated mode is at resonance, and equal to infinity (or large number) when the

---

[35] As opposed to the sub-structure characteristic modes to be described in Section 2.4.3, and of late also being referred to as full-structure characteristic modes [XIAN 19].

[36] Which will henceforth, at least as far as CM analyses are concerned, be assumed to be a perfectly conducting (PEC) object.

[37] Defined in Section 2.3.3.

mode is non-radiating (reactive). The eigenvalues can be negative or positive indicating a capacitive or inductive mode. The CM eigencurrents are orthogonal in the following sense [HARR 71b]:

$$[J_m]^T[R][J_n]=[J_m^*]^T[R][J_n]=\delta_{mn} \tag{2.4.2}$$

$$[J_m]^T[X][J_n]=[J_m^*]^T[X][J_n]=\lambda_n\delta_{mn} \tag{2.4-3}$$

and

$$[J_m]^T[Z][J_n]=[J_m^*]^T[Z][J_n]=\left(1+j\lambda_n\right)\delta_{mn} \tag{2.4-4}$$

where δ_{mn} is the Kronecker delta,

$$\delta_{mn}=\begin{cases}0 & m\neq n\\ 1 & m=n\end{cases} \tag{2.4-5}$$

Note that the currents are normalized so that individual modes radiate a power of 1 Watt. The CM fields in the far zone (i.e. over the sphere at infinity) are orthogonal in the following sense [HARR 71a]:

$$C_{mn}=\frac{1}{\eta_0}\oiint_{S_\infty}\bar{E}_m(\theta,\phi)\cdot\bar{E}_n^*(\theta,\phi)\sin\theta\, d\theta d\phi=\delta_{mn} \tag{2.4-6}$$

and

$$\frac{1}{\eta_0}\oiint_{S_\infty}\bar{H}_m(\theta,\phi)\cdot\bar{H}_n^*(\theta,\phi)\sin\theta\, d\theta d\phi=\delta_{mn} \tag{2.4-7}$$

where $\eta_0=\sqrt{\mu_o/\varepsilon_o}$ is the free-space intrinsic impedance, and $\bar{E}_m(\theta,\phi)$ and $\bar{H}_m(\theta,\phi)$ are the far-zone eigenfields (with the distance dependent term e^{-jkr}/r suppressed) due to eigencurrent $\bar{J}_m$. The expressions in (2.4-2) through (2.4-4), (2.4-6), and (2.4-7), are referred as the current and field orthogonality relationships. The modal weighting coefficient α_n of the n-th mode, is found as [HARR 71a]

$$\alpha_n=\frac{\left\langle \bar{J}_n,\bar{E}^i_{\tan}\right\rangle}{1+j\lambda_n}=\frac{V_n^i}{1+j\lambda_n} \tag{2.4-8}$$

In (2.4-8) the terms V_n^i are seen to be as the inner product of the CM eigencurrent with the incident field due to the impressed source in the absence of the PEC object. It allows one to determine "how much" of each of the characteristic modes is excited for a given excitation.

Due to the orthogonality properties, any arbitrary surface current $\bar{J}_s$ and its fields ($\bar{E}$, $\bar{H}$) can be expressed as a linear sum of the CM eigencurrents $\bar{J}_n$ and eigenfields ($\bar{E}_n$, $\bar{H}_n$) of the object, namely

$$\bar{J}_s(\bar{r}) = \sum_{n=0}^{\infty} \alpha_n \bar{J}_n(\bar{r}) \tag{2.4-9}$$

$$\bar{E}(\bar{r}) = \sum_{n=1}^{\infty} \alpha_n \bar{E}_n(\bar{r}) \tag{2.4-10}$$

and

$$\bar{H}(\bar{r}) = \sum_{n=1}^{\infty} \alpha_n \bar{H}_n(\bar{r}) \tag{2.4-11}$$

The quantity

$$MS = \left| \frac{1}{1 + j\lambda_n} \right| \tag{2.4-12}$$

is called the modal significance factor, the term contained within the modulus signs also occurring in expression (2.4-8). This quantity will lie between zero and unity; if a CM is resonant (has zero eigenvalue) then $MS = 1$.

2.4.3 Sub-Structure Characteristic Modes

The sub-structure CM idea for conducting objects was introduced in [ETHI 12] and in more general form in [ALRO 14] and [ALRO 16]. It is next described in the form given in the latter reference.

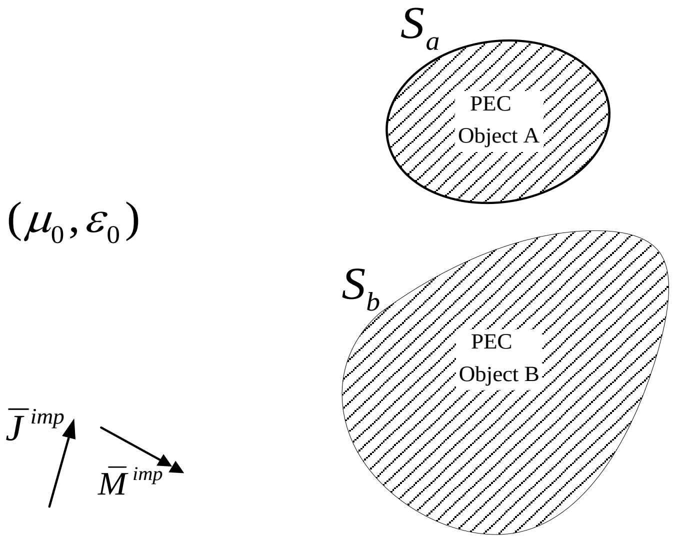

Fig.2.4-1 **:** Two objects considered for the sub-structure CM analysis.

Consider the PEC scatterer shown in Fig.2.4-1. We recognize that it is possible to purposefully view the structure in Fig.2.4-1 as consisting of two portions, Objects#A and #B, with distinct expansion function subsets located on these two portions. We can then partition the method of moment matrix equation to read

$$\begin{bmatrix} [Z_{AA}] & [Z_{AB}] \\ [Z_{BA}] & [Z_{BB}] \end{bmatrix} \begin{bmatrix} [J_A] \\ [J_B] \end{bmatrix} = \begin{bmatrix} [V_A] \\ [V_B] \end{bmatrix} \qquad (2.4\text{-}13)$$

This does not alter the scattering problem in any way. We will call (2.4-13) the *primary* MM formulation equation. It is possible to find the conventional CMs of the complete structure as the solutions of the matrix eigenvalue problem (2.4-1).

We can next define the general sub-structure CM concept. In order to do this we manipulate matrix equation (2.4-13) into the two equations

$$\left\{[Z_{\mathrm{AA}}]-[Z_{\mathrm{AB}}][Z_{\mathrm{BB}}]^{-1}[Z_{\mathrm{BA}}]\right\}[J_A]=[V_{\mathrm{A}}]-[Z_{\mathrm{AB}}]\left[Z_{\mathrm{BB}}\right]^{-1}\left[V_{\mathrm{B}}\right] \qquad (2.4\text{-}14)$$

and

$$\left[J_B\right]=-\left[Z_{\mathrm{BB}}\right]^{-1}\left[Z_{\mathrm{BA}}\right]\left[J_A\right]+\left[Z_{\mathrm{BB}}\right]^{-1}\left[V_{\mathrm{B}}\right] \qquad (2.4\text{-}15)$$

In (2.4-14), we can write

$$[Z_{\mathrm{AA}}]-[Z_{\mathrm{AB}}][Z_{\mathrm{BB}}]^{-1}[Z_{\mathrm{BA}}]=[Z_{\mathrm{sub}}] \qquad (2.4\text{-}16)$$

and obtain the *sub-structure* CMs of Object#A in the presence of Object#B from eigenvalue problem

$$[X_{sub}][J_n^{Asub}] = \lambda_n^{sub}[R_{sub}][J_n^{Asub}] \tag{2.4-17}$$

with sub-structure eigenvalues λ_n^{sub} different from those λ_n of the conventional CMs, and $[Z_{sub}] = [R_{sub}] + j[X_{sub}]$. Note that the set of λ_n^{sub} are not a subset of the set of λ_n.

The $[J_n^{Asub}]$ are the sub-structure eigencurrents on Object#A in the presence of Object#B. In order to find the eigenfields due to sub-structure eigencurrents $[J_n^{Asub}]$ we must first find the "secondary" currents $[J_n^{B\sec}]$ on Object#B. This is a separate driven problem. We must view $[J_n^{Asub}]$ as an impressed current density (with Object#A absent) that illuminates Object#B, and use a MM formulation (which we will call the *secondary* method of moment formulation) to find $[J_n^{B\sec}]$. The elements of $[Z_{BA}]$ in the primary formulation are of the form $Z_{ij} = \iint_{S_B} \bar{E}\left\{\bar{r}, \bar{J}_j(\bar{r})\right\} \cdot \bar{J}_i(\bar{r})\,\mathrm{dS}$. Here $\bar{E}\left\{\bar{r}, \bar{J}_j(\bar{r})\right\}$ would be the electric field at $\bar{r}$ due to the j-th expansion function $\bar{J}_j(\bar{r})$, which is on Object#A, whereas $\bar{J}_i(\bar{r})$ is the i-th weighting function, which is on Object#B. Now the matrix equation for the secondary problem would be of the form

$$\left[Z_{\mathrm{BB}}\right][J_n^{B\sec}] = [\mathrm{V}_B^{\sec}] \tag{2.4-18}$$

We write $[\mathrm{V}_B^{\sec}]$ because it is the excitation with $\bar{J}_n^{Asub}$ as the impressed current, and is not the same as in primary formulation (2.4-13). If we use the same expansion functions on Object#B for both the primary and secondary problems then $\left[Z_{\mathrm{BB}}\right]$ is the same in the two problems. The elements of $[\mathrm{V}_B^{\sec}]$ in the secondary formulation will be of the form $-\iint_{S_B} \bar{E}^{inc}\left\{\bar{r}, \bar{J}_n^{Asub}(\bar{r})\right\} \cdot \bar{J}_i(\bar{r})\,\mathrm{dS}$, where $\bar{E}^{inc}\left\{\bar{r}, \bar{J}_n^{Asub}(\bar{r})\right\}$ would be the electric field at $\bar{r}$ due to $\bar{J}_n^{Asub}$ viewed as an impressed current density. Of course, we have $\bar{J}_n^{Asub}(\bar{r})$ described in the form of expansion functions and a set of coefficients. Thus the expression for $[\mathrm{V}_B^{\sec}]$ in fact reduces to

$$[\mathrm{V}_B^{\mathrm{sec}}] = -\left[Z_{\mathrm{BA}} \right][J_n^{\mathrm{Asub}}] \tag{2.4-19}$$

If we substitute this into (2.4-18) the latter becomes

$$\left[Z_{\mathrm{BB}} \right][J_n^{B\mathrm{ec}}] = -\left[Z_{\mathrm{BA}} \right][J_n^{\mathrm{Asub}}] \tag{2.4-20}$$

which can be rewritten as

$$[J_n^{\mathrm{Bsec}}] = -\left[Z_{\mathrm{BB}} \right]^{-1}\left[Z_{\mathrm{BA}} \right][J_n^{\mathrm{Asub}}] \tag{2.4-21}$$

Thus it turns out that we already have all the matrix information needed for the secondary method of moment formulation from the primary formulation. Expression (2.4-15) just happens to be the same as (2.4-21) with $\left[V_{\mathrm{B}} \right] = [0]$, but has nothing to do with $\left[V_{\mathrm{B}} \right]$ or $\left[V_A \right]$ of the primary problem. The sub-structure CMs do not depend on $\left[V_{\mathrm{B}} \right]$ or $\left[V_A \right]$ in any way, as expected because of the fact that CM formulations are eigenvalue and not driven problems. The sub-structure CM field $\bar{E}_n$ is the superposition of the fields due to $\bar{J}_n^{Asub}$ and $\bar{J}_n^{B\sec}$. It is shown in [ALRO 16] that the sub-structure CMs also satisfy orthogonality conditions on the current densities and fields; the reader is referred to that reference for a catalogue of these properties.

Suppose we knew the modified Green's function which can be used to determine the field in all of space for an arbitrary electric current density distribution in the presence of Object#B, and used it to derive an EFIE for the current density on Object#A. In the associated method of moment formulation the expressions for the impedance matrix and excitation vector now involve the appropriate modified Green's function and so are not the same as when the free-space Green's function is used. It would provide the same sub-structure CMs as those described in the paragraphs above. However, such modified Green's functions are usually not known, except in idealised cases such as when Object#B is an infinite PEC groundplane, of infinitely long PEC circular cylinder, and so on. The route described in the paragraphs above effectively uses the modified Green's function without explicitly needing it.

2.4.4 Applications of Characteristic Modes in Antenna Design

Computational electromagnetics provides superb tools for antenna analysis. The source densities and electromagnetic fields from such modelling incorporate all the physics associated with a particular configuration. Several authors have shown how the use of a CM analysis of a structure allows one to exploit this information to the full, and have used it in systematized antenna design.

Characteristic modes can be used in two ways in antenna design. Most authors use them to “understand” the antenna design problem being tackled and then use the insight gained to come up with a good design; this might be called the *indirect approach*. Another way is more direct, namely the use of CMs in the automated shaping of the antenna. In this thesis we are interested in the latter shape synthesis, and will extend the range application of the *direct approach*, and will review the topic of shape synthesis (even those that do not use CMs) in much more detail in Section 2.6. Suffice it to say here that a representative cross-section of the *indirect use* of CMs in antenna design includes :

- Tuning and bandwidth enhancement of electrically small antennas [ADAM 11]
- The excitation of chassis modes as antennas for small terminals [MART 11][WU 13].
- MIMO antennas [ETHI 08][DENG 16][MART 16][LI 14][MIER 13].
- Reconfigurable MIMO antennas that utilise chassis modes [KISH 13].
- Coplanar-fed dielectric resonator antennas [BERN 15].
- Shipboard antennas [CHEN 15a].
- Slotted patch antennas [CHEN 12].
- UWB antennas [ANTO 10].
- Wearable antenna design [YAN 18]
- UHF RFID antennas on tin cans [SHAR 19]

The above applications, and many more, have steadily increased interest in characteristic modes, and hence their accurate computation [CAPE 17][DAI 16].

2.5 A PRIMER ON OPTIMISATION ALGORITHMS

2.5.1 Classification of Optimisation Algorithms

An optimisation algorithm is one that tries to find the minimum (or maximum) of some function F_{obj}, called the objective function, fitness function or cost function, with respect to several independent variables. These algorithms are, in the numerical mathematics literature, described as performing optimisation without constraints (unconstrained optimisation) or with constraints (constrained optimisation). In antenna work the constraints often do not fit into a neat mathematical framework, and so unconstrained optimisation algorithms are used with the constraints built into the objective functions themselves. This is especially so for evolutionary algorithms.

2.5.2 Gradient Based Algorithms

Gradient based optimization algorithms are essentially greatly advanced versions of the technique we learn in beginning calculus courses for finding the location of the minimum (or maximum) value of a given mathematical function. In such courses we start with a real function $f(x)$ of the single independent variable x and wish to know at what x value (i.e. at what point) the function is a minimum. We recall that this involves use of the derivative (and possibly second derivative) of the function with respect to x. When the function to be maximized is dependent on several independent variables the more general gradient operations are involved instead of a simple derivative. The now-multidimensional point is sought at which the function (still a single real number) is a minimum. The various algorithms devised to do this differ in the way we navigate in the multidimensional landscape to reach the desired point where the function is maximized. Good tutorial accounts of these "gradient based" algorithms remain [BAND 69] and [BAND 88]. The objective functions used must of course be such that their gradients are defined and can be found.

2.5.3 Evolutionary Algorithms

Optimization algorithms are available that do not use gradients [RAHM 12]. This has made them very flexible indeed. They go by interesting names (that attempt to hint at how they work) such as particle swarm optimization, differential evolution [OLIV 12][ROCC 11], and genetic algorithms [JOHN 97][MITC 99]. Only the genetic algorithm (GA) will be used in this thesis, and so it will be reviewed immediately below. Some other evolutionary algorithm could be used in place of the GA in the shape synthesis tool, but this will not be done. Optimization algorithms are available already implemented in commercial software, and their development is not considered a contribution in this thesis[38].

2.5.4 Further Detail on a Specific Evolutionary Algorithm : The Genetic Algorithm

A. Aim of Sub-Section

In the shape synthesis tool that is the subject of Chapter 3 we will use the genetic algorithm (GA) exclusively, and so it will be discussed in some detail. However, this will be done in the context in which it is used in this thesis, namely in relation to the shaping of conducting surface antennas.

B. Pixelation of a Conducting Surface

Consider a fictitious planar surface that has been divided into a mesh of N_{bit} elements[39], as shown in Fig.2.5-1. Each element can be filled with conductor or left unfilled[40]. We can associate a 1 or a 0 with each element, a 1 if it is filled with conductor and a 0 if it is not. We can define a chromosome that consists of a string of N_{bit} genes (or bits), for example $\{110011000110011............0100\}$, and map each chromosome bit to a different element in the meshed geometry. Thus by altering the binary values of each bit a different conducting geometry can be defined. Another way of thinking of it is that each shape is described by a bar-code. An objective (or fitness) function F_{obj} is defined that is a function of the binary value of each gene constituting the chromosome. In other words, it can be considered a function whose indpendent variables are the bits in the chromosome. Thus it is a function of the shape of the conductor. The definition of F_{obj} is naturally problem-specific. The operation of the GA will next be explained in outline, emphasizing those aspects that will need to be referred to when discussing the development of the new antenna shape synthesis tool in Chapter 3.

---

[38] They are merely used as a building block in the actual contribution, namely the extension of shaping procedures to include 3D conducting surfaces (Chapter 4) and closely-spaced antennas (Chapter 5)

[39] In the case shown these are rectangular. This will not be so in the shape synthesis tool developed in Chapter 3; reasons will be given there.

[40] Each cell is actually filled completely with conductor or has no conductor at all. The gaps shown in the diagram are for clarity of explanation only.

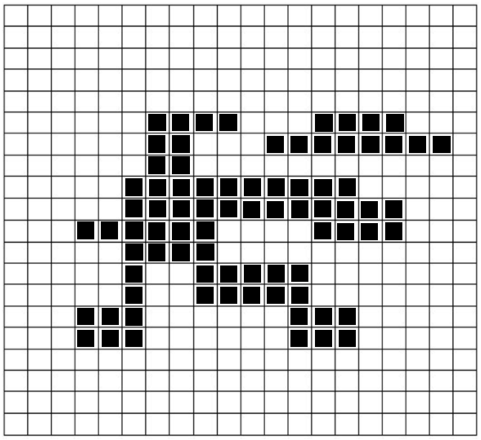

Fig.2.5-1 : A demonstration of pixelization of a geometry. Those pixels (or elements) occupied by conductor are sketched in black; unfilled elements are left clear.

C. Outline of the Genetic Algorithm

■ *Initialisation*

All optimization algorithms have to have a starting point. In the GA this is a set of possible, but far from final, solutions (called the initial population of chromosomes) that are generated randomly. The number of *members* in the *population* is called the *population size* N_{pop}. The value of N_{pop} has to be chosen. The larger the value of N_{pop} the better the chances of the optimization scheme actually allowing F_{obj} to reach its physically possible maximum value. This can be viewed as allowing enough genetic diversity to exist in the population. There is always a trade-off though. For instance, in antenna work the evaluation of F_{obj} for each population member usually needs a full-wave electromagnetic analysis. This is computationally time-consuming in the present context, since such an analysis will be needed for each member of each new population as the GA iterates (that is, for each new *generation*).

■ *Selection*

Once a population is created, members of the population must be evaluated according to the fitness function. As stated above, it takes the conductor geometry of each member, and outputs a numerical value for the associated F_{obj} that allows each member to be ranked relative to the other members. Once the fitness of all members has been computed, a portion (call it $N_{\text{select}} < N_{\text{pop}}$ for convenience) of the "top-scoring" members is selected. Many sophisticated methods of *selection*[41] have been developed (eg. fitness

---

[41] There are seven possibilities in the particular GA whose choice we discuss in Section 3.3.

proportionate selection; tournament selection) for deciding which population members will be mated. These "elite" population members are then mated, and generate offspring that share characteristics with their parents, and that are subsequently integrated into the population. One can keep the population size N_{pop} constant (in which case the lowest fitness members not selected for mating are removed), or a more complicated variable population size can be used in which some of the lowest fitness members are retained but simply not allowed to mate. The hope is that a gradual improvement in the fitness of the members of the population will occur as the GA iterates from generation to generation – in other words that we will find the chromosome that gives F_{obj} its minimum (or maximum) value.

■ ***Mating Operators***

These could be called mating operators, and include the operations of crossover, mutation and migration. As previously stated, the population members that are selected for mating (crossover) produce offspring that contain a mixture of the parents' qualities. *Crossover*[42] is the process that combines two individuals (parents) in the population to form a new individual (child) for the next generation. Treatises have been written on how crossover may be accomplished, the particular GA whose choice we discuss in Section 3.3 allows eight possibilities. In order to prevent the optimization algorithm from quickly becoming trapped in local extrema, new genetic material must be introduced into the generation. This is done using mutation and migration. *Mutation*[43] changes a small portion of the offspring[44] so that they no longer perfectly reflect subsets of the parents' genes. The chance of a particular offspring undergoing a mutation, as well as the severity of the mutation, is governed by a probability distribution. Genetic diversity can also be increased using a *migration* operator (that makes small random changes), whose name at once allows us to grasp its function. Migration can be forward, backward, or both.

■ ***Termination***

The algorithm must eventually be halted. There are two cases in which this usually occurs: either the algorithm has reached some specified *maximum number of generations* (say N_{gen}), or the value of F_{obj} is ound to not improve significantly from one generation to the next (eg. F_{obj} changes in value by an amount less than Tol .

---

[42] In essence the "crossover" point in the chromosome that decides which bits will be altered to produce a new chromosome.

[43] It too has been studied extensively by numerical analysts. In the particular GA whose choice we discuss in Section 3.3 there are seven different ways of achieving mutation that one can decide on.

[44] By flipping some of the bits in the chromosome.

2.6 EXISTING ANTENNA SHAPE SYNTHESIS TECHNIQUES

2.6.1 Introduction

The classification of the way optimisation is used in antenna design has already been mentioned in Section 1.1. In this thesis we are solely interested in the shape optimisation (or shape synthesis) of antennas that are electrically small or possibly of intermediate size[45]. Reasons for the practical interest in the latter type of antenna will be presented in the introductory sections of Chapters 4 and 5.

2.6.2 Existing Shape Synthesis Methods Using *Driven Problem Simulation*

In order to use optimization algorithms for the shape synthesis of any antenna it is necessary to translate the design goals into a quantity that, when minimized, provides an antenna that has the performance we desire. The most obvious way to define an objective function in antenna work would be to use some well-chosen combination of the input reflection coefficient, the directivity, radiation efficiency, and so on, as defined in Section 2.2. However, such quantities can only be found (during the shaping process) if the complete antenna is modelled, as a driven problem. This implies that the type and location of the feed has to be selected before the shaping process. Most previous work on shape synthesis has adopted this route. Such shape optimization of low gain microstrip [JOHN 99a][JOHN 99b][THOR 05], and wire antennas [YAMA 09], with only the conductor geometry undergoing shaping through the removal or retention of conducting pixels/segments into which the starting shape is divided, has allowed miniaturization and bandwidth increases; the structure planarity is preserved, and so this can be described as two-dimensional shaping. Fully three-dimensional shaping of thin-wire antennas is performed in [ALTS 02][LIND 99][CHOO 05], with some restrictions placed on the allowed occupied volume to maintain a sense of practicality. The above all used the GA as the optimisation method. More recently [MIRH 16] other evolutionary algorithms have been tried in place of the GA in the pixelisation-based shaping; it works but is not more effective than when the GA is used. Binary differential evolution has also been used as a replacement for the GA, but has only been applied [GOUD 17] to relatively simple antenna shaping problems already satisfactorily tackled with the GA in place.

One alternative to the pixelisation approach used so-called topology optimization (gradient based), based on methods used in structural engineering, and is discussed in [HASS 14] and [EREN 11]. It allows

---

[45] The shaping of electrically large antennas with high-directivity antennas are not of interest here. This includes the shaping of large reflector surfaces that form a component of a completely different class of antenna, requiring a separate feed antenna to illuminate the reflector, which together with it form the actual antenna.

extremely fine resolution, as is apparently required in its structural application, but it is not clear whether such resolution is really significant in antenna problems. Another non-pixelisation route uses gradient based optimisation to shape antennas whose geometry is defined in terms of splines [GRIF 06][TOIV 10][SALU 18]; the spline parameters are adjusted during the optimisation process. With the exception of [EREN 11], all the shape synthesis work for conducting surface antennas (as opposed to thin wires) that we have surveyed, such as that reviewed above, *has been applied to planar shapes only*.

2.6.3 Existing Shape Synthesis Methods Using *Characteristic Mode Approaches*

A method for the shape synthesis of single electrically-small antennas, unique in the sense that the feed location need only be selected after the shaping has been performed, was described in [ETHI 14]. A related route was used in [YANG 19] for MIMO antennas, and has been termed a *shape-first, feed-next* approach. This work applies to electrically small or intermediate-size antennas that are “single-mode” in the sense that only one dominant CM is sufficient to describe the behaviour of the antenna. If the antenna proper radiates in the presence of other objects (that need not be electrically small) the approach of [ETHI 14] can still be used, except that the sub-structure CMs of the antenna proper (with the other objects in place) must be used. The antenna proper is then of an electrical size that makes it “single mode” in the sense of its sub-structure CMs [ETHI 12][ALRO 16]. The reason the antenna must be single-mode in a CM sense is that the method uses CMs to construct the objective functions whose minimization will constitute the shaping process; this is the key reason it is not necessary to select the feedpoint location before shaping but only after shaping using information provided by the CMs of the shaped structure(s). The pixelisation of Section 2.5.4 and 2.6.2 is still used, except that it uses an eigenvalue analysis to evaluate objective functions and not the output of driven electromagnetic analyses. All the shape-first feed-next approach has been for planar conducting surface antennas. In this thesis we extend it to fully 3D conducting surface antennas, and to the shaping of two closely-spaced antennas operating at different frequencies.

2.6.4 Computational Considerations

All of the above-mentioned shape synthesis methods need to utilize full-wave techniques of computational electromagnetics. If one remembers that during shape optimization such full-wave analysis needs to be done repeatedly, and possibly at several different frequencies each time, it becomes clear that this process will be computationally demanding, in spite of ever-improving access to powerful numerical processors. The burden of repeated full-wave analysis can often be relieved somewhat through the use of neural network modelling or space-mapping. However, these are better suited to size optimization[46], where the number of optimization variables is greatly reduced compared to the N_{bit} (in the hundreds) of them when using the shape optimization intended here. If the number of variables is larger than roughly 50, then the use of conventional neural networks has been reported to become problematic. Also, for the large number of variables being used here, it becomes difficult to ensure that the coarse model (in space mapping) faithfully "follows" the fine model with respect to all such variables. As a result, the so-called direct matrix method (DMM) was developed in [JOHN99a] and [JOHN 99b] to speed up computation. The DMM can be explained as follows: Suppose we have an EFIE/MM model for any of the conductor shapes that might be constructed out of cells as indicated in Fig.2.5-1. In the DMM the Z-matrix for the object is constructed for the case when all cells are filled with conductor (the starting shape), and expansion functions have been put in place over the entire object. We will call this $[Z_{start}]$. In successive iterations of the shaping process different potential shapes, obtained by removing conductor from some of the cells, are created in each generation. Each such shape will have its own Z-matrix that is a reduced version of $[Z_{start}]$; in other words the reduced Z-matrix can be constructed from elements already existing in $[Z_{start}]$ and so do not need to be re-computed. This saves computation time. It of course requires careful manipulation of the Z-matrix. It will be used in the new developments in Chapter 3.

---

[46] Where they have resulted in quite superb design routes.

2.7 CONCLUDING REMARKS

We began this chapter by pledging the interest in this thesis work to be that of shape synthesizing antennas that are electrically-small or of intermediate size. Section 2.2 defined the antenna performance measures that will be needed in what follows. Sections 2.3 and 2.4 identified the computational electromagnetics modelling concepts that will be used in the work. The shaping process always has some sort of optimizer at its core, and so the genetic algorithm, the optimization algorithm of choice in this thesis, was briefly described in Section 2.5.

Finally, Section 2.6 reviewed existing shape synthesis work on electrically small conducting antennas, from which a number of conclusions can be drawn. Firstly, no shape synthesis method that does not constrain the location of the feed-point prior to shaping has been available for fully three-dimensional (3D) conducting surface antennas[47]. Chapter 4 applies a procedure to do this for the first time[48]. Chapter 3 develops the new computational tool needed to achieve this. Secondly, such shape synthesis methods have not been applied to the problem of two closely-spaced antennas, operating at different frequencies. The contribution of Chapter 5 fills this void. Chapter 6 does not undertake the devising of any new synthesis method, but instead identifies and demonstrates a novel way of finding the sub-structure characteristic modes of a conducting object in the presence of an electrically very large second object using a hybrid MM/GTD scheme.

---

[47] As noted in Section 2.6, by calling them thus, we distinguish them from conducting thin-wire antennas.

[48] Reasons why this might be of interest in practice are given in Section 4.1.

CHAPTER 3

Construction of a General Shape Synthesis Tool

3.1 PRELIMINARY REMARKS

A tool that applies the DMM technique[49], and incorporates the characteristic mode route to allow a "shape-first feed-later" approach to be used, for the shape synthesis of 3D conducting surface antennas, has not been available. The development of such a tool was needed to achieve the goals of this thesis. It is the subject of this chapter, and will be described in terms of the following essential elements :

- ■ Section 3.2 - Selection of the CEM Engine
- ■ Section 3.3 - Selection of the Optimisation Algorithm
- ■ Section 3.4 - Shaping Manager : Part I
- ■ Section 3.5 - Geometry of Starting Shape, Shaping, and Shaping Constraints
- ■ Section 3.6 – Connecting Expansion Function, and Geometry, Chromosomes
- ■ Section 3.7 – Characteristic Mode Eigenanalysis
- ■ Section 3.8 - Objective Function Definition
- ■ Section 3.9 – Customization of the Shaping Prescription
- ■ Section 3.10 – Feed Point Selection & Triangle Removal After Shaping
- ■ Section 3.11 – Supplementary Antenna Performance Computation
- ■ Section 3.12 - Shaping Manager : Part II
- ■ Section 3.13 – Concluding Remarks

It will become clear as this chapter proceeds that the 3D shape synthesis tool in question consists of far more than "merely" the optimization algorithm, or simply running the CEM engine.

The nature of the material in this chapter is such that the use of footnotes greatly facilitates explanations, and hence footnotes will be used freely. Without them the explanations soon become unacceptably convoluted.

---

[49] The DMM is described in Section 2.6.4.

3.2 SELECTION OF THE COMPUTATIONAL ELECTROMAGNETICS ENGINE

Any shape synthesis tool needs a CEM engine that, given a certain conductor geometry, is able to compute all related current densities and fields on demand. If research of the type described here is ever to be taken to the point where it might be used in engineering practice, one has to use a commercially available electromagnetic simulator and optimisation algorithm software. These are not only vastly more powerful than most "in-house" simulators, but are available to others as well. In order to do this it is necessary to develop a deeper insight into the operation of such codes than might otherwise be required for conventional use of the codes. Several commercial software tools are available that use a Method of Moment (MoM) formulation for full-wave electromagnetic analysis[50]. Access to the details of the MM formulation, such as the mesh geometry, its association with the expansion functions used, and other "book-keeping" details, as well as the impedance matrix [Z], is typically restricted in commercial codes for proprietary reasons. However, access to [Z] is required in order to apply the DMM approach, and to perform sub-structure CM analyses[51]. Access to the vertex coordinates of the triangles in the mesh, and expansion function numbering, is needed in order to be able to manipulate the geometry as the shaping proceeds. The commercially available CEM code [FEKO] was selected because it has the enlightened attitude of giving the user access to resource files that provide this information[52]. Sub-algorithms and associated scripts were developed[53] to link each expansion function with the geometrical data on its associated pair of triangles, as will be detailed in Section 3.8. The selected CEM engine uses a mesh of triangles over the conducting objects, and RWG expansion functions, as described in Section 2.3.4.

3.3 SELECTION OF THE OPTIMISATION ALGORITHM

Many researchers have developed in-house genetic optimization algorithms. As with the CEM engine selected, our approach is similar to that in a measurement laboratory where one simply uses a vector network analyser (VNA) rather than develop such a piece of equipment oneself. So we have selected a particular "make" of GA, namely that available in the MATLAB optimization toolbox. As is the case of our use of the commercially available CEM engine (FEKO), utilization of the commercially available GA algorithm (in

---

[50] This work relies on an ability to find the characteristic modes of a structure. The MM is the only one that currently allows this to be done reliably.

[51] Detailed in Section 2.4.3.

[52] Resource files with such information is not available from other commercially available CEM codes.

[53] This was a considerable and far from straightforward task, and hints at reasons why others might not have attempted 3D conducting surface antenna shaping. We believe that the reason the shape synthesis of 3D conducting surface antennas has not been reported in the literature might be that the CEM engines used have typically been in-house codes, with limited geometrical ability.

MATLAB) has allowed the development of a shape synthesis tool that can be accessible to others. It can benefit from the superior coding practices in such software, as well as future upgrades. The performance of any GA is always problem-specific, and its degree of success depends on the use of just the correct settings of the various parameters[54] already mentioned in relation to the GA in Section 2.5.4. The GA in MATLAB allows one to experiment with these settings. This has been done, and will be discussed for the class of problems of interest in this thesis in Section 3.9.

3.4 SHAPING MANAGER – PART I

In the remaining sections of this chapter we will describe the steps/processes required to completely perform the antenna shaping. These are all implemented as MATLAB scripts that collectively form what can be called the "shaping manager", which controls the overall shape synthesis procedure. More will be said about the capabilities of the shaping manager in Section 3.12 once the above actions it controls have been individually described. In the latter descriptions, when we name the operation (eg. "the conducting surface is meshed") we mean the shaping manager instructs FEKO or the GA to do so under its control, or performs the operation itself.

Although they are technicalities, it is worthwhile naming where the required pieces of data can be found in FEKO resource files, since it is not mentioned elsewhere in the thesis. The (x_n, y_n, z_n), $n = 1, 2, 3$, of the vertices of each triangle are available in FEKO resource file **.cfm*. The data are written in ASCII format, and so must be converted to text format (that is, what MATLAB refers to as 'double format', which simply means 'numbers') for further processing by the MATLAB-based shaping manager. The FEKO resource file **.out* is a text file containing information on the number of triangles, the triangle numbering and the placement of the expansion functions onto the mesh. It also becomes populated with true output such as current densities and fields; in the present context this means after a characteristic mode analysis during shaping or after a driven analysis once the shaped antenna is known. The shaping manager needs to pick out the specific information that is needed from this file at various stages in the shaping process. The FEKO file **.mat* contains the impedance matrix[55]. As with the other files mentioned, such **.mat* files are opened by a MATLAB script (that forms part of the shaping manager) that does the data format conversion, and thereafter assembles the impedance matrix terms into a recognisable "matrix format".

---

[54] The settings for the population size, selection, crossover, mutation and migration mentioned in Section 2.5.4.

[55] As mentioned in Section 3.2, such information is not accessible to users of other commercial codes, at least not at the time of writing of this thesis.

3.5 GEOMETRY OF STARTING SHAPE, SHAPING, AND SHAPING CONSTRAINTS

We imagine a fictitious specification that requires an antenna to be designed subject to the restriction that it only occupy some surface of arbitrary shape, or collection of sub-surfaces. At the start of the shaping process these surfaces are considered to be completely occupied by conductor, and referred to as the *starting shape*. The shaping procedure synthesizes an antenna by removing portions of conductor from this starting shape.

Once the starting shape and centre-frequency of operation (f_o) have been specified, the starting shape is meshed into N_Δ triangles. We ensure that the mesh is sufficiently dense to guarantee both the accurate representation of the computed current density and the geometrical resolution desired. The number and layout of triangles sets the number of edges common to two triangles. There is an expansion function associated with each such common edge[56], of which there are N_{dof} in number[57]. The number of bits in an expansion function chromosome[58] (eg. [10110011100…..0100]) that is manipulated by the GA is denoted[59] by bits N_{bit}. In other words, each bit indicates the presence or absence of an expansion function and not the presence or otherwise of a triangle[60]. Thus as the GA performs the shaping it is removing and/or returning particular expansion functions rather than triangular elements. Once the shaping process is complete the expansion functions that remain are known. The mapping between each expansion function and its triangle pair allows one to determine what triangles (that is, pieces of conductor) remain; this mapping is described in Section 3.6.

The location of the expansion function bit in a chromosome, and the geometrical location of the expansion function on the actual conducting surface geometry, are roughly[61] related so that, as often as possible, adjacent bits in an expansion function chromosome imply almost-adjacent geometrical location of these functions. This allows us to approximately interpret the behaviour of the GA process in physical terms, which will be useful in the discussion in Section 3.9.

---

[56] Recall from Section 2.3.4 that a tringle can thus have up to three different expansion functions defined on it. In general $N_\Delta \geq N_{\text{dof}}$.

[57] The shaping manager immediately instructs FEKO to generate the MM matrix $[Z_{\text{start}}]$ of the starting shape. As the shaping proceeds the value of N_{dof} will change from its value for the starting shape, as the geometry (and hence N_Δ) is altered.

[58] That we will show in Section 3.8 can be one-to-one mapped to a geometry chromosome that defines a particular antenna shape.

[59] In general $N_{\text{bit}} \leq N_{\text{dof}}$, as will be explained in the last paragraph of this section.

[60] We will later, in order to facilitate discussion in Section 3.8, also refer to geometry chromosomes in which a 1 or 0 indicates the presence or absence of a triangle. It will be of length N_Δ and denoted in parentheses *viz.* {100110101…….001} instead of square brackets.

[61] Because the expansion function chromosomes and geometry chromosomes are not of the same length.

There may be certain portions of the starting shape that we insist must remain conductor and cannot participate in the shaping process. There may be many reasons for wanting this, including ones related to the fabrication of the shaped antenna, or the way it is to be assembled with associated circuitry, and so on. The shaping manager can be used to disallow participation of specified portions of the starting shape in the shaping process. In such a case $N_{\text{bit}} < N_{\text{dof}}$. The "disallowing" is achieved by keeping the appropriate locations in the geometry chromosome always set to 1, that is achieved as follows : The starting shape is built as a union of sub-geometries. This is done in a way that all fixed regions that may not be changed during shaping can be identified as a collection of specific sub-geometries. Although the complete starting shape is always described by the chromosome of length N_{dof}, those bits associated with the fixed region are prevented (by the shaping manager) from changing.

Of course, of certain portions of a surface must not contain conductor, one simply does not include such portions in the starting shape.

3.6 CONNECTING EXPANSION FUNCTION, AND GEOMETRY, CHROMOSOMES

Consider the chromosome[62] {1 1 1 1} that describes the starting object geometry[63] shown in Fig,3.6-1(a). The fact that each bit is a "1" means that each of the four triangles is "filled" with conductor. There are four common edges and so there are four expansion functions, each associated with a common edge[64]. The starting impedance matrix [Z] is therefore a 4×4 matrix. The expansion function chromosome of the starting geometry is [1 1 1 1].

Now suppose that in the shaping process triangle#1 is removed. The chromosome describing the altered geometry is thus {1 1 1 0}. With two expansion functions removed the reduced Z-matrix is 2×2, as shown in Fig.3.6-1(b). All terms needed for any reduced matrices that might arise are contained in the starting [Z].

---

[62] The position in the geometry chromosome is {Triangle#4 Triangle#3 Triangle#2 Triangle#1}. Observe that we are purposefully using parentheses {…} to represent this chromosome. Square brackets […] will be used to represent chromosomes that describe which expansion functions (not triangles) are present. The position in the expansion function chromosome is in the format [Expansion#4 Expansion#3 Expansion#2 Expansion#1] .

[63] Of course, in the actual shape synthesis work, there would be hundreds of triangles used to resolve a geometry. The four-triangle one being used here

[64] As outlined in Section 2.3.4.

The procedure just described in words must be implemented using the limited information available in the workspace files of the CEM engine. In this work we have done so using a binary logic approach, as the next set of bullets will explain[65]. The reader is once more referred to the geometry in Fig.3.6-1.

■ Each individual triangle (as opposed to expansion function) can be represented by chromosomes:

Triangle #1	{0 0 0 1}
Triangle #2	{0 0 1 0}
Triangle #3	{0 1 0 0}
Triangle #4	{1 0 0 0}

■ The FEKO output file gives the information which indicates the connection between these triangles and their expansion function indices, in the following format (annotated here for clarity):

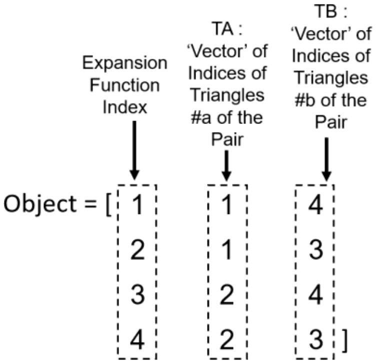

This shows that expansion function #1 (for example) is defined on the edge common to triangles #1 and # 4, and expansion function #2 is defined on the edge common to triangles #1 and #3, and so forth.

■ The TA and TB index 'vectors' for the entire starting geometry are converted to binary format:

TA
1 → 1 0 0 0
1 → 1 0 0 0
2 → 0 1 0 0
2 → 0 1 0 0

TB
4 → 0 0 0 1

---

[65] This is needed because we use the DMM approach; if not the process would not be as complicated. The reward is that, using the DMM, the $[Z]$ need be computed only once.

3 → 0 0 1 0
4 → 0 0 0 1
3 → 0 0 1 0

The above binary vectors are then added (adding in binary format implies an OR logic operation) :

TA • OR • TB

1 0 0 1
1 0 1 0
0 1 0 1
0 1 1 0

The outcome of the OR operation is then flipped :

1 0 0 1
0 1 0 1
1 0 1 0
0 1 1 0

Now suppose we have a chromosome of triangles {1 1 1 0}. This defines a specific conductor geometry. We wish to identify the corresponding chromosome of expansion functions in square brackets as [x x x x]. In order to do this, {1 1 1 0} undergoes an AND operation with each element in the array of the flipped TA • OR • TB quantities on the previous page:

{1 1 1 0} • OR • {1 0 0 1} = {1 0 0 0}
{1 1 1 0} • OR • {1 0 1 0} = {0 1 0 0}
{1 1 1 0} • OR • {0 1 0 1} = {1 0 1 0}
{1 1 1 0} • OR • {0 1 1 1} = {0 1 1 0}

or in other words

1 0 0 0
0 1 0 0
1 0 1 0
0 1 1 0

which, when rotated, becomes

1 0 1 0
0 1 0 1
0 0 1 1
0 0 0 0

The decimal addition of the bits in each complete column provides

1 1 2 2

A digit "1" signifies that there is no expansion function at the particular location in the expansion function chromosome, whereas "2" signifies the opposite[66]. The above digits thus tell us that expansion function chromosome associated with the triangle function chromosome {1 1 1 0} is [0 0 1 1]. Only expansion functions #3 and #4 are present. This fits with Fig.3.6-1(b).

The above process in essence does the following : Given the "barcode" for the expansion functions generate the associated barcode for the conductor layout, so that the conducting shape is known.

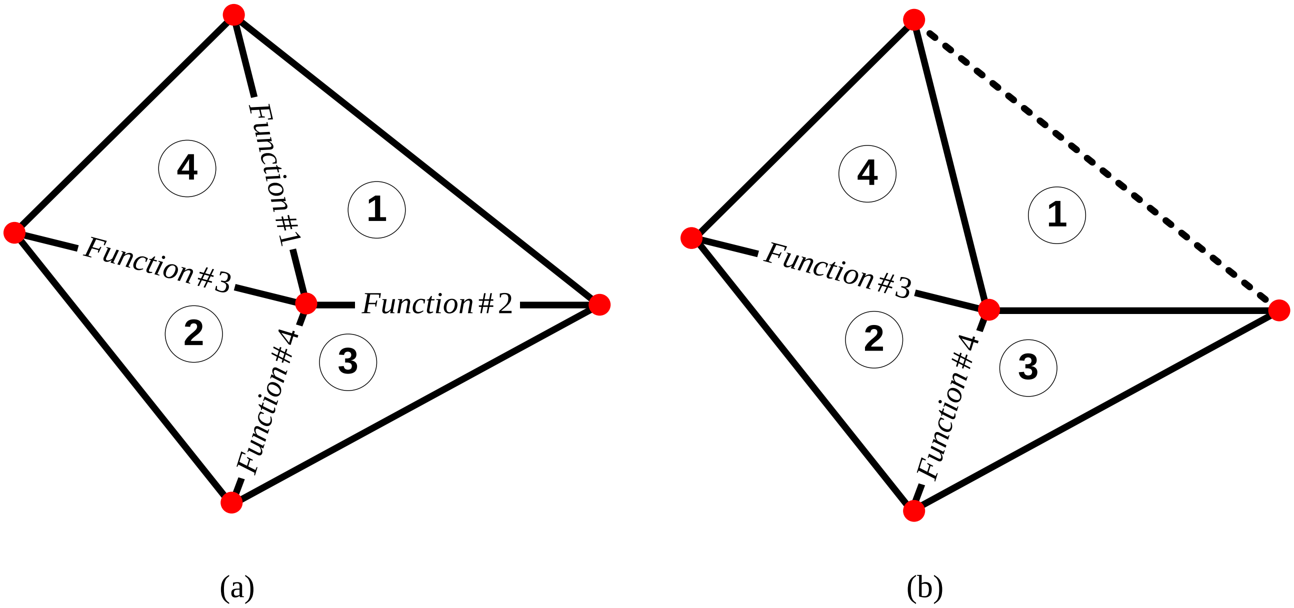

(a) (b)

Fig.3.6-1 : (a). Simplified unaltered geometry consisting of four triangles and four expansion functions and (b). with triangle#1 removed (as suggested by the dashed line). Triangle numbering is shown encircled. The red dots are the vertices of the triangles.

---

[66] This is true no matter how many triangles are present.

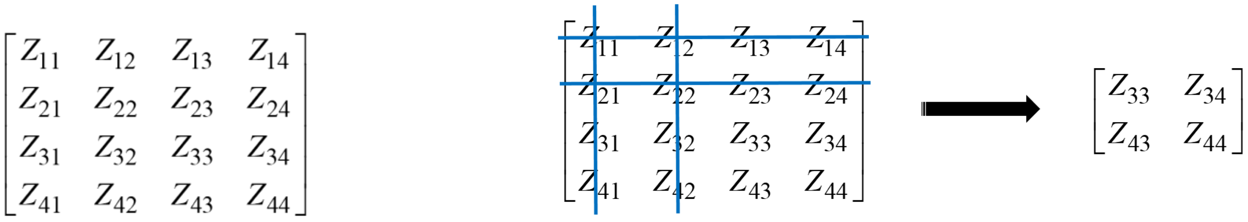
(a) (b)

Fig.3.6-2 : (a). MM impedance matrix [Z] corresponding to the unaltered geometry in Fig.3.6-1(a), and (b). the reduced MM matrix formation upon removal of expansion function #1 and expansion function #2.

3.7 CHARACTERISTIC MODE EIGENANALYSIS

If we require conventional characteristic modes of some shape, the shaping manager takes the reduced [Z] of the particular shape, separates it into real and imaginary parts, and solves the matrix eigenvalue problem of expression (2.4-1) using MATLAB eigenvalue problem routines. If we require sub-structure characteristic modes of some shape, the shaping manager takes the reduced [Z] of the particular shape, separates it into real and imaginary parts, and executes the matrix operations (2.4-16), (2.4-17) and (2.4-21) using MATLAB routines. This eigenanalysis of course supplies the column vectors $[J_n]$ that are the eigencurrents. FEKO does not support sub-structure CM analysis.

If at any stage[67] the associated eigenfields are needed the modal currents[68] $[J_n]$ are returned to FEKO by the shaping manager so that it can compute these fields. The eigencurrents $[J_n]$ of any shaped geometry will not be of the same length as the starting shape, because the starting shape has more expansion functions on it. In order to be able to export this reduced $[J_n]$ back to FEKO[69] to obtain current distribution plots and compute the fields due to it (i.e. secondary parameters), a special MATLAB script that is part of the shaping manager has been written that does the following: It alters the relevant FEKO resource files so that it accepts an altered geometry, and regenerates the (smaller) new $[Z]$ for this altered geometry[70]. It then converts the $[J_n]$ generated in binary format by MATLAB to a so-called **.str* file[71] in ASCII format that can be

---

[67] Albeit usually only once the shaping has been completed.

[68] Whether for conventional or sub-structure CMs.

[69] That allows us to fully exploit its superior post-processing capabilities.

[70] As a double-check, one can compare this $[Z]$ to the associated reduced $[Z]$ that had been obtained from applying the DMM. These should be identical. This was always found to be true.

[71] This is FEKO terminology.

interpreted by FEKO. Once this has been done FEKO is able to compute secondary quantities based on these current density values.

When using these column vectors of coefficients for the CM currents it is necessary to instruct FEKO to "only calculate the scattered part of the field"; this is an option provided by FEKO. The script must also explicitly request FEKO to read the current column vectors from the created *.str file.

In the case when sub-structure CMs are used, the shaping manager first concatenates $[J_n^{Asub}]$ and $[J_n^{B\sec}]$, as defined in Section 2.4.3, to form a single column vector of coefficients before sending it to FEKO for secondary parameter computation.

3.8 OBJECTIVE FUNCTION DEFINITION

Objective functions translate the design requirements into mathematical quantities that can be minimized by the optimization algorithm. Use of an algorithm that is not gradient-based allows one to use objective functions that are not merely simple classical mathematical function. It can also incorporate some sub-algorithm that can bias the decisions of the shape optimization algorithm based on known physical knowledge. At any rate, it is best to customize objective functions to the design targets of a specific shaping example. They are easily defined as a script in the shaping manager. Objective functions will therefore be revisited when particular shaping examples are discussed in Chapter 4 and Chapter 5. These can be easily incorporated into the shaping manager.

3.9 CUSTOMIZATION OF THE SHAPING PRESCRIPTION

We mentioned earlier that the parameter values needed for successful operation of a GA are always specific to the class of optimization problem. Such necessary details are most often not provided, even though they are essential if the reader wishes to repeat what has been described. Exhaustive testing of the shaping process done using a particular case[72] as a vehicle has resulted in the development of a customized adaptive approach to the application of the GA for antenna shaping. Although the outcome of this case will only be discussed in Section 4.2, the customized procedure that resulted from the numerical experiments on it are provided here in an effort to keep the thesis properly organized. It became the route that was followed in all subsequent shape synthesis examples.

When the GA was used with the default settings for its various parameters the shaping process either stagnated or, to put things plainly, the GA removed too much conductor too soon in its initial few iterations,

---

[72] Reported as Example #1 in Chapter 4.

and then did not seem able to put back conducting pixels in an acceptable number of iterations, when it "realised its mistake" in later iterations. Adjustment of the GA's parameters[73] such the crossover, mutation, migration direction, and so on, did not consistently improve matters. A comprehensive organized set of numerical experiments was clearly needed. The outcome was a structured procedure that successfully achieves the shaped antennas desired.

We have found that it is necessary to divide the shaping process into two parts, *a trial run*[74] and only then the *actual run*[75]. These are summarized in the flowcharts Fig. 3.9-1 and Fig. 3.9-2, respectively. They will next be elaborated on as a series of bullets written in the form of a 'recipe', and several other observations.

A. Trial Run – Flowchart#1

▪ Assume that the value of N_{pop} has been specified. The GA randomly generates a single beginning expansion function chromosome (call it $[C_{\text{init}}]$), and from this breeds an initial population of N_{pop} possible antenna shapes[76].

▪ Allow the GA to cycle through several generations, using default crossover, mutation and migration settings, until the value of F_{obj} has decreased substantially (eg. decreased by a factor of 10 or so). Halt the GA. Up to this stage the iterations of the GA are conventional.

▪ Select the chromosome with the smallest value of F_{obj}. Use this chromosome as the new initial chromosome C_{init} and start the GA afresh. If any chromosome in subsequent populations contains fewer 1's than C_{init} do not place it in custody[77]. Otherwise place it in custody and using, it as the next C_{init}, do a freshly-started GA run.

▪ Begin the fresh GA runs using this C_{init} with a crossover value[78] of 0.2.

▪ After the first iteration, record the value of F_{obj}

▪ Change the crossover value to 0.3, and complete another generation. Record the value of F_{obj}.

---

[73] These actions can be performed in a number of ways, usually controlled by a particular deterministic or probability function type that has to be chosen, and numerical values that define the details of the choice.

[74] The trial run finds a physically feasible "warm start" for the actual shaping run.

[75] The actual run eventually produces the shaped antenna.

[76] Even though it actually generates an initial population of N_{pop} expansion function chromosomes, we know from Section 3.8 that these can, when required, be translated into geometry chromosomes that each define a shape. Thus we will simply say that different antenna shapes are created.

[77] By placing a chromosome in custody we mean we record it for later possible use.

[78] This means 20% of the bits are kept fixed and 80% altered.

▪ Repeat this with increasing crossover values until a generation has been completed with a crossover value[79] of 0.8.

▪ Compare the values of F_{obj} of the collection of C_{init} chromosomes. Select the C_{init} in the set that gave the smallest F_{obj}, and the associated crossover value[80] that allowed it to be spawned. Use this C_{init} as the initial chromosome, and the crossover value, and then run the GA in the conventional way for very many generations. In other words, move to the next stage of the shaping process, namely the actual run.

B. Actual Run

The flowchart in Fig. 3.9-2 provides the entire list of steps for the actual run. Although it is not absolutely necessary, this author has done the following once the shaping procedure just described is complete (and hence F_{obj} small): The mesh is refined on the final shape (that is, for the final chromosome). This chromosome is then used as an initial chromosome C_{init}, the GA allowed to run for one more generation, and the value of F_{obj} for the bets population member observed. This was done for all the examples to be described in Chapters 4 and 5; it never altered the final shape.

C. Further Observations

▪ Both forward and backward migration should be attempted for the 3D antenna shaping problem. This is not necessarily the case with all physical problems.

▪ There are often rules of thumb stated, which in the present notation takes the form[81] $N_{\text{pop}} \approx m\, N_{\text{dof}}$, with suggested values provided for integer m. Experience in this thesis has made us believe that this should not be used as a general rule. The selection of N_{pop} has to be studied for particular classes of problem. This is seldom detailed in the literature. The best[82] values of N_{pop} for the antenna shaping problem has been established through supervision of the progress of the GA for several specific cases (when beginning form

---

[79] If the crossover value of larger than 80% too many bits are kept fixed for sufficient progress to take place.

[80] In all the shaping experiments carried out the best crossover value has been found to lie between 0.5 and 0.8.

[81] Because N_{dof} is the expansion function chromosome length, the expansion function chromosome being the ones directly acted upon by the GA.

[82] In the sense that it will actually lead to a shape that has a very small F_{obj}.

the starting geometry). We use $N_{\text{pop}} \approx 20$ in order to arrive as fast as possible at the stage where refined runs are performed. Only after doing so is the value of N_{pop} increased significantly.

▪ We have found that values of Tol (defined in Section 2.5.4) should be set to 10^{-12} in the actual run. The GA will stop if the changes to the value of F_{obj} of the best member of the population changes by less than Tol from one generation to the next.

▪ If one has fixed regions on the starting geometry it is observed that the GA takes longer to reduce the value of F_{obj}. This can be understood in the sense that one is interfering in the route the algorithm wishes to follow. In a sense one is "protecting" possibly weak members of the population. In such cases stagnation can occur unless the crossover values are adjusted slightly at different stages of the shaping process; this is one aspect falling within the *User Supervision* block in flowchart#2.

▪ In the same *User Supervision* block the mutation rate might need to be adjusted of necessary. In all the shape synthesis examples completed in this work we have found that mutation rates between 0.3% and 0.5% are satisfactory.

▪ In all the shaping experiments carried out the best crossover value has been found to lie between 0.5 and 0.8. The reason is clear. If the crossover value is 0.x (stated as x%), then (100-x)% of the bits in the chromosome are altered in generating new shapes for the next generation. Bits in chromosome locations close to each other are changed. This implies that expansion functions located geometrically close to each other are changed. If $x < 0.5$ we end up with too many shapes in a population that have far too little conductor, that we know for physical reasons are not going to give us what we need.

▪ In all the applications shown in this thesis the mating scheme employed is uniform crossover and the selection scheme used is tournament selection. The population size (N_{pop}) was held constant in all trial runs; although its value was experimented with in some actual runs (in an attempt to save electromagnetic simulation time) this is not really necessary.

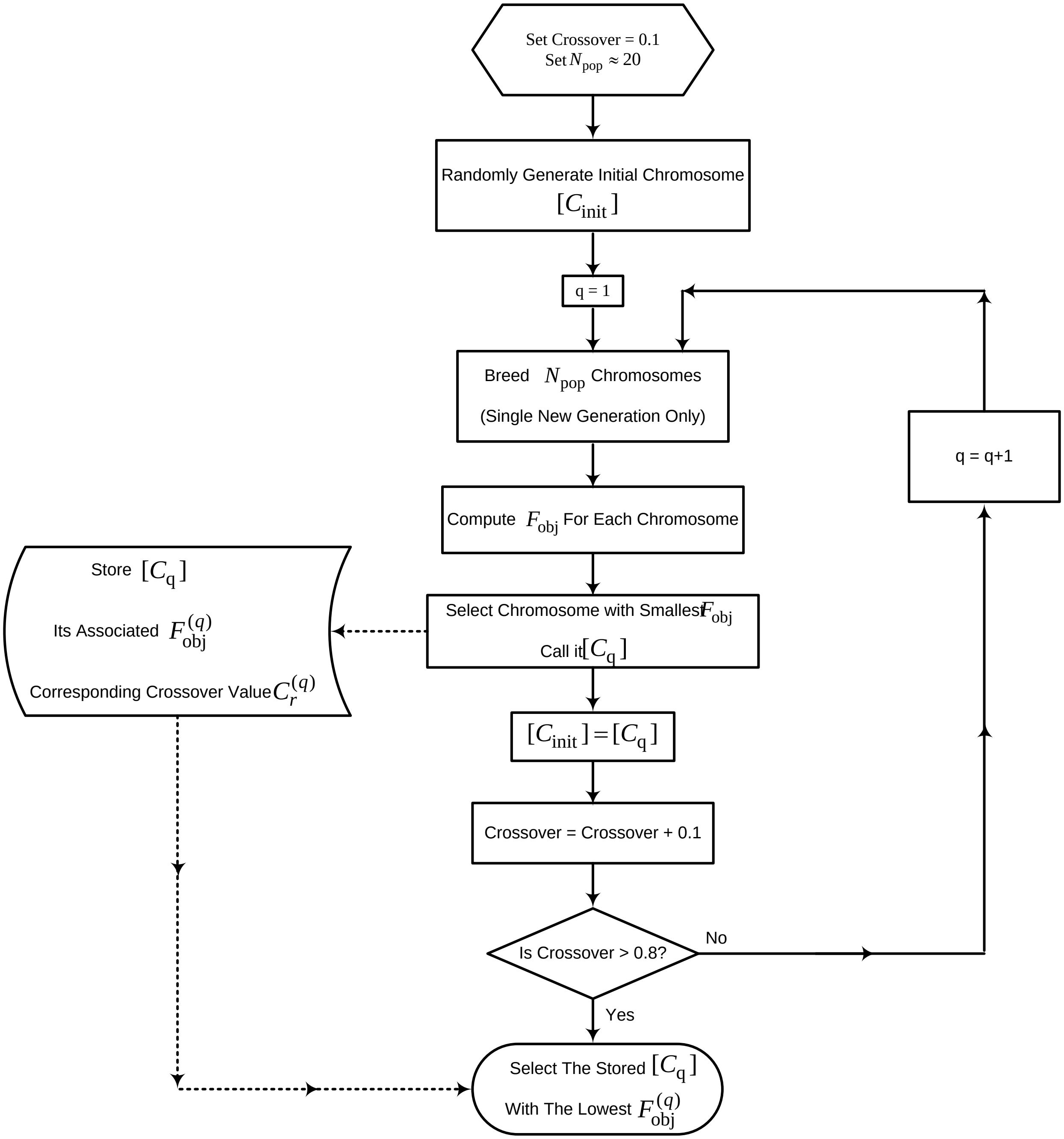

Fig. 3.9-1 : Trial Run - Flowchart#1

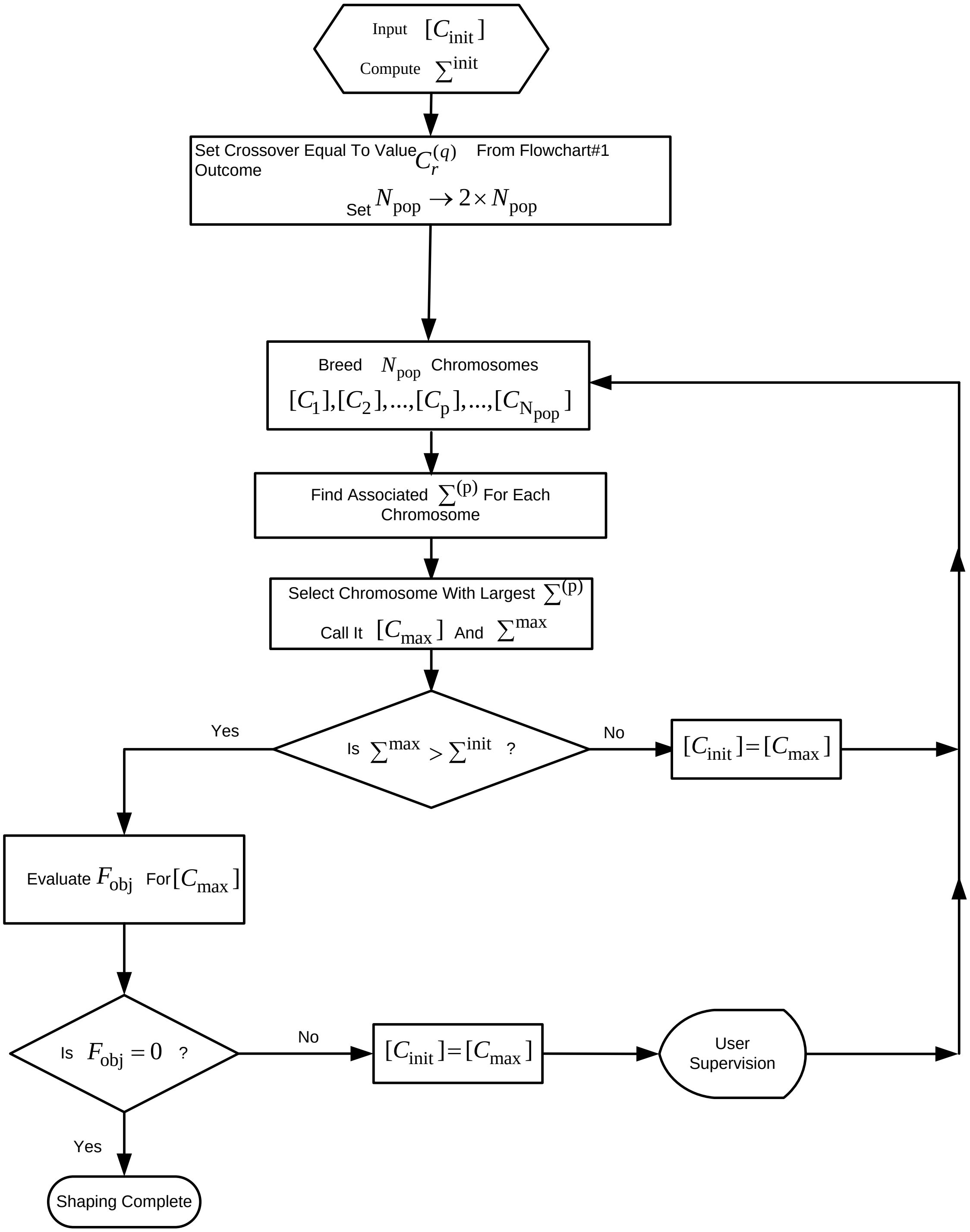

Fig. 3.9-2 : Actual Run - Flowchart#2

3.10 FEED POINT SELECTION & TRIANGLE REMOVAL AFTER SHAPING

3.10.1 Feed Point Selection

At the end of the shaping process the feed point must be selected on the shaped antenna[83]. This is determined based on the current distribution (in other words the column vector of coefficients) of the dominant CM on the antenna. In the shaping manager a script therefore simply search for the coefficient with the maximum value, and the known link (form Section 3.6) between the expansion function index and the geometry used to determine exactly where the feedpoint should be placed. Visual observation of the displayed CM current on the shaped antenna is not sufficiently precise to reliably select this location.

3.10.2 Removal of Islands & Vertex-Only Connections

When fabricating the antenna under consideration the synthesized shape that is produced by the shaping manager will contain triangles that are joined only at their vertices (vertex-only connections), or are not joined to any other triangles at all (islands). The RWG expansion functions[84] are so-defined that there is no current crossing such junctions. Such junctions must not be fabricated, since they would allow current flow through them and hence the fabricated model would not correspond to the electromagnetic model upon which the shaping was based. Such “vertex only” connections must therefore be separated slightly (“split”) in the geometry file before it is used as input to the fabrication process, to prevent such current flow. Furthermore, any single isolated triangles occurring in the shaped geometry must be removed; they will not have had any current on them (again due to the manner in which the RWG expansion functions are defined) during the simulations.

---

[83] After which a driven MM analysis is performed using FEKO to determine the antenna properties.

[84] Described in Section 2.3.4.

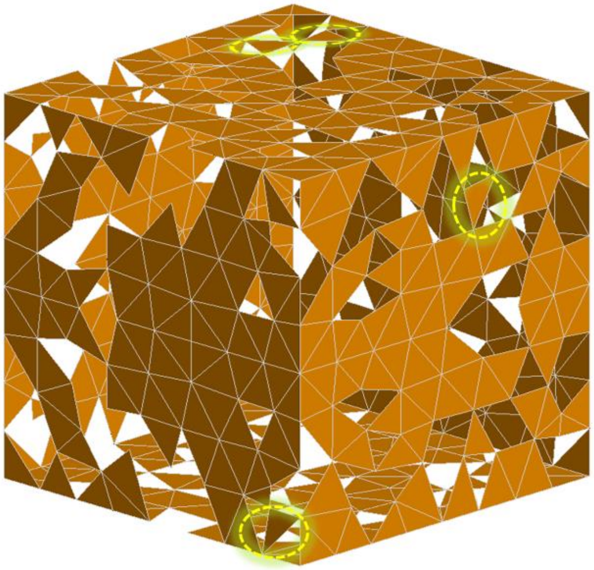

Fig.3.10-1 : Illustration of a shape-synthesized antenna with highlighted vertex-only connections.

3.11 SUPPLEMENTARY ANTENNA PERFORMANCE COMPUTATION

3.11.1 Quantities

Definitions of all the antenna performance parameters needed have been provided in Section 2.2. Most of these are provided directly by the chosen computational engine (FEKO). However, the mean effective gain (MEG), antenna quality factor (Q), and bandwidth-efficiency product ($B\eta_{rad}$) are not, and so scripts in the shaping manager were written to determine these once the shape synthesis of an antenna has been completed.

It is often easy to be mislead by colour-coded plots of the current density over a conducting surface of unconventional shape with which one is not yet familiar. In order to explain what we mean Fig.3.11-1 shows the current density on a centre-fed strip dipole. The current is high at the location of the source, and at the edges of the strip in the vicinity the source[85]. The temptation is to assume that the portions of the PEC strip (the ends in this case) where the current density is low are of little importance to the antenna operation, and are "not being used". Of course, we know from experience that these portions (physically connected[86] as they are to portions where the current density is higher) are essential for proper operation of the antenna,

---

[85] Current density parallel to a PEC edge peaks at the edge; the so-called *edge condition*.

[86] In a structure (not the dipole depicted here) containing small isolated pieces of PEC on which the current density is everywhere almost zero will indeed not play a significant role in the antenna operation.

because this is where most of the net electric charge density resides. This author had to continually recall this fact when observing currents on the unconventional shapes to be discussed in Chapters 4 and 5.

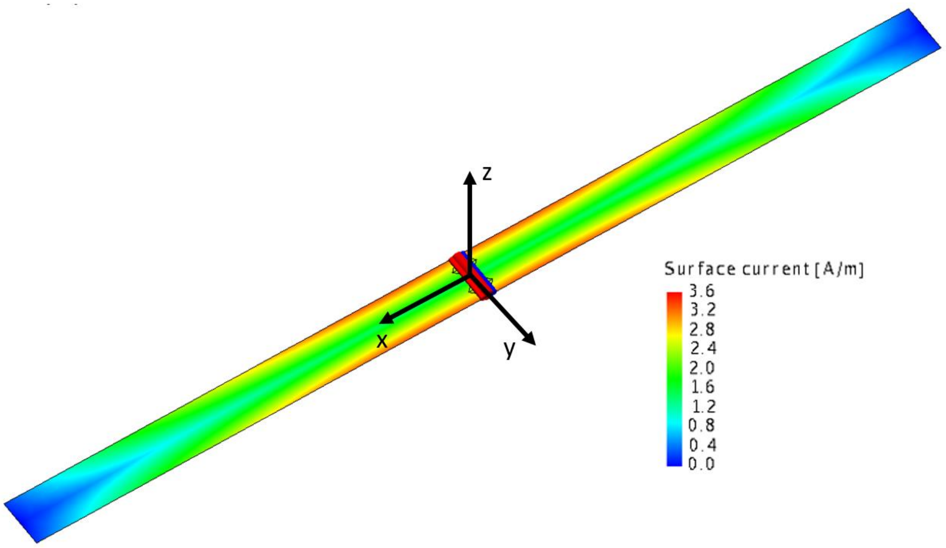

Fig. 3.11-1 : Current density on a centre-fed PEC strip of roughly one-half-wavelength.

3.11.2 Quality Factor (Q)

The actual quality factor is computed using the expression for Q_z given in Section 2.2.10. At any frequency f the derivatives $R'_{in}(f)$ and $X'_{in}(f)$ can simply be computed via first-order finite differences using values at frequencies a very small amount lower and higher, than the frequency of interest (eg. 1.5MHz “deltas” on either side of 1 GHz).

3.11.3 Mean Effective Gain (MEG)

The MEG is computed by the shaping manager using expression (2.2-47). The gain, or directivity functions and radiation efficiency, are extracted from FEKO by the shaping manager. One can define the angular probability density functions for a specific environment in the shaping manager. It then normalises them so that (2.2-50) and (2.2-51) are satisfied. The integrals in the definition of the MEG are then numerically computed the integration over S_∞. It is found that, for the relatively broad radiation patterns of the electrically small antenna under discussion here, values of $\Delta\theta$ and $\Delta\phi$ less than 1° allow the MEG integral to be evaluated accurately as a simple Riemann sum.

3.11.4 Bandwidth-Efficiency Product ($B\eta_{rad}$)

This quantity was defined in Part E of Section 2.2.10. The fractional bandwidth B is found from the actual $|\Gamma_{\mathrm{in}}(f)|$ curve, and the radiation efficiency as that computed by FEKO multiplied by a correction factor[87] if needed.

3.12 SHAPING MANAGER - PART II

The overall operation of the shaping manager is summarized by the flowchart in Fig. 3.12-1. As stated previously, it is implemented in MATLAB and is thus flexible enough to be built-upon if new requirements arise. It links the CEM engine and the GA algorithm, makes the changes to the geometry during shaping, performs the required CM analyses, evaluates the objective functions for each candidate geometry, is able to enforce symmetry or not during shaping. It is able to disallow shaping over portions of the geometry. Most of the shaping process is completed without having to continually appeal to FEKO; it is not necessary to re-compute the MM-matrix several times during each iteration of the GA because the DMM approach is used by the shaping manager. This is so unless the objective function includes not only CM eigenvalues but also the far-zone fields[88] of the CMs. The shaping manager is able to interpret FEKO resource files and hence can exploit all that FEKO is able to provide as far as electromagnetic computation, CAD capabilities for describing the geometry (which can be quite complex), and even the export of CAD files for fabrication purposes are concerned. The latter can also be used to designate parts of a complete object as Object#A and Object#B (or more) if the shape synthesis is to be done[89] using sub-structure CMs.

---

[87] The correction factor will be discussed in Section 4.2 and, as will be discussed there, Appendix A.

[88] As explained in Section 4.5.

[89] This will be done in Chapter 5.

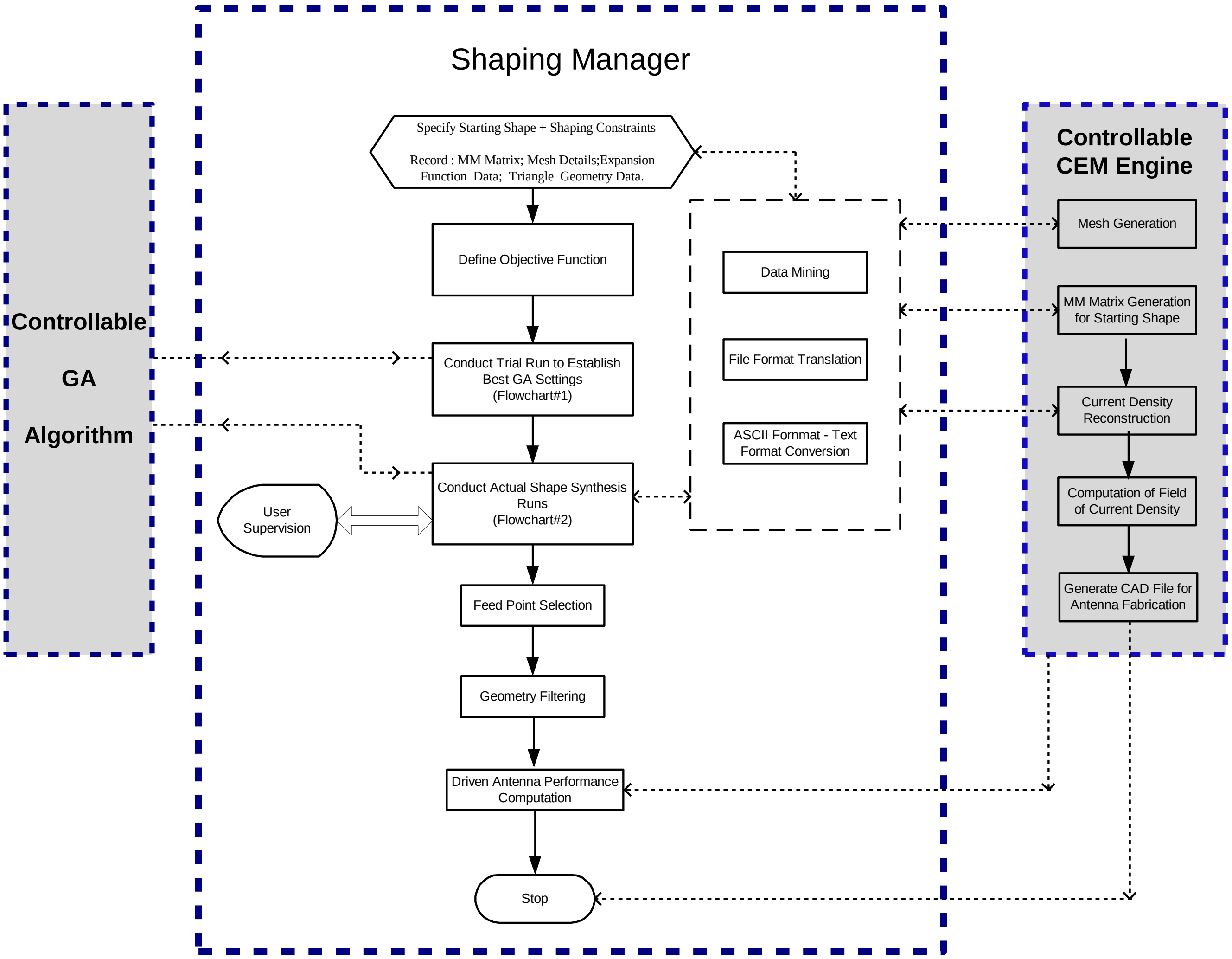

Fig. 3.12-1 : Shaping Manager - Flowchart#3

3.13 CONCLUDING REMARKS

Chapter 3 has developed the very complex machinery for a computational electromagnetics-based tool capable of performing the shape synthesis of conducting antennas. It has been developed in the form of a software shaping manager that controls the shaping process by exploiting a commercially available CEM engine and a commercially implemented genetic optimisation algorithm. This is an important step, because it allows, contrary to pixilation-based shaping implementations used by others, an ability to perform true 3D shaping of conducting surface antennas here for the first time. The use of a commercially available CEM engine (FEKO), and a commercially available GA algorithm (in MATLAB) has allowed the development of a shape synthesis tool that can be accessible to others. It benefits from their superior pre- and post-processing capabilities, and will so from future upgrades[90]. Another reason for using a commercial code such as FEKO is that files describing complicated shaped geometries can be exported for fabrication. However, it will hopefully have been appreciated from the description in this chapter that the shaping manager is considerably more than merely “running FEKO”.

One might wonder why the GA is used at all, and whether a simple direct search approach should be used. However, the number of permutations of the bits in a binary word of length m is 2^m. If m is on the order of 800 (which is less than that in the first example in Chapter 4) there will be an impossibly large number of arrangements to examine. This obviously discourages a direct search, since a full-wave electromagnetic simulation would be required for each of the population members (that is, antenna shapes) considered. The GA’s evolutionary approach much reduces the number of shapes that need to be “tested” in reaching a shape that is optimal according to the selected objective function.

---

[90] We believe that the reason shape synthesis of 3D conducting surface antennas has not been reported in the literature might be that the CEM engines used have typically been in-house codes, with limited geometrical ability.

CHAPTER 4

The Shape Synthesis of Non-Planar Conducting Surface Antennas

4.1 PRELIMINARY REMARKS

4.1.1 Outline of this Chapter

The review in Section 2.6 allowed us to correctly conclude that shape synthesis methods which do not constrain the location of the feed-point have not yet been available for, or hence applied to, fully three-dimensional (3D) conducting surface antennas. A full-wave based synthesis tool was therefore developed in Chapter 3 to enable the antenna designer to do this. In the present chapter several examples of the application of this synthesis tool are treated, and some experimental validation of the approach discussed. Chapter 3 has been written in such a way that descriptions of the set-up for these examples can be concisely laid down here in Chapter 4. The first shaping example, in Section 4.2, starts with an open cuboid shape and synthesises an antenna from it for self-resonance at a specified frequency. This, as well as the further examples considered in this chapter, confirms the validity of both the shaping idea for 3D conducting surface antennas, and the success of its implementation tool described in Chapter 3. The specific antenna (in Section 4.2) is fabricated and its performance measured, to demonstrate that the CEM modelling process is sound.

Sections 4.3 and 4.4 further demonstrate the successful application of the shape synthesis process, with their examples representative of how the starting shape could be altered (eg. to accommodate possible fabrication), and then when there is an inclusion (eg. battery) within the starting shape. Section 4.5 demonstrates a case where shaping is done, not only to achieve self-resonance (which it continues to do), but to simultaneously maximise the mean effective directivity (MED) of the antenna. Section 4.6 briefly mentions some possible extensions of the work of Chapter 4. The contributions of the work in this chapter are summarized in Section 4.7. Before proceeding to the shape synthesis examples it will be instructive to motivate the need for such 3D conducting surface antennas.

4.1.2 Some Motivation

There is much hyperbole associated with new technology, and the Internet of Things (IoT) concept is no exception. However, even if only a small percentage of this “hype” is eventually realized, it will represent an enormous industry, conservatively[91] estimated at around $300 billion annually. It is recognized [NEZA19] that the IoT is still in its infancy, and that details of its eventual structure and constituents are yet to be determined. There are challenges at all levels, involving virtually every discipline within electrical engineering. Indeed, there is even now an IEEE Internet of Things Journal. One aim of the Internet of Things is to allow embedded sensors to be connected to some host, so that once connected they can be supervised, tracked, and monitored via the Internet. What is certain is that there will be sensors on many devices that communicate with their data centres via the wireless network. Each sensor therefore needs an antenna and associated RF circuitry, because whenever communications takes place in a wireless, as opposed to a wired, manner, this is essential. The number of wirelessly connected devices is expected to grow to 50 billion[92] by 2020. The range of possible applications is summarized in Fig.4.1-1.

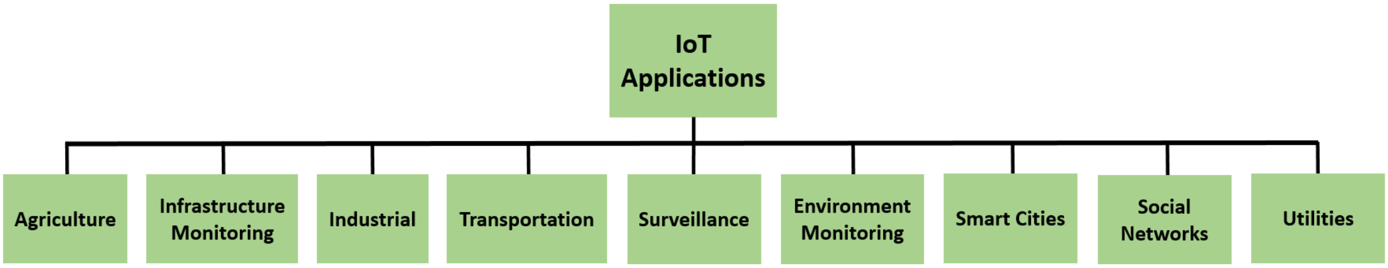

Fig.4.1-1 : Applications of the Internet of Things (Adapted from [NEZA19])

The type we have in mind in this work is antennas on such things as surveilllance cameras, weather monitoring stations, parking meters, road cones that alert the public to construction work ('smart' cones), and so forth. In such applications, if one can make the antennas electrically small, then they will also be acceptably physically small and allow use of the lower frequency ranges not crucial for future very high data rate communications. In such applications the goal is to have antennas on the surface of some package (eg. cuboid) capable of having sensor circuitry packaged within the antenna structure. This has resulted in the terminology "antenna-on-package" (AoP). Although it may be considered technically vague terminology, the trade literature describes the antenna requirements as providing "near isotropic" radiation patterns so that the sensor is not over-sensitive to orientation. It also mentions that the use of additive manufacturing techniques to make and fit, or directly deposit, the antenna on the package would be favourable.

---

[91] The conservative estimation process has consisted of extracting dollar figures from tens of websites, flyers in the trade literature, and statements by investors hoping to profit hugely, and simply averaging their predictions.

[92] This includes mobile phones and tablets. Thus some are even referring to the Internet of Everything (IoE) or Internet of People (IoP). However, IoT is apparently the term accepted in the engineering community.

There are only a limited number of references directly related to electrically-small 3D conducting surface antennas[93] on a package of the type in mind in the present work. Good representative examples are those reviewed below:

[KRUE 09] : The antenna consists of a non-conducting cube into which three meander-line dipoles, fed using T-match configurations, have been folded. The antenna has $ka = 0.5169$, has a measured $\eta_{rad} = 75\%$, and a -10dB bandwidth of 1.3%. The authors refer to this as "smart packaging" because sensor equipment may be integrated inside the cube's hollow interior.

[NASS 12] : The antenna consists of a meander-line dipole folded onto a non-conducting cube which "makes available the cube interior for sensor electronics equipment. Two antenna were designed. The antenna with $ka = 0.55$ had a measured $\eta_{rad} = 78\%$, and a -10dB bandwidth of 2%. The antenna with $ka = 0.45$ had a measured $\eta_{rad} = 73\%$, and a -10dB bandwidth of 1.5%.

[ADAM 15] : The authors discuss the 3D printing – direct writing of silver nanoparticle ink - of a spherical dipole onto a non-conducting spherical shell, using 3D printing. The with $ka = 0.367$ had a measured $\eta_{rad} = 57\%$. It should be remembered that silver nanoparticle ink has a much lower conductivity than conventional printed circuit board copper.

[LIU 16] : The antenna consists of a meandered loop antenna whose plane is located at the (vertical) centre of the a cubic package. The antenna has $ka \approx 0.12$, a measured $\eta_{rad} = 22\%$, and a -10dB bandwidth of 1.1%. Electrically, this antenna is extremely small. It is not self-resonant, and needs a lumped component matching network.

[SU 18] : The antenna consists of meander-line antennas folded onto a non-conducting rectangular package. The antenna has $ka = 0.78$, and was constructed using additive printing onto a flat surface that is then folded onto the package and any required connections made using conductive epoxy. The emphasis in the paper is that the resulting antenna patterns are near-isotropic, and the fact that dimensions on the antenna were

---

[93] None of which can be considered to have been shape synthesized.

(manually) altered in trade-off studies to obtain the said behaviour in the presence of a battery inside the supporting package.

In all of the above instances the design process consisted of using conventional antenna geometries and folding them to conform to a prescribed host surface. The resulting changes in the antenna behaviour are accepted as inevitable, and matching networks are sometimes needed. In this chapter we will demonstrate that, with the shaping tool of Chapter 3 now available, the intended surface of some package can be specified (with portions designated as a starting shape for the eventual conducting surface antenna), and we can let the electromagnetics guide the shape synthesis of the antenna so that it is self-resonant at some frequency of interest.

4.2 THREE-DIMENSIONAL SHAPE SYNTHESIS EXAMPLE #1 : OPEN CUBOID ANTENNA

4.2.1 Preamble

This example was chosen to serve as the *test object* on which to run computational experiments in an effort to observe and understand the behaviour of the proposed shaping process, in particular the manner in which to use the genetic algorithm. An enormously large number of runs were made and the progress (or lack thereof) observed. The result was the customization that has already been described in Section 3.9. The results shown here[94] are the outcome when this customization was finally implemented. Furthermore, we used $ka \approx 1$ for this test case. Such an antenna is on the border of the usual "electrically small" designation, and could be said to be of intermediate electrical size. Such an antenna, susceptible as it is to not being single-mode[95], represents a slightly more tricky shaping problem when using the shape-first/feed-next approach, and thus serves as a good test case. Subsequent examples have much smaller values of ka.

4.2.2 Starting Geometry

The starting shape is the non-planar cuboid with one face removed, as shown in Fig.4.2-1. The centre frequency is $f_o = 2GHz$, at which the wavelength $\lambda = 150\,\text{mm}$, and so the sides[96] are each of electrical dimension $d = 30\text{mm} = \lambda / 5$. The radius *a* of a sphere that just encloses a cuboid of sides *d* can be shown to be $a = (\sqrt{3}/2)\,d$. Thus we here have $a/\lambda = 0.1732$ and hence $ka = 1.09$. The starting shape is densely

---

[94] And indeed for all shape synthesis examples to be given in this thesis.

[95] In the sense defined in Section 2.6.3.

[96] There is no groundplane. A "half-wavelength" self-resonant dipole operating at the same frequency would have to have a length $0.48\lambda = 72\text{mm}$ and have (as noted in Section 2.2.2) $ka = 1.57$.

meshed into $N_{\Delta} = 860$ triangles. This results in an initial $N_{\text{dof}} = 1023$, and implies that the average length of any side of the triangles in the mesh is 2 mm, which is well below $\lambda / 60$. This very fine mesh was selected so that we could experiment with the shaping process prescription without having to be concerned about the accuracy of the electromagnetic modelling. It also provides good geometrical resolution.

We selected the starting shape to be open at the bottom to emphasize that it can in fact be any shape whatsoever; the implication in this case is that such a starting shape would ensure that the final synthesized antenna can easily be assembled by pushing it over a package. Furthermore, we envisaged that the intention is to have the antenna fabricated out of a flat sheet of copper and then folded into a structurally rigid form[97]. We therefore instructed the shaping manager to disallow the removal of triangles on either side of all edges in the shaping process. A lower number of optimization variables always makes the shape synthesis process slightly "tougher"; but we have not been able to quantify this in any way. No symmetry was enforced during the shaping process.

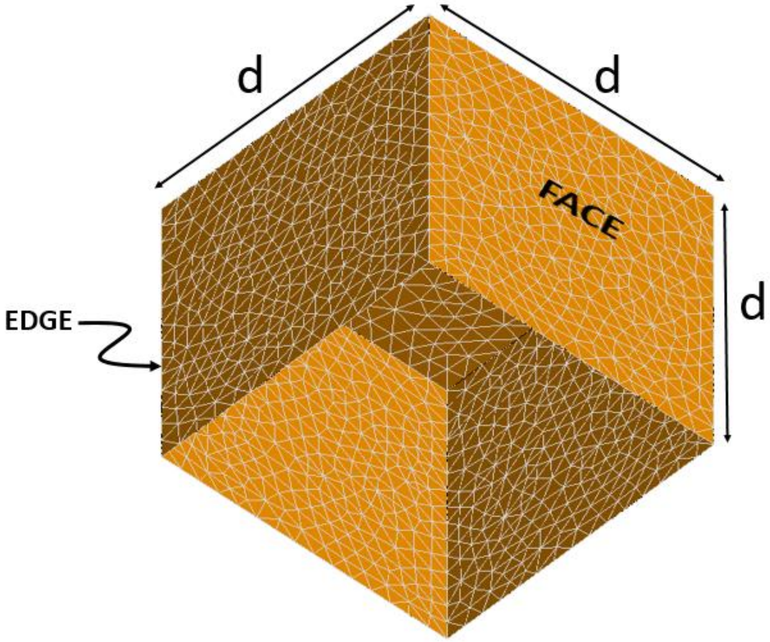

Fig.4.2-1: Starting non-planar cuboid 3D conductor shape with bottom face removed, and sides of dimension $d = 30\,\text{mm}$. Diagram shows tilted cuboid viewed from below.

---

[97] Further comments on how alternative intended fabrication methods might be accommodated by the choice of the starting shape, or constraints, are made in later sections of this chapter.

4.2.3 The Objective Function

The objective function used was simply

$$F_{obj} = |\lambda_1(f_o)| \qquad (4.2\text{-}1)$$

with $|\lambda_1(f_o)|$ the magnitude of the CM with the lowest eigenvalue at f_o. The range of possible values is $0 \le F_{obj} < \infty$. The reasoning is that, as long as the structure is indeed a single-mode one, a low $|\lambda_1(f_o)|$ value will signify that the shaped structure is resonant in a CM-sense, and it will then be possible to find a feed point with respect to which, as an antenna, it will be self-resonant[98].

4.2.4 Outcome of the Shape Synthesis Process

The shaping procedure flowcharted in Chapter 3 was followed. Fig.4.2-2 reveals that the shaping took roughly $N_{\text{gen}} = 250$ generations to converge. The value of $|\lambda_1(f_o)|$ reached was 0.004. Fig.4.2-3 is a plot of a normalised eigenvalue $|\lambda_n|^{dB} = 10\log\{|\lambda_n|/|\lambda_1|\}$. It is clear that the lowest eigenvalue is orders of magnitude lower than that of the other CMs. The synthesized shape is that in Fig.4.2-4, which also indicates the location of the feed, found using the approach described in Section 3.10.1. The surface current density distribution of the lowest CM is depicted in Fig.4.2-5 (a) through (c), and shows pictorially why the feed location turns out to be where it is; we wish to excite this particular CM strongly to ensure self-resonance at f_o. Note that these are eigencurrents. The current for the driven structure is that in Fig.4.2-5(d); the driven structure will be discussed in the next section.

---

[98] If the modal Q-factor were to be included as part of the objective function this could allow the bandwidth to be maximised subject to the given constraints.

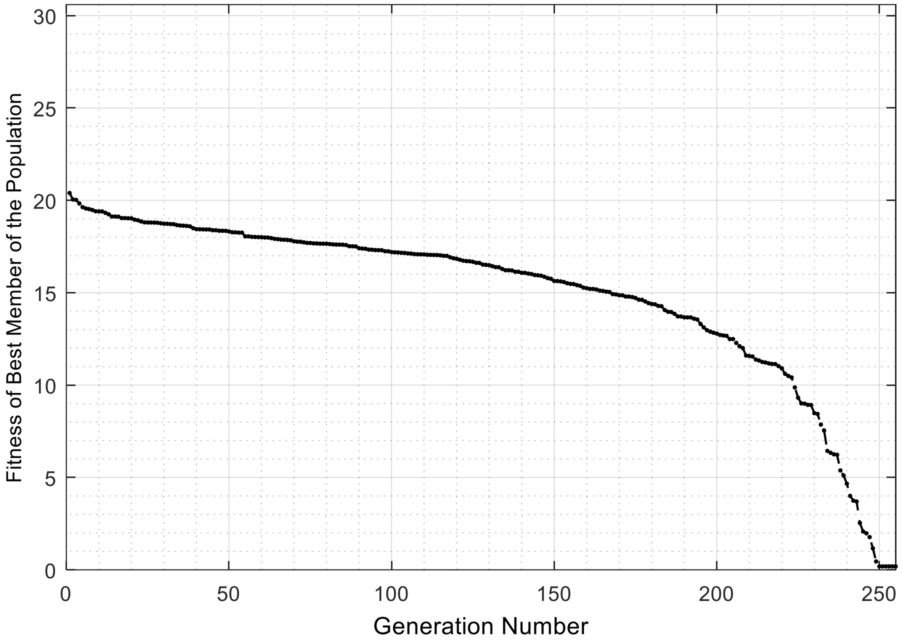

Fig.4.2-2 : Progress of the value of the objective function (fitness function) of the fittest member of the population as a function of generation number in the “actual run”.

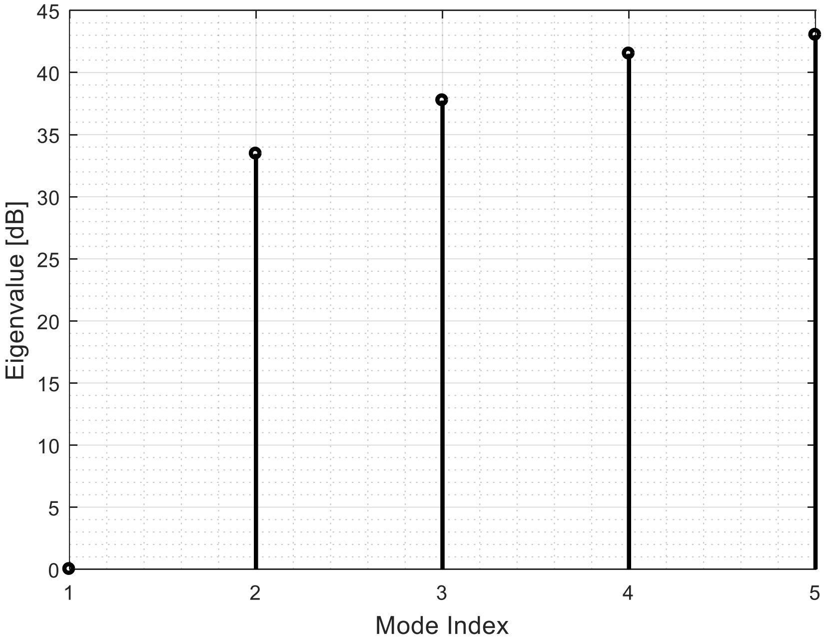

Fig.4.2-3 : Eigenvalues $|\lambda_n|$ vs mode index *n* for the final shaped antenna at f_o, normalised to $|\lambda_1|$ and expressed in decibels.

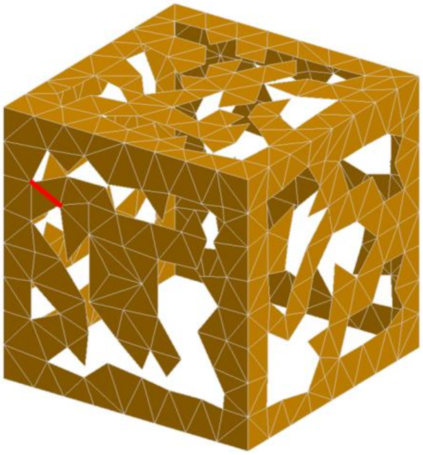

Fig.4.2-4 : Shape-synthesized antenna geometry. The feed point is indicated by the red bar.

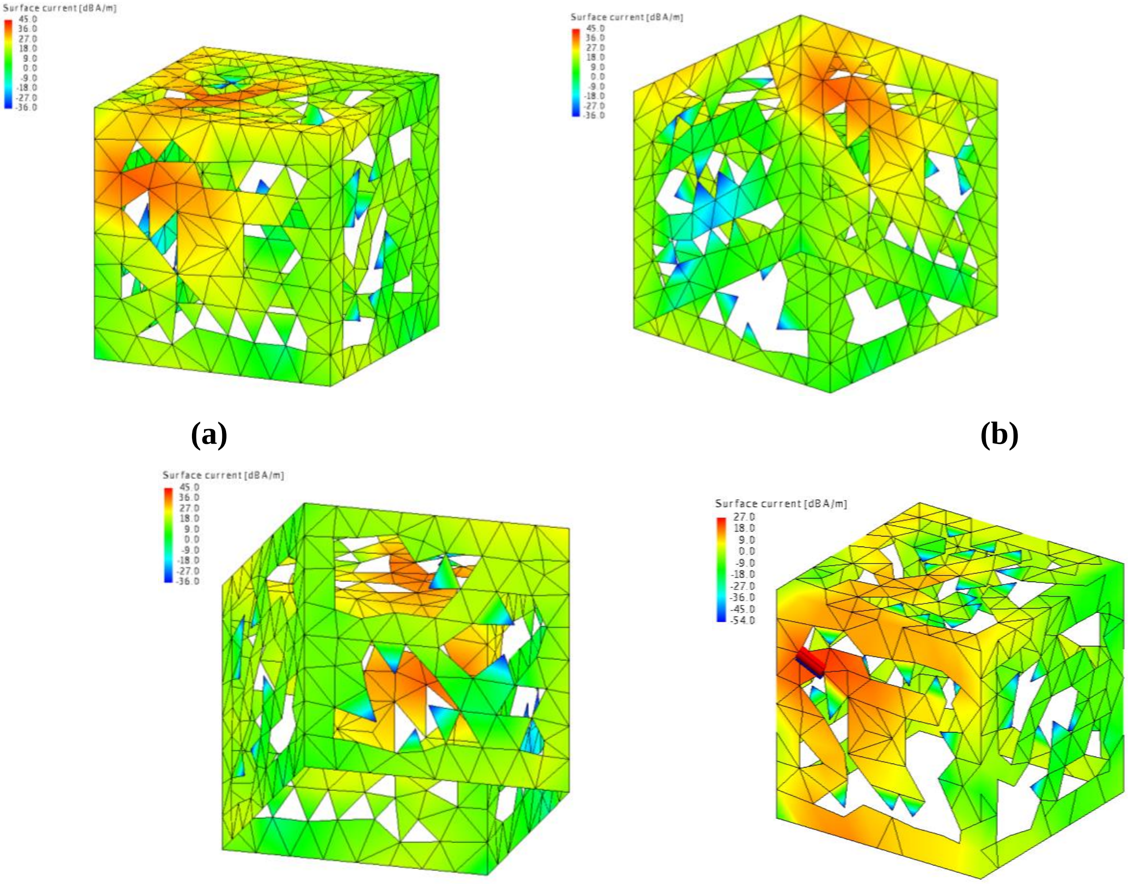

(a) **(b)**

(c) **(d)**

Fig.4.2-5 : Three views, at frequency f_o**,** of the current density of the lowest order CM on the shaped structure in Fig.4.2-4 are shown in (a) through (c). The current distribution on the driven shaped antenna is that in (d), and is referred to in Section 4.2.5.

4.2.5 Computed Performance of the Shaped Antenna

With the feeding location selected, we can proceed to simulate the shaped structure as a driven problem to obtain the input impedance and reflection coefficient, radiation efficiency and antenna quality factor at frequency f_{o} and hence assess how successful the shape synthesis has been. It is clear from the modal weighting coefficients shown in Fig.4.2-6 that, with the feed located as shown in Fig.4.2-4, the antenna is indeed a single-mode structure. Higher-order CMs are all excited at levels around 20dB or more lower than the dominant lowest one.

The computed input impedance in Fig.4.2-7 confirms that at $f_{\mathrm{o}} = 2\,\mathrm{GHz}$ (or 1.997 GHz to be precise) the antenna is self-resonant, with $X_{\mathrm{in}} \approx 0$ and $R_{\mathrm{in}} = 47.3\Omega$. As expected, the input reflection coefficient $|\Gamma_{\mathrm{in}}|$, referenced to 50Ω, is very low in the vicinity of f_{o}. This can be seen from Fig.4.2-8. Computed radiation patterns[99] are shown in Fig.4.2-8. Fig.4.2-8(a) has been included for convenience in recognizing which cuts are being referred to. The azimuthal pattern cut is that in Fig.4.2-8(b); it is seen to be almost omni-directional in this plane. Two elevation cuts are shown in Fig.4-2-8 (c) and (d), namely the xz- and y-z-planes respectively. Such broad patterns are expected of an antenna with $ka \approx 1$ and are highly desirable for sensor applications. Additional computed performance measures will be referred to Section 4.2.6, in relation to their measured values for the fabricated version of this antenna.

Fig.4.2-7 reveals that there is an ordinary resonance at 1.76 GHz, but that $R_{in} \approx 3\Omega$ there, which is very low. Interestingly, the shaping procedure automatically selected the anti-resonance point with the higher R_{in} value without user intervention. If bandwidth maximization were to be included in the objective function (see comments later) then it might very well select the ordinary resonance and deliver the low R_{in} to us. At frequencies below 1.76GHz the input resistance (and hence radiation resistance) drops quickly towards zero, whereas X_{in} becomes increasing negative (capacitive).

---

[99] The maximum total gain was computed to be 2.8 dBi.

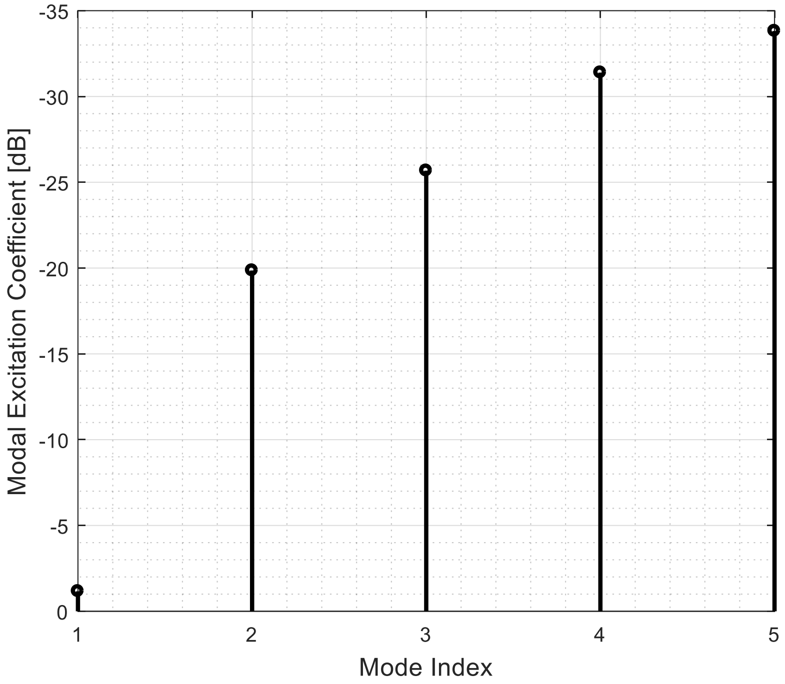

Fig.4.2-6 : Modal excitation coefficient ($|\alpha_n|$) vs. mode index (n) at f_o.

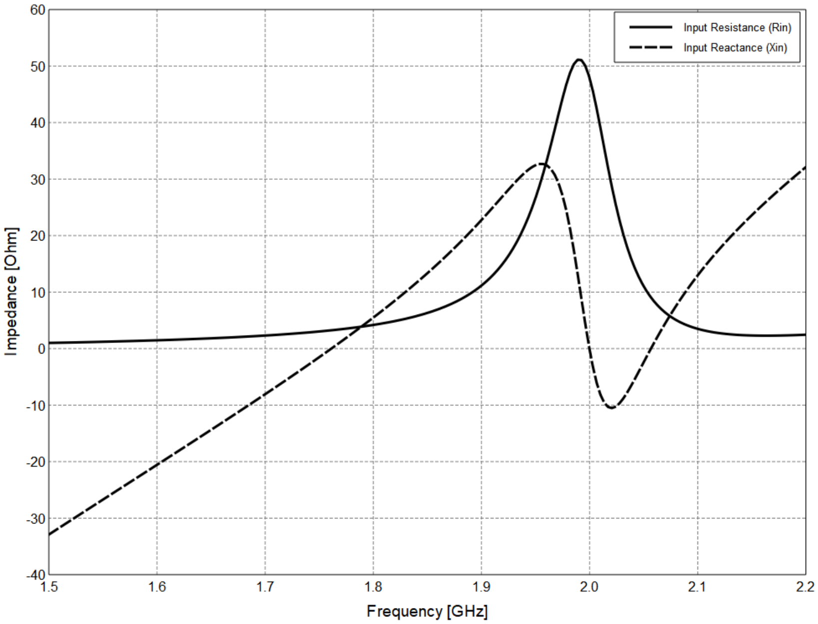

Fig.4.2-7 : Computed input impedance of the shaped antenna.

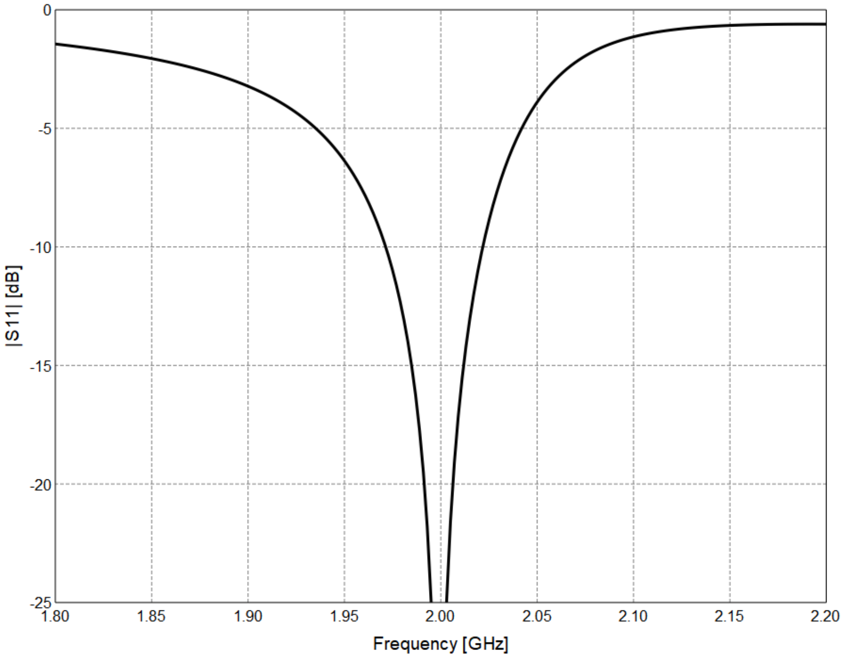

Fig.4.2-8 : Computed input reflection coefficient of the shaped-synthesized antenna for reference impedance $Z_o = 50\,\Omega$.

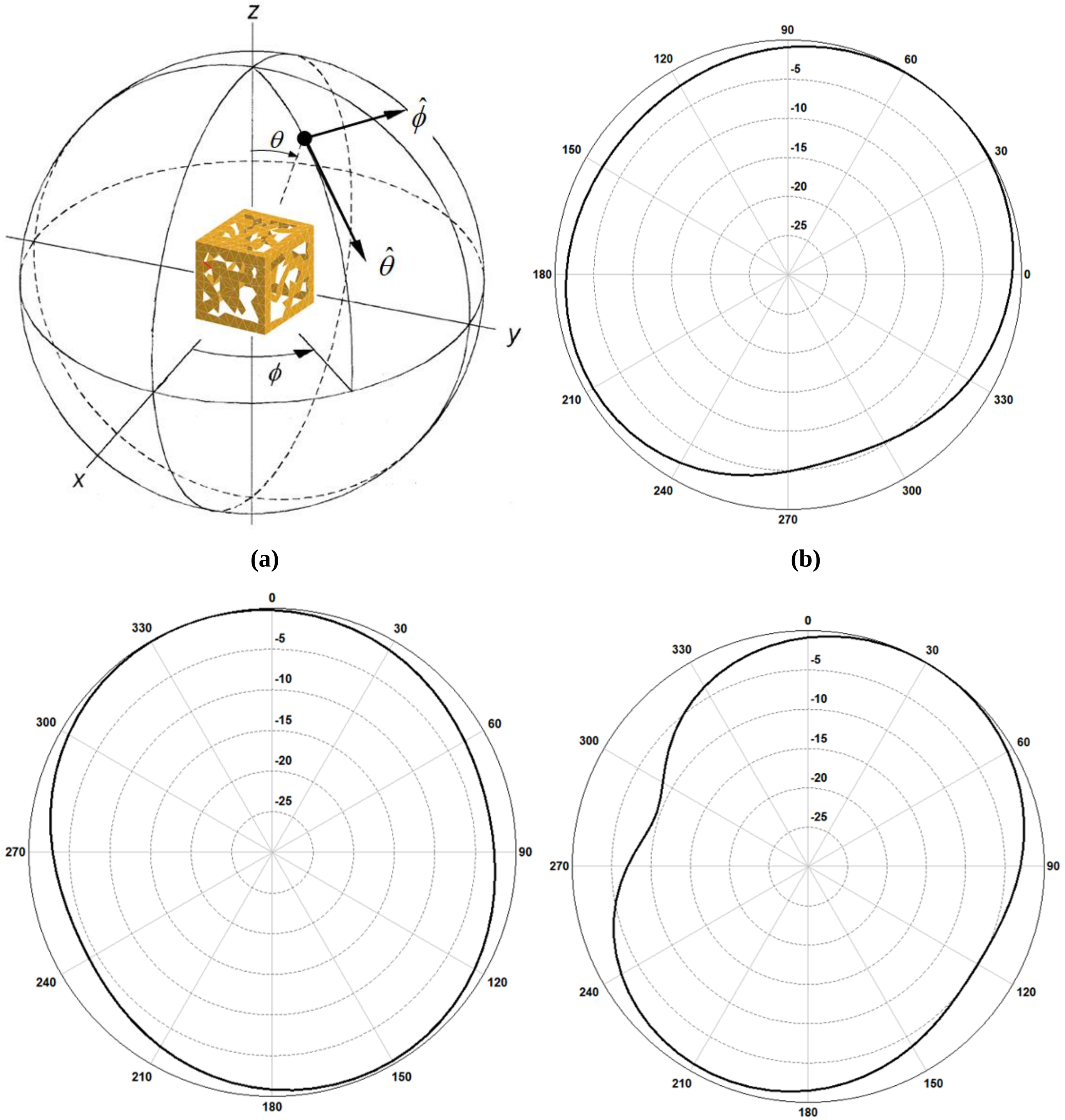

(a) **(b)**

(c) **(d)**

Fig.4.2-9 : Normalized radiation pattern cuts at f_o . The coordinate system sketch in (a) shows which pattern cuts are referred to. The pattern cuts are as follows - (b). $\theta = 90^\circ, 0^\circ \le \phi \le 360^\circ$ (c). $\phi = 0^\circ, 0^\circ \le \theta \le 360^\circ$, (d). $\phi = 90^\circ, 0^\circ \le \theta \le 360^\circ$

4.2.6 Scaling, Fabrication and Measurement

In an effort to facilitate fabrication, we increased all linear dimensions of the shape-synthesized antenna by a factor of two, and hence the behaviour of all performance measures will decrease in frequency by the same factor[100]. In other words, the centre-frequency of the scaled antenna will be 1 GHz. Just for confirmation, the computed input impedance is shown in Fig.4.2-10 and is seen to have the same behaviour as that shown in Fig.4.2-7 scaled down in frequency to be centered around 1 GHz. In the remainder of the present Section 4.2, when we refer to computed values, *it is the scaled antenna to which we are referring*.

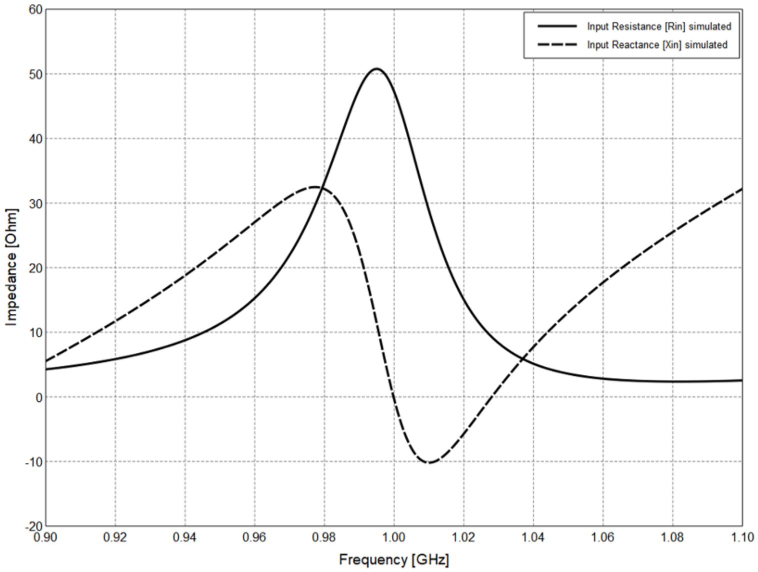

Fig. 4.2-10 : Computed input resistance and reactance of the *scaled* antenna.

The flat-patterned shape of the antenna, as shown in Fig.4.2-11, was laser-cut out of a sheet of C110 copper of thickness 0.45mm. This copper has a nominal conductivity of 5.8782×10^{7} S/m. The flat-patterned shape was then folded to form the open cuboid shape, and the corners soldered, as shown in Fig.4.2-12.

A coaxial cable was run across the one side of the cuboid antenna, as shown in the schematic diagram in Fig.4.2-13. The cable follows a current path on the cuboid shape; the outer conductor of the coaxial cable is soldered to the cuboid all the way to one side of the feedpoint gap; the centre conductor of the coaxial cable then jumps the gap and is soldered to the other side of the gap. This approximates an infinite balun. In practice antennas of this type that are used with a sensor package would be fed directly from the enclosed electronics. The coaxial feed arrangement is simply used here to permit experimental work.

---

[100] Basically, if the dimensions are scaled by a factor x, the ‘frequencies’ are shifted by (x^{-1}). This is expected from the theorem of similitude [SINC 48] [POPO 81].

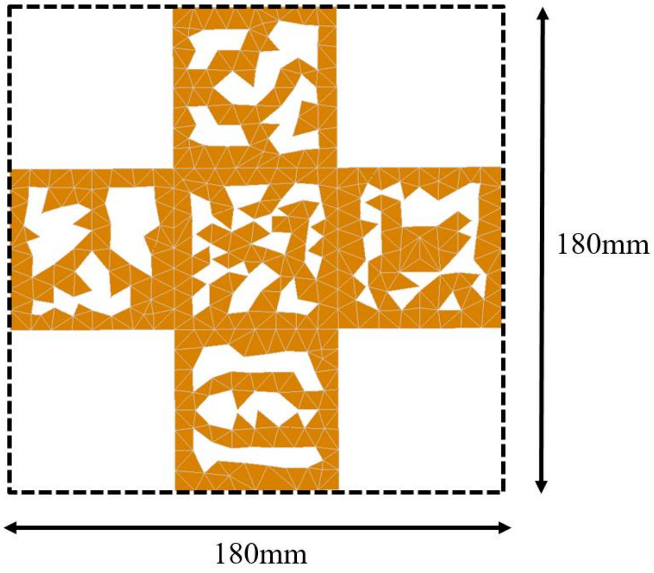

Fig. 4.2-11 : Flat-patterned antenna shape scaled by a factor of two for fabrication purposes.

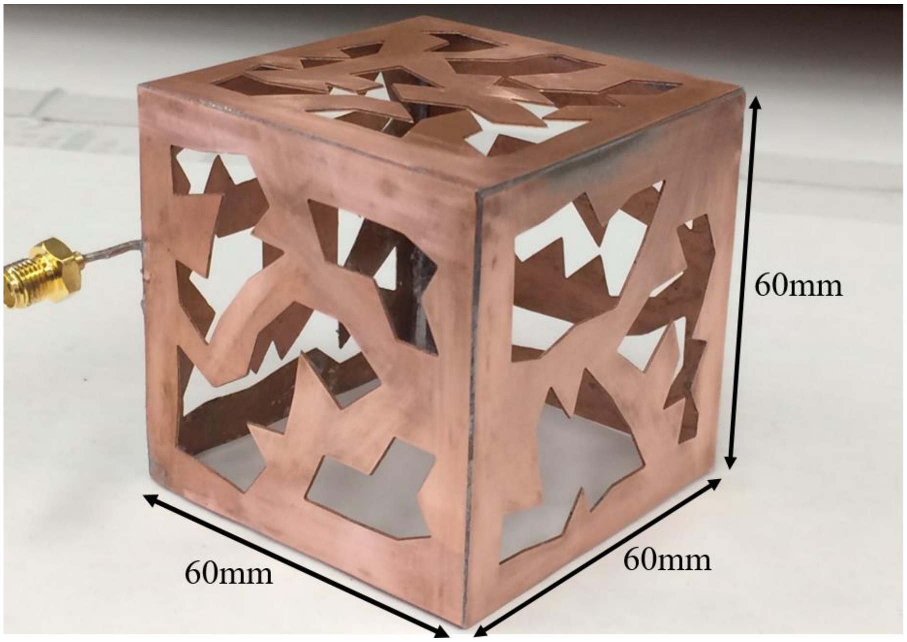

Fig. 4.2-12 : Fabricated scaled antenna.

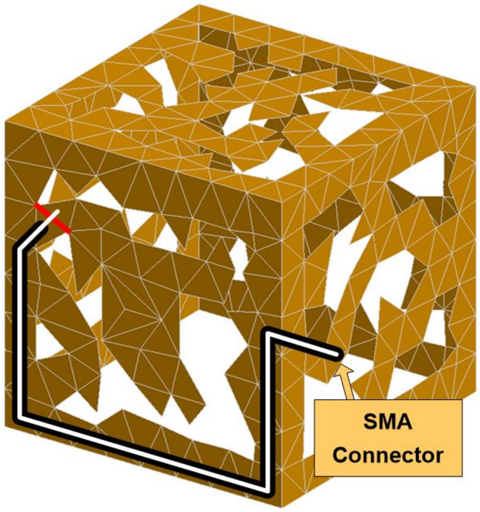

Fig.4.2-13 : Schematic illustration of the coaxial cable feedline location. The red line represents a small gap (first depicted in Fig.4.2-4), the black line the coaxial cable outer conductor, and the white line the latter's inner conductor.

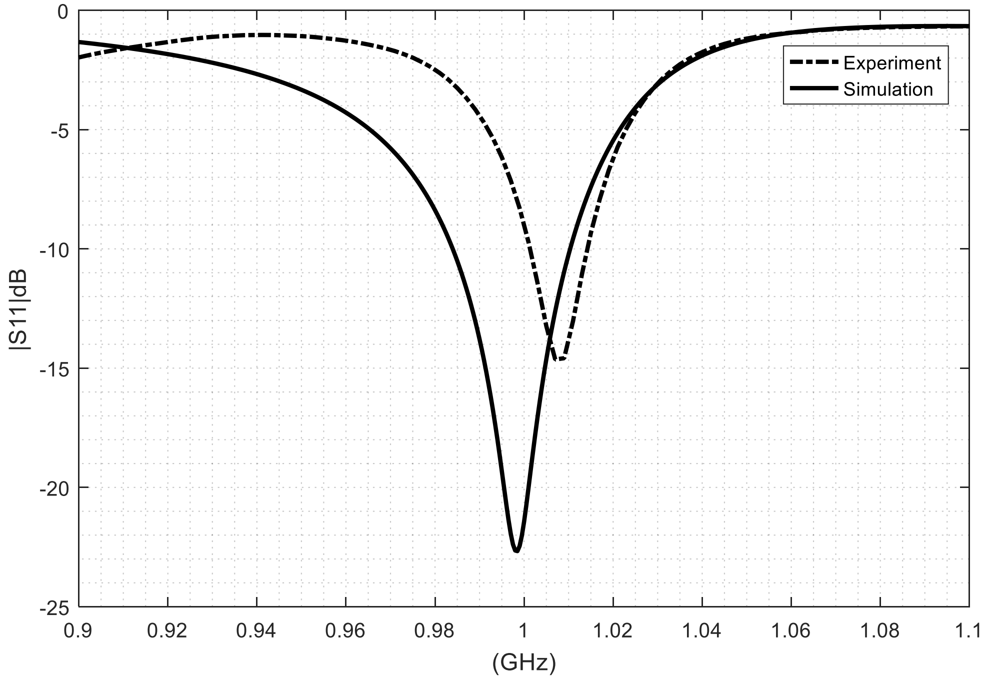

Fig.4.2-14 : Plot of the computed and measured reflection coefficient of 3-D shape electrically small antenna for a 50Ω reference impedance.

The measured $|\Gamma_{\text{in}}(f)|$ performance is compared to that computed in Fig.4.2-14. It is immediately clear that the centre-frequency (as defined by the best reflection coefficient performance) of the fabricated antenna is shifted *up* (by 0.8%) with respect to the computed one. Other parameters for the antenna are summarized in Table 4.2-1, to which we now refer. The measured self-resonance frequency is 995 MHz instead of the desired 1GHz, which represents a shift *down* (0.5%) in frequency from that computed. Using as a reference impedance the actual computed $R_{\text{in}} = 47.3\Omega$ instead of 50Ω moves the centre-frequencies slightly closer, but does not make them coincident. There are many different features on this shaped antenna. We have measured a set of randomly selected features, and calculated the difference between their values on the computed and fabricated shape. The fabricated shape dimensions differ on average by 2.3% from those of the computed shape. Thus we might expect the self-resonant frequency of the fabricated antenna (measured as 995 MHz) to be the just-mentioned percentage lower than the computed value (1000 MHz); it is in fact only 0.5% lower. Although it has been difficult to quantify, we conjecture that these shifts have been caused by the frequency-behaviour of the feeding network on the fabricated antenna, a fact supported by the observation (in Table 4.2-1) that the measured R_{in} at self-resonance is in fact 61Ω and not 47.3Ω. The value of Q_z found using (2.2-54) from computed and measured data are also shown in Table 4.2-1. The bandwidth (for a -9.54dB reflection coefficient) obtained using the Q_z in expression (2.2-55), and that using the $|\Gamma_{\text{in}}(f)|$ plot are in agreement when computed quiantities are concerned. However, there is a significant difference between the bandwidth gleaned directly from the $|\Gamma_{\text{in}}(f)|$ plot and (2.2-55) when the measured data is used.

Next we turn to the simulated radiation efficiency. We have considered that the antenna is constructed from copper, with the resulting radiation efficiency computed to be $\eta_{\text{rad}} = 98.94\%$. This is clearly an over-optimistic value[101], and confirms the known fact that it is difficult to accurately predict η_{rad}. Although the goal in this research is the establishment of the shape synthesis tool and a demonstration of its use to obtain self-resonant antennas that conform to some specified 3D surface, we nevertheless wished to obtain a more realistic estimate of η_{rad}. This has been done using the argument and results described in Appendix A. It results in a more realistic (if pessimistic) estimate of $\eta_{\text{rad}} \approx 65\%$.

---

[101] If the CEM engine's capabilities of computing η_{rad} were to improve this would automatically become part of the shaping manager. This supports the argument that a commercially available CEM engine be used as an existing resource in the shaping manager.

Finally, the computed normalized radiation pattern in the azimuth plane shown in Fig.4.2-9(b) is compared to the measured pattern in Fig.4.2-15. The decrease in the pattern level in the vicinity of the $\phi = 180^\circ$ direction is attributed to the location of the coaxial cable of the antenna test chamber equipment (emerging from the pedestal holding the antenna-under-test, and connecting to the latter there).

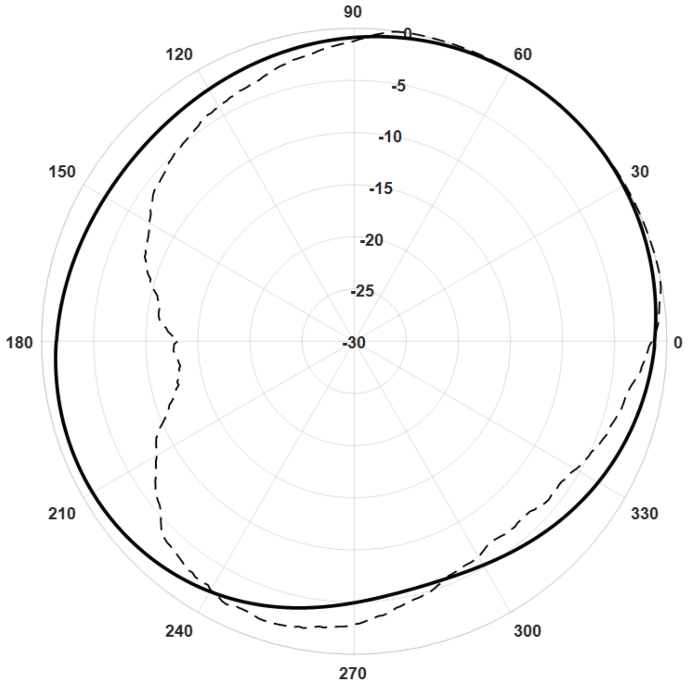

Fig.4.2-15 : Polar plot of the computed and measured normalized patterns in the azimuth plane.

Table 4.2-1 : Summary of some performance measures of the shaped open cuboid antenna

Quantity	**Intended Value**	**Computed Value**	**Measured Value**
Frequency of Minimum $\lvert\Gamma_{\text{in}}(f)\rvert$	-	998.5 MHz	1007 MHz
Minimum $\lvert\Gamma_{\text{in}}(f)\rvert$	-	-22.7 dB	-14.7 dB
Bandwidth (-9.54dB) extracted from $\lvert\Gamma_{\text{in}}(f)\rvert$ plot	-	2.8%	1.6%
Self-Resonance Frequency ($X_{\text{in}} \approx 0$)	1000 MHz	1000 MHz	995 MHz
R_{in} at Self-Resonance Frequency	-	47.3Ω	61Ω
Q_z	-	25.82	19.44
Bandwidth (-9.54dB) from Q_z at f_o	-	2.8%	3.7%

4.2.7 Shaping of a Closed Cuboid of the Same Size

It is of interest to briefly consider the difference in the outcome of the shape synthesis if the starting shape is a cuboid of the same size as that just discussed, but is closed (that is, has its bottom face present) as shown in Fig.4.2-16(a). The centre frequency is 2 GHz, and up/down geometrical symmetry is enforced. Fig.4.2-17 shows that the shaping procedure takes 150 generations. The shaped geometry is that in Fig.4.2-16(b), which also shows the feedpoint (located after shaping has been completed) denoted by the red line. The computed $Z_{\mathrm{in}}(f)$ and $|\Gamma_{\mathrm{in}}(f)|$ are shown in Fig.4.2-18, and is the principal point of interest here. Although an anti-resonance behaviour occurs at a much lower frequency (and we could use this, with $ka = 1$ at 1.85 GHz), with the additional conductor available (the bottom face) the shaping procedure has selected the second "ordinary-resonance" where the variation of the real and imaginary parts of $Z_{\mathrm{in}}(f)$ are more gradual with respect to frequency. Indeed, at the self-resonance frequency (2 GHz) we have $Q_z = 10.62$, which is less than half the computed value (in Table 4.2-1) when the open cuboid starting shape was used. This predicts a -9.54dB bandwidth of 6.7%.

We observe that the open cuboid $Z_{\mathrm{in}}(f)$ result in Fig.4.2-7 differs in character (not just values) from that of the present closed cuboid in Fig.4.2-18(b). Dipole-like antennas have a first anti-resonance at a frequency higher than that at which its ordinary resonance occurs, whereas the opposite is true for loop-like antennas. It would appear that the different current paths that emerge from the shaping procedure thus also determine which kind of input impedance behaviour will result, depending on the starting shape and hence the associated conducting material available to it.

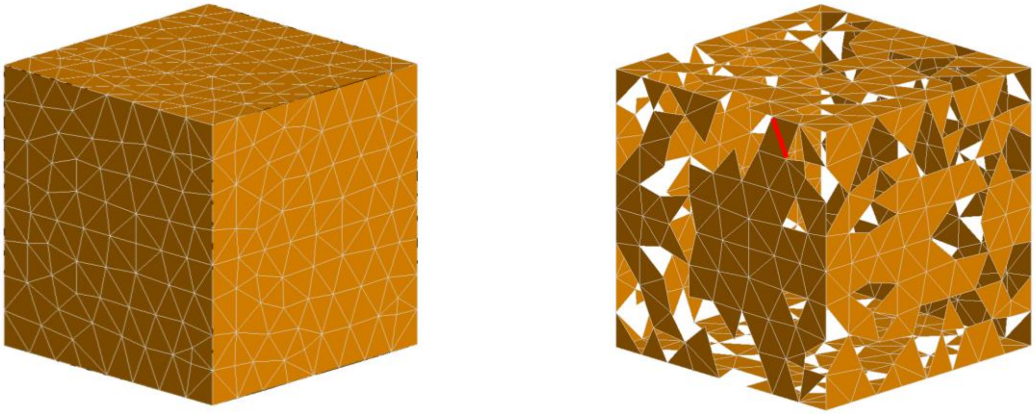
(a) (b)

Fig.4.2-16 : (a). The starting shape of the closed cuboid, and (b). the resulting shape synthesized antenna. Islands and vertex-only connections have not yet been removed in (b).

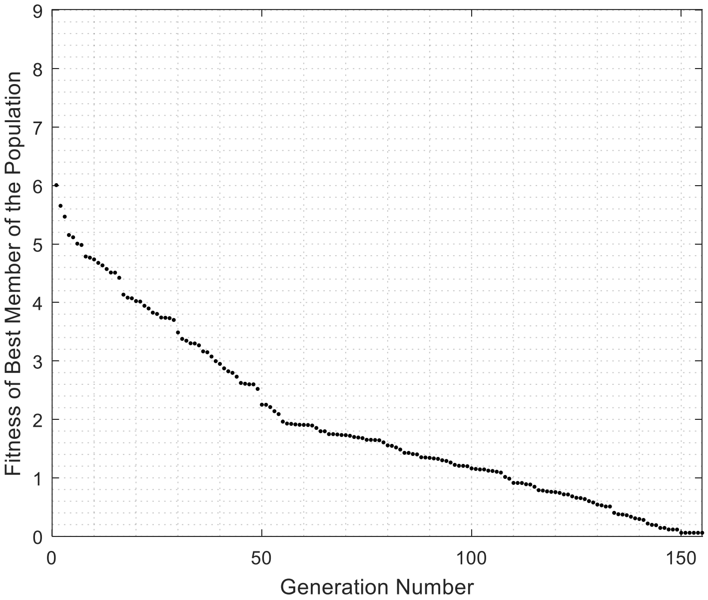

Fig.4.2-17 : The objective function value of the fittest shape in each generation, versus the generation number.

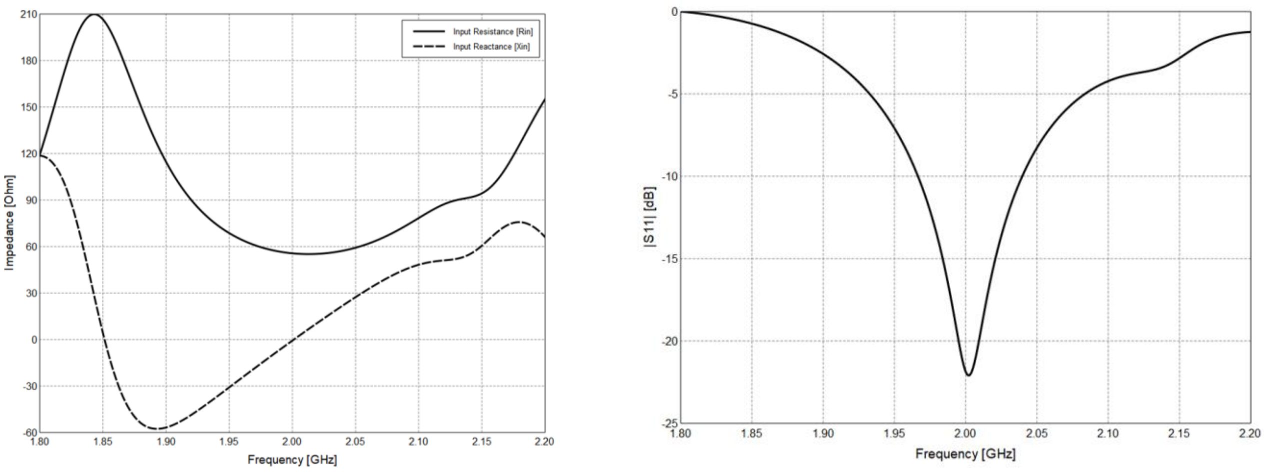

(a) **(b)**

Fig.4.2-18 : (a). Computed input impedance of the antenna shape-synthesized from the closed cuboid starting shape and (b). its computed input reflection coefficient for reference impedance $Z_o = 50\Omega$.

4.2.8 Shaping of a Closed Conducting Sphere

The conducting sphere has been of interest for a long time, and its analysis harks back to a time when it was the only finite-sized PEC object that could be treated in a rigorous analytical way [HARR 61], and so as much information on electromagnetic scattering was gleaned from it in order to understand scattering in general. Also, the so-called spherical wave modes used in deriving various forms of the Q-bounds mentioned in Section 2.2.10 are in fact the characteristic modes of a PEC sphere of the same radius as the minimum sphere [LI 2019]. The spherical dipole antenna has also retained the interest of many [BEST 05]. But of course these are restricted to a spherical surface. We very briefly consider the spherical starting shape on the left in Fig.4.2-19, essentially only to dispel any concerns that the shaping tool needs starting shapes to be rectangular in form. They can literally be anything. The geometry here is such that the radius of the minimum sphere is obviously that of the actual starting shape itself, and in this case $ka = 0.4189$ for a 10mm radius sphere at 2 GHz. The starting shape was densely meshed into $N_\Delta = 856$ triangles, which resulted in an initial $N_{\text{dof}} = 1284$. The objective function was again $F_{obj} = |\lambda_1(f_o)|$. The resulting shape is that on the right in Fig.4.2-19, obtained in roughly 450 generations of the shape synthesis process. The computed $Q_Z = 53.88$, and so (2.2-55) predicts a -9.54dB bandwidth of 1.3%.

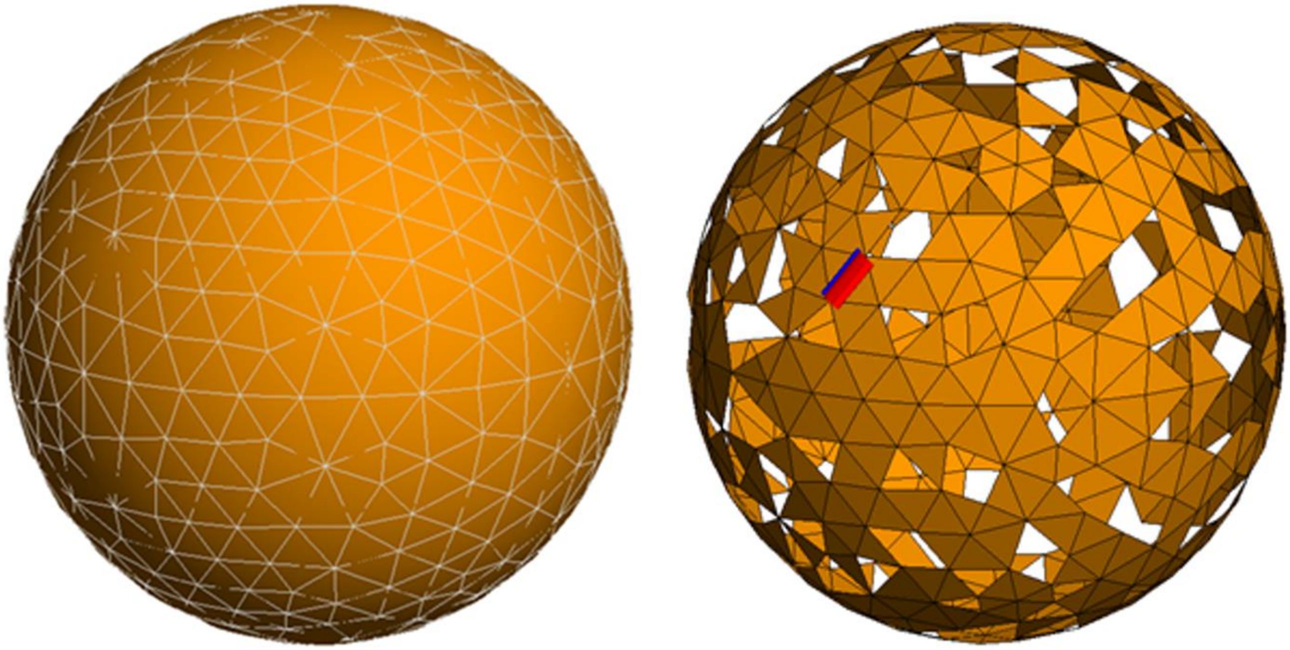

Fig.4.2-19 : The starting shape of the 10mm radius closed sphere is shown on the left, and the shaped antenna on the right (along with its feed location).

4.3 THREE-DIMENSIONAL SHAPE SYNTHESIS EXAMPLE #2 : PRINTED ELECTRONICS COMPATIBLE ANTENNA

4.3.1 Preamble

Although printed electronics can be done over 3D surfaces, indications are that cost considerations likely encourage the use of such printing on a flat surface that is then folded. In such cases the desire is to simply fold and bond the printed shape onto the package without any need for any sort of conductive bonding (or soldering) at the edges.

4.3.2 Starting Geometry & Objective Function

The starting shape is the non-planar cuboid-like structure shown in Fig.4.3-1(a), with $d = 10\,\text{mm}$, $\text{w} = h = 6\,\text{mm}$ and $s = 2\,\text{mm}$. The corners are purposefully missing so that the resulting shape satisfies the assembly requirements noted in Section 4.3.1. The centre frequency $f_o = 3$ GHz, at which the wavelength $\lambda = 100\,\text{mm}$, and so $d = \lambda/10$. Use of some elementary analytical geometry shows that the radius of the minimum sphere is $a = \sqrt{h^2 + 2d^2}\,/\,2$, and so in this case $a/\lambda = 0.0768$ and hence $ka = 0.4826$. The starting shape is meshed into $N_\Delta = 644$ triangles, resulting in an initial $N_{dof} = 922$. The objective function is the same as that in expression (4.2-1).

Although we do not do so here, the shape synthesis procedure and tool can deal with any starting shape. For example, if it is determined that quick assembly (folding) of such an antenna would result in a “cubical” shape with some rounding of the edges, as depicted in Fig.4.2-1(b), the starting shape could be specified to accommodate this.

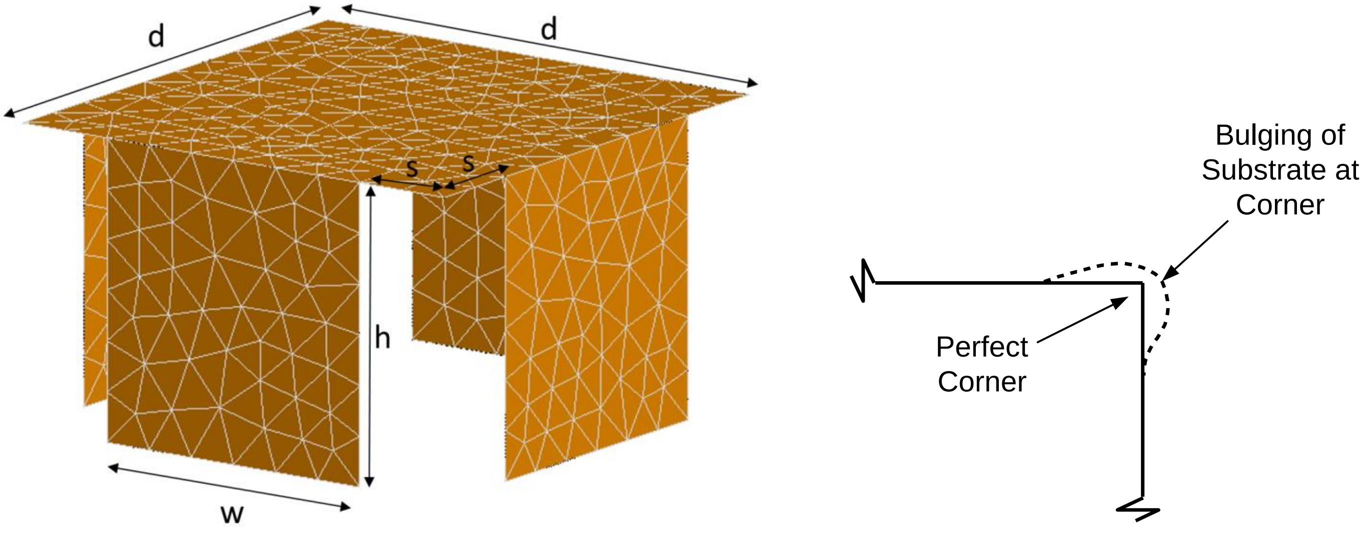

(a) **(b)**

Fig.4.3-1: (a).Cuboid-like starting shape with purposefully missing corners, used in this example, and (b).Possible alternative shape that compensates for assembly ‘imperfections’. Note that $\text{w} + 2s = d$.

4.3.3 Outcome of the Shape Synthesis Process

The shaped antenna geometry is that on the left in Fig.4.3-2. This shape, which with $ka = 0.4826$ is electrically much smaller than that in Section 4.2, was achieved 5000 generations, and resulted in $F_{obj} = |\lambda_1(f_o)| = 0.034.$ It is clear from Fig.4.3-3 that the eigenvalues of the higher-order CMs are much larger than that of the lowest order one. The feedpoint location was found to be as shown on the right in Fig.4.3-2. In Fig.4.3-5 the first three eigenvalues of the shaped structure are plotted versus frequency, confirming that λ_1 indeed goes through zero at 3 GHz. We will make further use of this information in Section 4.3.4.

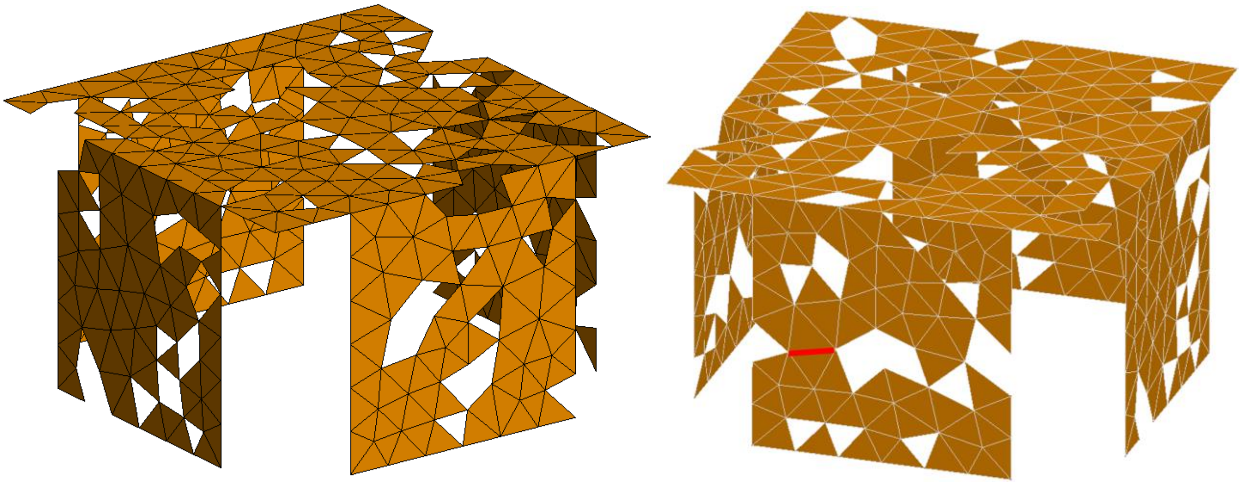

Fig.4.3-2 : Two different views of the geometry of the shaped antenna. The left view shows the feed location as a red line.

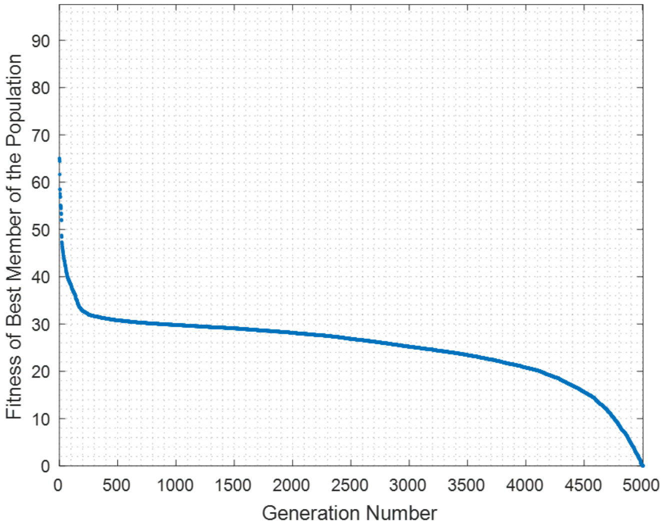

Fig.4.3-3 : The cost function of the fittest member in each generation of shapes versus the generation number.

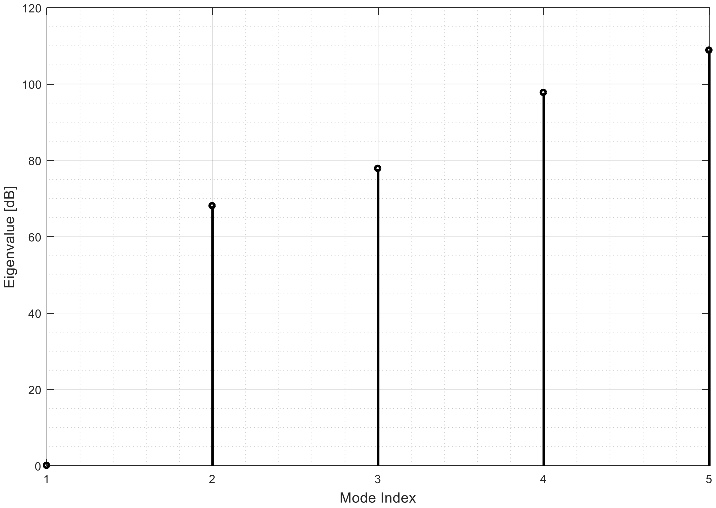

Fig.4.3-4 : Eigenvalues $|\lambda_n|$ vs mode index *n* for the final shaped antenna at f_o, normalised to $|\lambda_1|$ and expressed in deciBels.

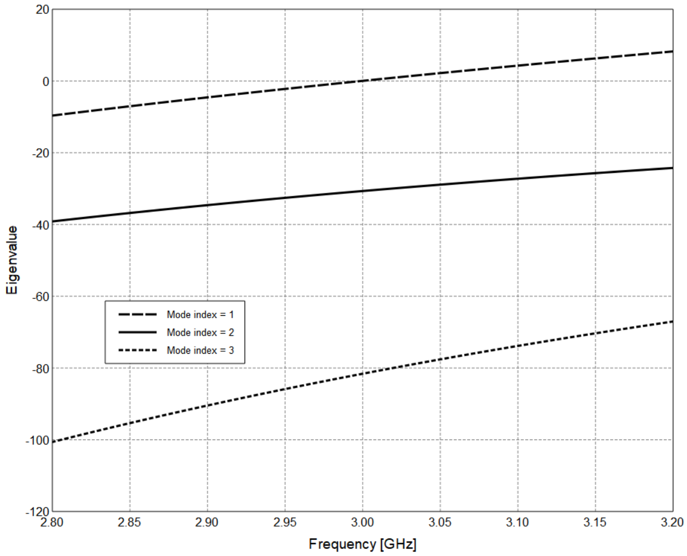

Fig.4.3-5 : Eigenvalues of the first three characteristic modes versus frequency.

4.3.4 Computed Performance of the Shaped Antenna

With a feed located at the location on the shaped antenna as shown in Fig.4.3-2, a driven analysis provides its performance measures in Fig.4.3-6 through Fig.4.3-8, as well as Table 4.3-1. Some comments are in order. Firsly, we note from Fig.4/3-7 that the modal excitation coefficient of the lowest CM are more than 70dB more than that of the higher order CMs. This is truly a single-mode antenna. More so than the open cuboid case for which a corresponding result is that in Fig.4.2-6. The reason is that the open cuboid had ka roughly double that of the present antenna. Fig.4.3-8 shows the input impedance character is that of utilizing an ordinary resonance at the desired f_o, this occuring at a frequency lower than that at which the first anti-resonance occurs. Table 4.3-1 shows that the -9.54dB bandwidths predicted from $|\Gamma_{\mathrm{in}}(f)|$ and from Q_{z} are much the same. Also shown is the the quality factor Q_{cm} predicted from the slope of the curve $\lambda_1(f)$ in Fig.4.3-5, at f_o, via expression (2.2-53). The value of Q_{cm} (predictable from the eigeanalysis of the shaped antenna before ever specifying the feed location), and Q_{z} (predictable from $Z_{in}(f)$ and a driven analysis once the feed has been specified), are almost identical for such a single-mode antenna. It is not necessary to use Q_{cm}, but showing its equivalence to Q_{z} anchors the shaping procedure being used here in the firmly in the characteristic mode framework. Finally, the computed total gain patterns

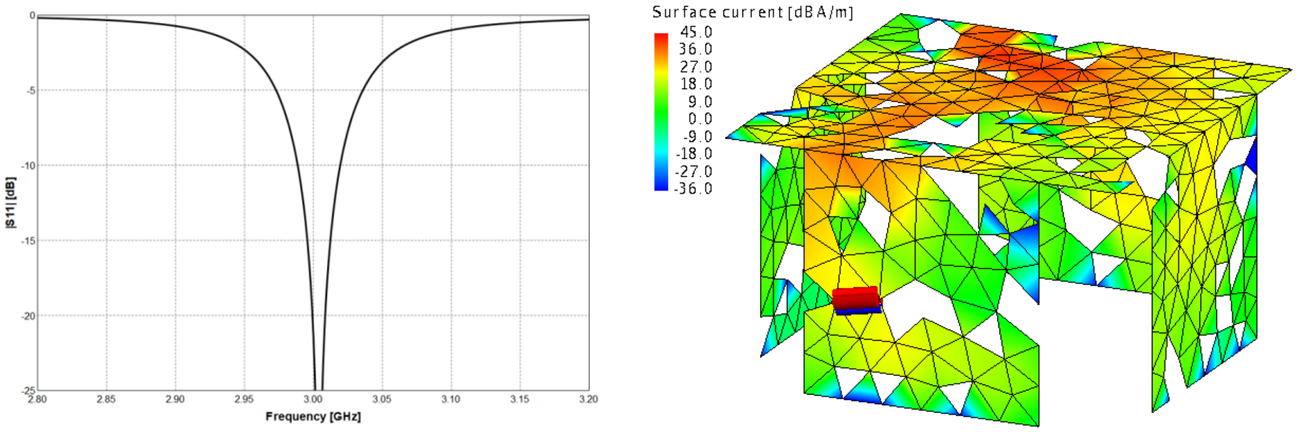

(a) **(b)**

Fig.4.3-6 : (a). Computed $|\Gamma_{\text{in}}(f)|$ of the shaped antenna for a reference impedance $Z_{\text{o}} = 50\,\Omega$, and (b). the associated current distribution on the fed antenna at 3 GHz.

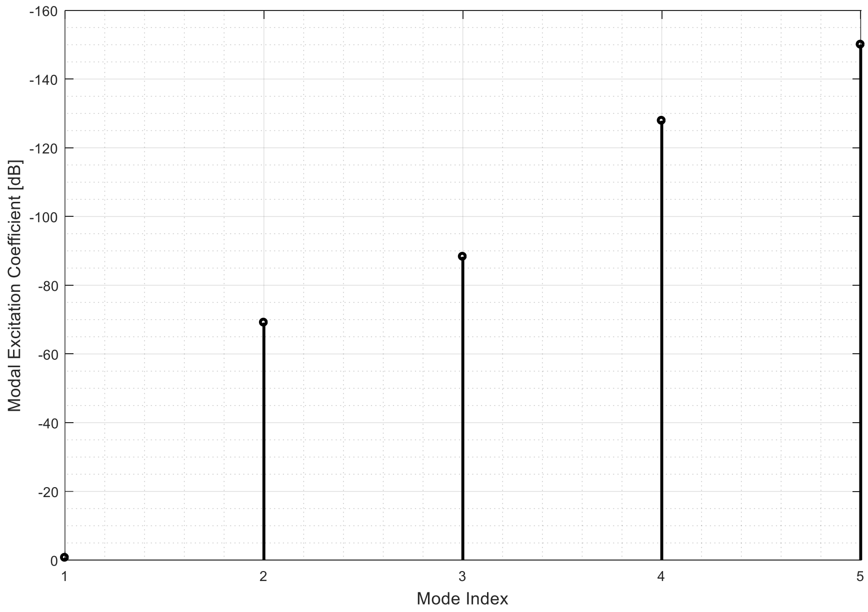

Fig.4.3-7 : Modal excitation coefficient $|\alpha_n|$ versus modal index *n*, at 3 GHz.

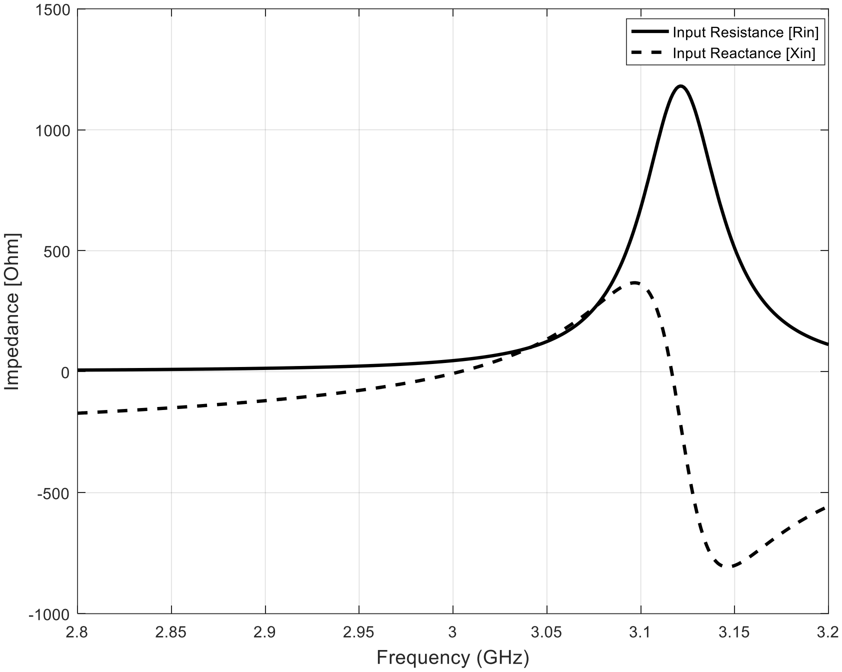

Fig.4.3-8 : Computed input resistance and reactance of the shape-synthesized antenna.

Table 4.3-1 : Summary of some performance measures of the shaped printed electronics compatible shaped antenna

Quantity	**Intended Value**	**Computed Value**
Frequency of Minimum $\left\|\Gamma_{\text{in}}(f)\right\|$	-	3.0002 GHz
Self-Resonance Frequency ($X_{\text{in}} \approx 0$)	3.0 GHz	3.0002 GHz
R_{in} at Self-Resonance Frequency	-	46 Ω
Maximum Gain at 3 GHz	-	1.47 dBi
Q_{cm} at 3 GHz	-	60
Q_z at 3 GHz	-	59
η_{rad} at 3 GHz	-	89%
Bandwidth (-9.54dB) extracted from $\left\|\Gamma_{\text{in}}(f)\right\|$ plot	-	1.10 %
Bandwidth (-9.54dB) from Q_z	-	1.20 %

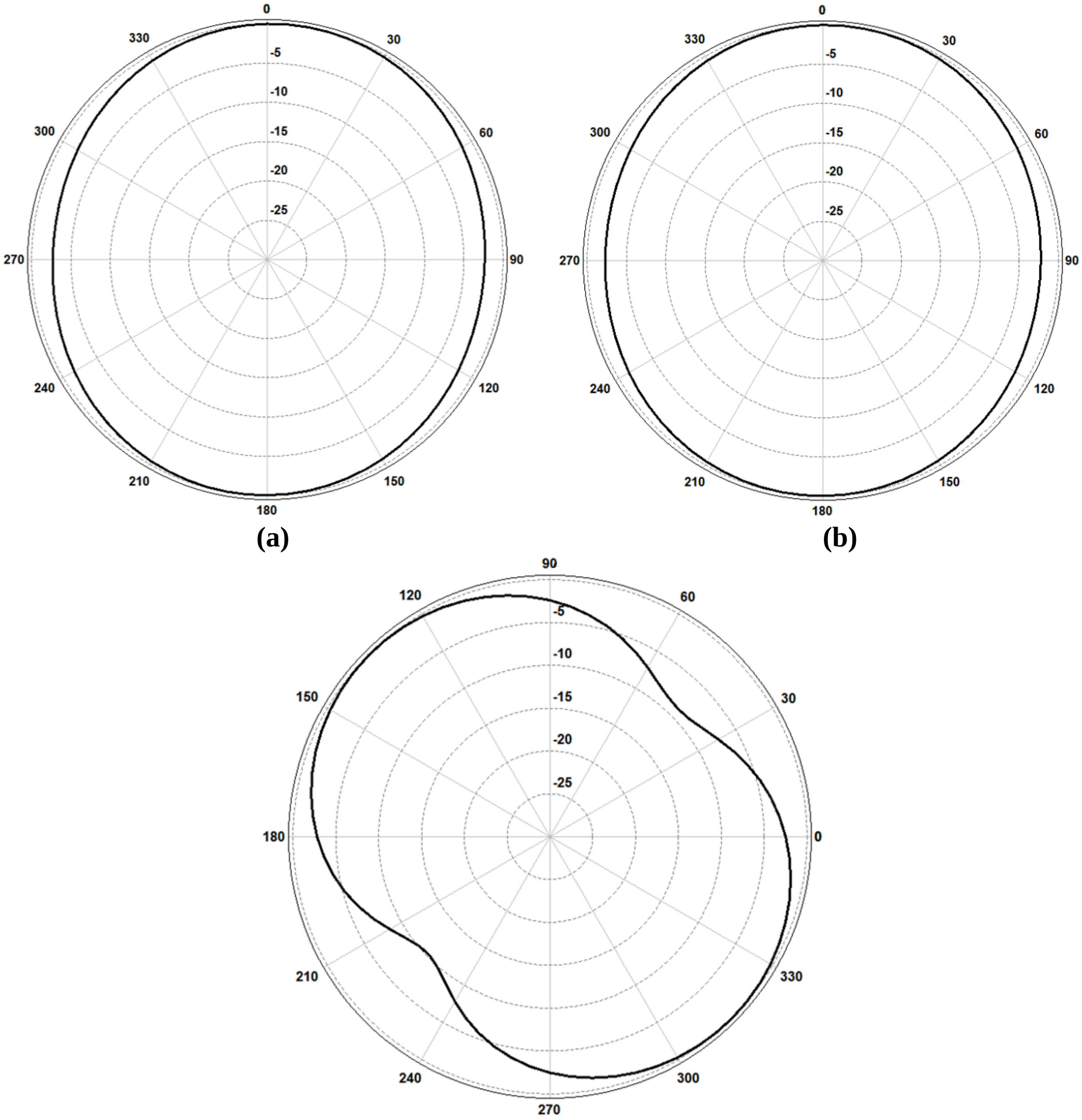

(a)

(b)

(c)

Fig.4.3-9 : Computed normalized radiation pattern cuts at f_o . The elevation plane cuts are (a). $\phi = 0^\circ, 0^\circ \le \theta \le 360^\circ$ and (b). $\phi = 90^\circ, 0^\circ \le \theta \le 360^\circ$. The azimuth pattern cut $\theta = 90^\circ, 0^\circ \le \phi \le 360^\circ$ is shown in (c).

4.4 THREE-DIMENSIONAL SHAPE SYNTHESIS EXAMPLE #3 : CUBOID WITH BATTERY INSIDE

4.4.1 Starting Geometry

It was noted in Section 4.1.2 that sensor packages often have batteries within them. In this demonstration of the shaping procedure that has been developed in this thesis we consider the starting shape to be the open cuboid with one face removed, and a closed smaller cuboid inside it, as depicted in Fig.4.4-1. The inner closed cuboid represents a battery, and it is constrained from participating in the shaping. The outer open cuboid is that to be shaped. The starting shape dimensions are $d = 13\,\text{mm}$, $h = 10\,\text{mm}$ and $s = 6.5\,\text{mm}$.

The centre frequency is $f_o = 2GHz$, at which the wavelength $\lambda = 150\,\text{mm}$, and so the sides of the outer cuboid are each of electrical dimension $d = 0.0867\lambda$ ($d \approx \lambda/11.5$). The radius a of the minimum sphere is then $a = (\sqrt{3}/2)\,d = 0.0751\lambda$, and hence $ka = 0.4716$. The starting shape is a densely meshed into $N_{\Delta} = 822$ triangles, which results in an initial $N_{\text{dof}} = 1219$. The objective function is that in expression (4.2-1).

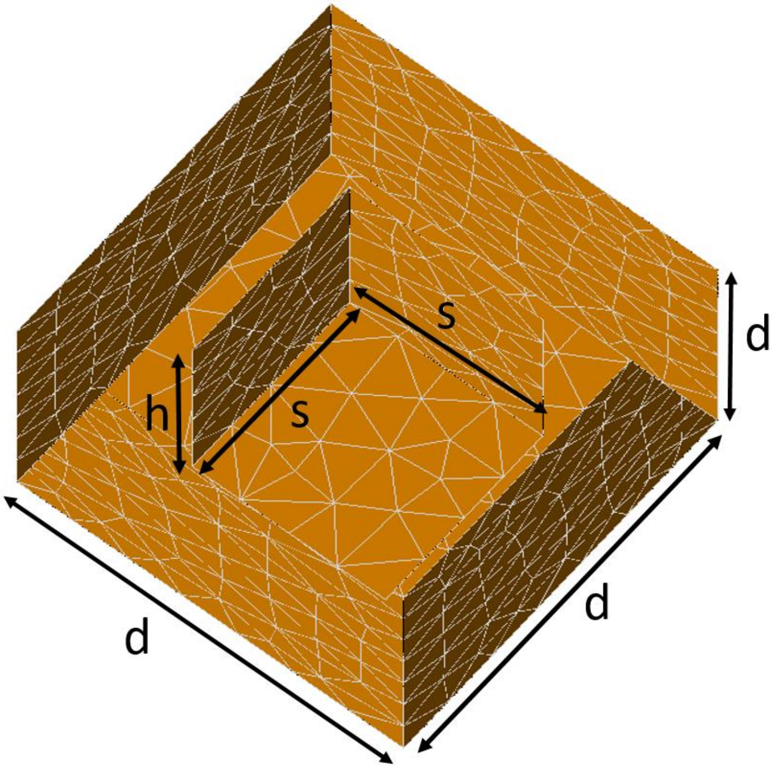

Fig.4.4-1: Starting shape consisting of an outer open cuboid with an inner closed cuboid.

4.4.2 Outcome of the Shape Synthesis Process

The shaping process reduced $F_{obj} = |\lambda_1(f_o)|$ to a value 0.0028 within several thousand generations, resulting in the shape shown to the left in Fig.4.4-2.

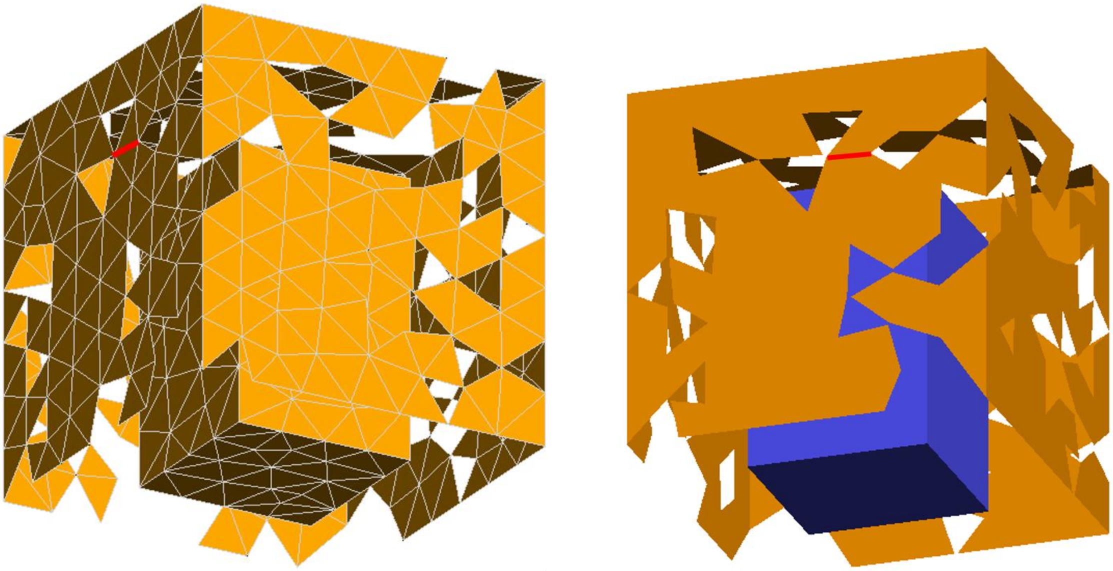

Fig.4.4-2 : The shape synthesized antenna is shown to the left, with the feedpoint identified in red. The same geometry is shown to the right, with the MM mesh removed and the (unshaped) battery shown in blue.

4.4.3 Computed Performance of the Shaped Antenna

As for most electrically small antennas the curve is $|\Gamma_{\text{in}}(f)|$ similar to that in Fig.4.3-6(b), with reflection coefficient $|\Gamma_{\text{in}}| < -30\,\text{dB}$ at (in this case) 2 GHz, referenced to 50Ω. The modal weighting coefficients in Fig.4.4-3 once again reveal this $ka = 0.4716$ shape synthesized antenna to be a perfectly single-mode one. It has achieved self-resonance in the presence of the inner cuboid (battery) by accounting for the presence of, and indeed exploiting, the latter object during shaping, as confirmed by the fact (not unexpected) that Fig.4.4-4 shows a significant induced current density on the battery. The input impedance character in Fig.4.4-5 reveals that the shaping process has utilized the first anti-resonance of the structure, there being no ordinary resonance lower in frequency where $R_{in} \neq 0$. The total gain patterns are given in Fig.4.4-6 and, like most electrically small antennas, these are broad (some even call such patterns “close to isotropic”). The performance is summarized in Table 4.4-1; this information will be used along with that in the earlier tables for comparison purposes in Fig.4.7-1. Although we mentioned earlier that (and this is not unusual) the computed η_{rad} values are optimistic, we note the trend that as we go to an antenna with a smaller ka value the predicted η_{rad} values decrease. This follows the trend, at least, found and expected by antenna researchers in practice.

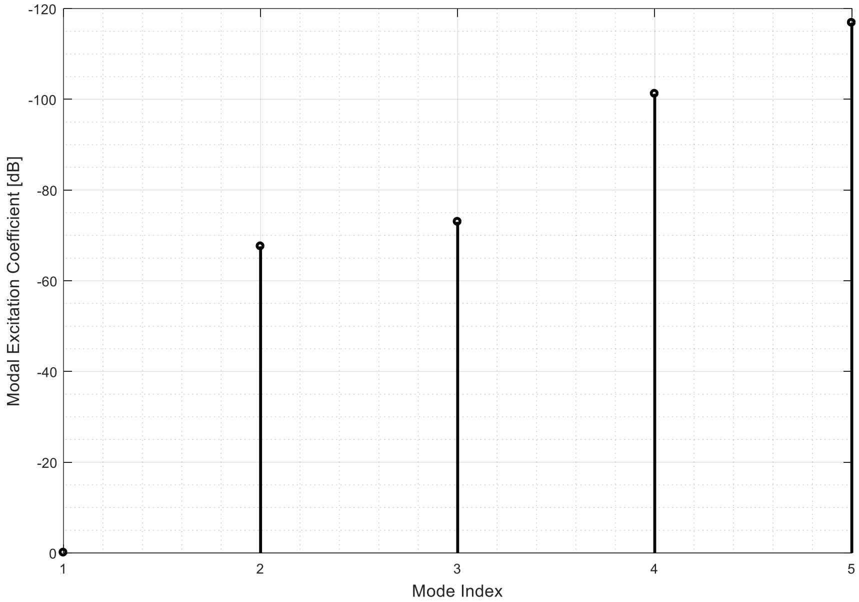

Fig.4.4-3 : Modal excitation coefficient $|\alpha_n|$ versus modal index n, at 2 GHz.

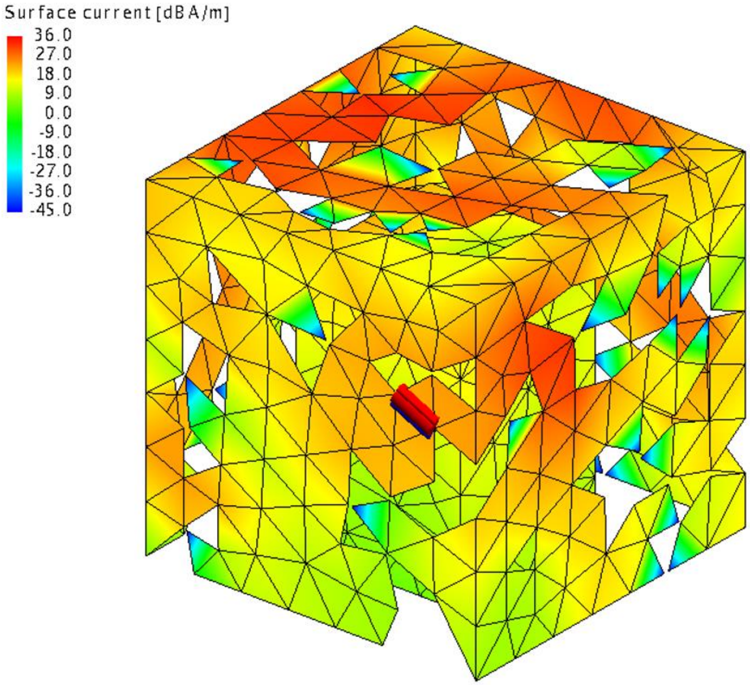

Fig.4.4-4 : Current distribution on the driven shaped structure at 2 GHz.

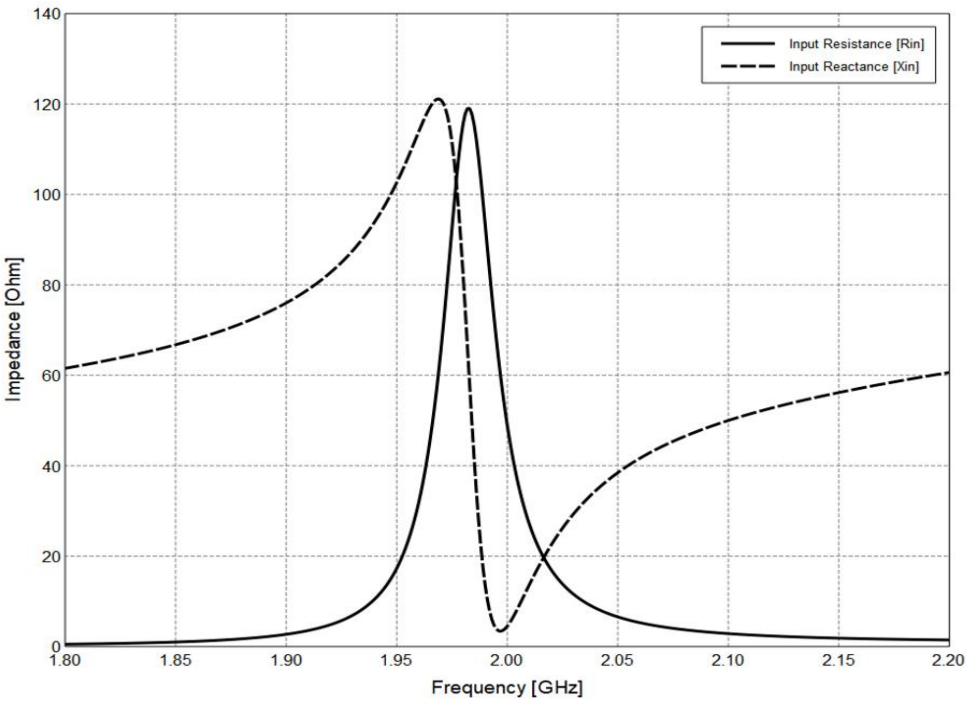

Fig.4.4-5 : Computed input impedance of the shaped-synthesized antenna.

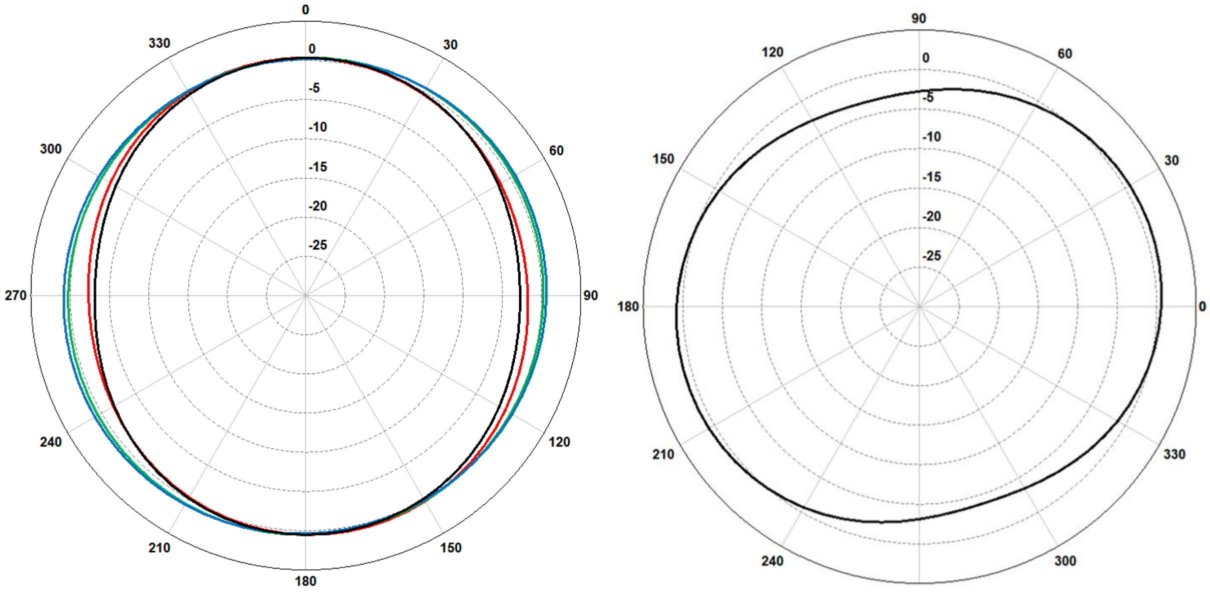

(a)

(b)

Fig.4.4-6 : Computed total gain patterns (in dBi). The elevation plane cuts shown in (a) are for $\phi = 0^\circ$, $\phi = 45^\circ$, $\phi = 90^\circ$ and $\phi = 135^\circ$. The azimuth pattern cut is that in (b).

Table 4.4-1 : Summary of some performance measures of the shaped antenna with a "battery" enclosed

Quantity	**Intended Value**	**Computed Value**
Frequency of Minimum $\left\|\Gamma_{\text{in}}(f)\right\|$	-	1.9972 GHz
Minimum $\left\|\Gamma_{\text{in}}(f)\right\|$	-	< -30 dB
Self-Resonance Frequency ($X_{\text{in}} \approx 0$)	2.0 GHz	1.9972 GHz
R_{in} at Self-Resonance Frequency	-	59.1 Ω
Maximum Gain at 2 GHz	-	1.13 dBi
Q_z at 2 GHz	-	66.18
η_{rad} at 2 GHz	-	92.3 %
Bandwidth (-9.54dB) extracted from $\left\|\Gamma_{\text{in}}(f)\right\|$ plot	-	1.03 %
Bandwidth (-9.54dB) from Q_z	-	1.07 %

4.5 THREE-DIMENSIONAL SHAPE SYNTHESIS EXAMPLE #4 : *OPEN CUBOID WITH PATTERN CONSTRAINTS*

4.5.1 Preamble

Until now we have used an objective function that strives simply to arrive at an antenna that is self-resonant. This is often sufficient. The electrical size of the resulting antennas is such that their radiation patterns are relatively broad almost by default. However, many sensor antennas will need to operate in the same wireless environment as mobile devices, and so the mean-effective-directivity (MED) might be an important quantity. This quantity is easily defined (and hence calculated) for a driven antenna, as explained in Section 2.2.9. However, recall that in the shaping procedure being pursued here the feed location is not known until the shaping is completed. Fortunately, we have been able to show (in Section 4.5.2) that it is possible to determine the MED for a single-mode antenna without actually knowing the feed location. Once this expression has been derived the starting shape form Section 4.3 is re-shaped with MED as an additional component of the objective function, all other specifications being the same as in Section 4.3.

4.5.2 Maximum Effective Directivity for a Single-Mode Antenna

Based on the comments in Section 2.2.9, the mean effective directivity (MED) is

$$MED = \int_0^{2\pi}\int_0^{\pi}\left\{\frac{XPR}{1+XPR}D_\theta(\theta,\phi)\mathscr{P}_\theta(\theta,\phi)+\frac{1}{1+XPR}D_\phi(\theta,\phi)\mathscr{P}_\phi(\theta,\phi)\right\}\sin\theta\, d\theta d\phi \qquad (4.5\text{-}1)$$

If an impressed source is used to drive a radiating structure whose CM fields $\bar{E}_n\left(\theta,\phi\right)$ are known, we saw in Section 2.4 that it is possible to compute the modal weighting coefficients α_n such that the far-zone radiated field is

$$\bar{E}(\theta,\phi) = \sum_{n=1}^{\infty}\alpha_n\,\bar{E}_n(\theta,\phi) = \hat{\theta}\sum_{n=1}^{\infty}\alpha_n\,E_{n\theta}(\theta,\phi)+\hat{\phi}\sum_{n=1}^{\infty}\alpha_n\,E_{n\phi}(\theta,\phi) \qquad (4.5\text{-}2)$$

The orthogonality property of the far-zone fields means that the power radiated by the driven structure is

$$P_{rad} = \sum_{n=1}^{\infty}\left|\alpha_n\right|^2 \qquad (4.5\text{-}3)$$

The partial radiation intensities are

$$U_\theta(\theta\,,\phi) = \frac{1}{2\eta_o}\left|\sum_{n=1}^{\infty}\alpha_n E_{n\theta}\left(\theta,\phi\right)\right|^2 \qquad (4.5\text{-}4)$$

and

$$U_\phi(\theta\,,\phi) = \frac{1}{2\eta_o}\left|\sum_{n=1}^{\infty}\alpha_n E_{n\phi}\left(\theta,\phi\right)\right|^2 \qquad (4.5\text{-}5)$$

The definitions in Section 2.2.7 then allow us to write the partial directivities of the antenna as

$$D_\theta(\theta\,,\phi) = \frac{4\pi\,U_\theta(\theta\,,\phi)}{P_{rad}} = \frac{2\pi}{\eta_o}\frac{\left|\sum_{n=1}^{\infty}\alpha_n E_{n\theta}\left(\theta,\phi\right)\right|^2}{\sum_{n=1}^{\infty}\left|\alpha_n\right|^2} \qquad (4.5\text{-}6)$$

and

$$D_\phi(\theta\,,\phi) = \frac{4\pi\,U_\phi(\theta\,,\phi)}{P_{rad}} = \frac{2\pi}{\eta_o}\frac{\left|\sum_{n=1}^{\infty}\alpha_n E_{n\phi}\left(\theta,\phi\right)\right|^2}{\sum_{n=1}^{\infty}\left|\alpha_n\right|^2} \qquad (4.5\text{-}7)$$

The model weighting coefficients α_n can of course not be found unless we specify how the antenna structure is excited. In other words, until we specify the feed we cannot find the partial directivities. However, if we have an electrically small single-mode antenna[102] then $|\alpha_1| >> |\alpha_m|$ for $m \geq 2$. The partial directivity expressions (4.5-4) and (4.5-5) then become

$$D_\theta(\theta\,,\phi) \approx \frac{2\pi}{\eta_o}\left|E_{1\theta}\left(\theta,\phi\right)\right|^2 \tag{4.5-8}$$

and

$$D_\phi(\theta\,,\phi) \approx \frac{2\pi}{\eta_o}\left|E_{1\phi}\left(\theta,\phi\right)\right|^2 \tag{4.5-9}$$

In other words, on the assumption that a single CM will be excited on the antenna structure, we can find the partial directivities without having to specify how this will be achieved[103]. Thus we can find the MED of each single-mode candidate during the shape optimisation process. Use of (4.5-6) and (4.5-7) in (4.5-1) gives

$$MED = \frac{2\pi}{\eta_o}\int_0^{2\pi}\int_0^{\pi}\left\{\frac{XPR}{1+XPR}\left|E_{1\theta}\left(\theta,\phi\right)\right|^2 \mathscr{P}_\theta(\theta,\phi) + \frac{1}{1+XPR}\left|E_{1\phi}\left(\theta,\phi\right)\right|^2 \mathscr{P}_\phi(\theta,\phi)\right\}\sin\theta\, d\theta d\phi \tag{4.5-10}$$

4.5.3 The Objective Function

The objective function used is now

$$F_{obj} = \left|\lambda_1(f_{\mathrm{o}})\right| + \left[1 - \frac{MED(f_{\mathrm{o}})}{4\pi}\right] \tag{4.5-11}$$

with $\left|\lambda_1(f_{\mathrm{o}})\right|$ the magnitude of the CM with the lowest eigenvalue at f_0. We know from Section 2.2.9 that the maximum value of MED is 4π, and that MED is always positive. Hence maximizing MED is the same as minimizing the 2nd term on the right hand side in (4.5-11).

The goal is to demonstrate the utility of being able to include MED in the objective function; we did not have a specific propagation environment in mind. We therefore used XPR=1 (0 dB) and Gaussian distributions [DOUG 98]

---

[102] Only one significant CM, which we always label as mode $n = 1$.

[103] Of course, once the shaping has been completed, we then decide where the structure will be fed.

$$\mathscr{P}_\theta(\theta,\phi) = A_\theta\, e^{-\left[\theta-\left(\pi/2-m_V\right)\right]^2/2\sigma_V^2} \tag{4.5-12}$$

and

$$\mathscr{P}_\phi(\theta,\phi) = A_\phi\, e^{-\left[\theta-\left(\pi/2-m_V\right)\right]^2/2\sigma_V^2} \tag{4.5-13}$$

with $m_V = m_H = 0^\circ$, and $\sigma_V = \sigma_H = 40^\circ$. This should result in the shaping attempting to achieve self-resonance and making the azimuth radiation pattern closer to omni-directional. This was indeed the outcome.

4.5.4 Outcome of the Shape Synthesis Process

Fig.4.5-1 compares the azimuth patterns of the present shaped antenna (with MED included in F_{obj}) and that from Section 4.3 where it was not included. It is very clear that the present antenna is more omni-directional, the maximum-to-minimum variation decreasing to 2.8dB from a value of 7.8dB when the MED was not included in F_{obj} in Section 4.3. But there has been a price to pay. The elevation patterns of the present antenna in Fig.4.5-1(b) show that there is now a dip in the pattern for the $\phi = 135^\circ$ elevation plane; this does not occur for the shaped antenna in Section 4.3. Note, however, that the shaping scheme, being mindful of the desired MED, has ensured that this dip does not occur in the azimuth plane. It has attempted to "twist" it out of the region of MED interest. The shape synthesis manager has ensured that we have gotten what we asked for, as defined by F_{obj}. In the interests of completeness, we show the present shaped antenna geometry

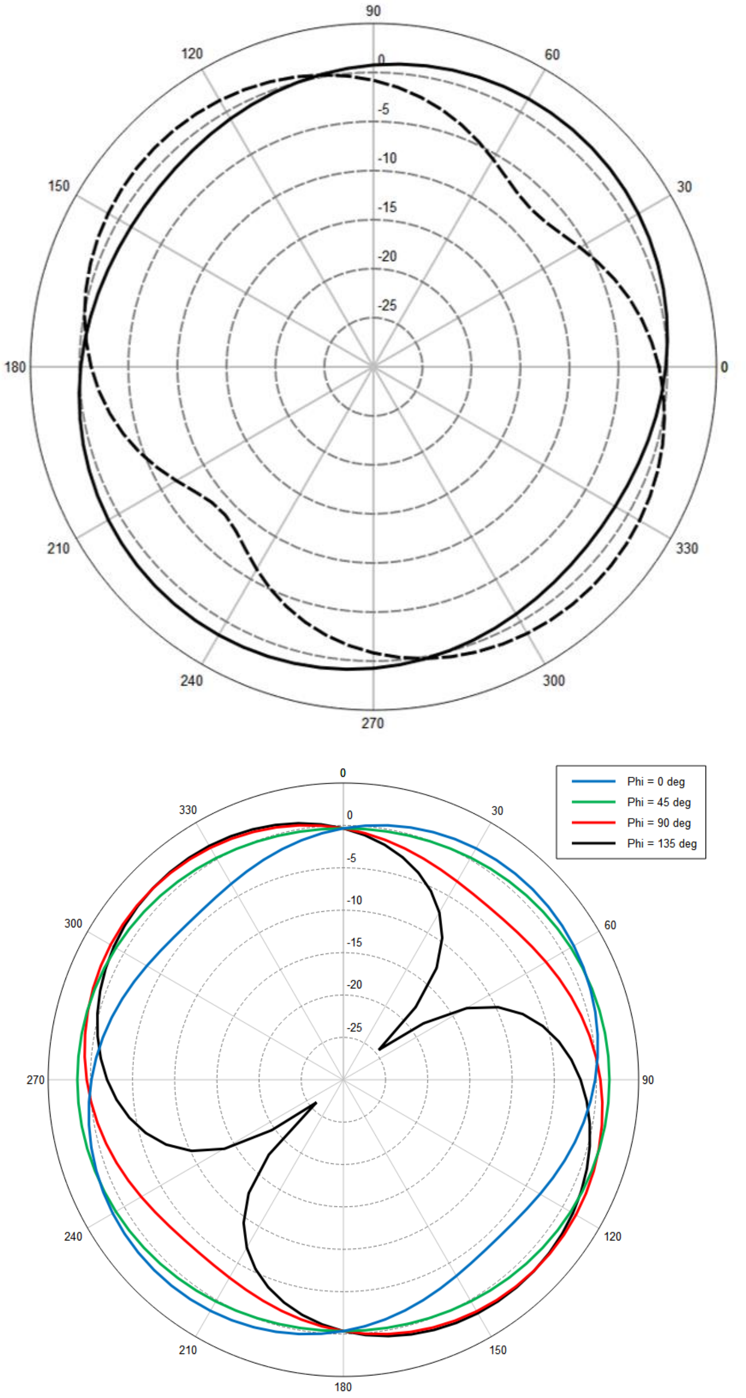

Fig.4.5-1 : Computed total gain patterns (in dBi). The azimuth plane cut is shown in (a), as the solid line, along with the corresponding result from Section 4.3 shown as a dashed line. The plane cuts shown in (b) are for $\phi = 0^\circ$, $\phi = 45^\circ$, $\phi = 90^\circ$ and $\phi = 135^\circ$.

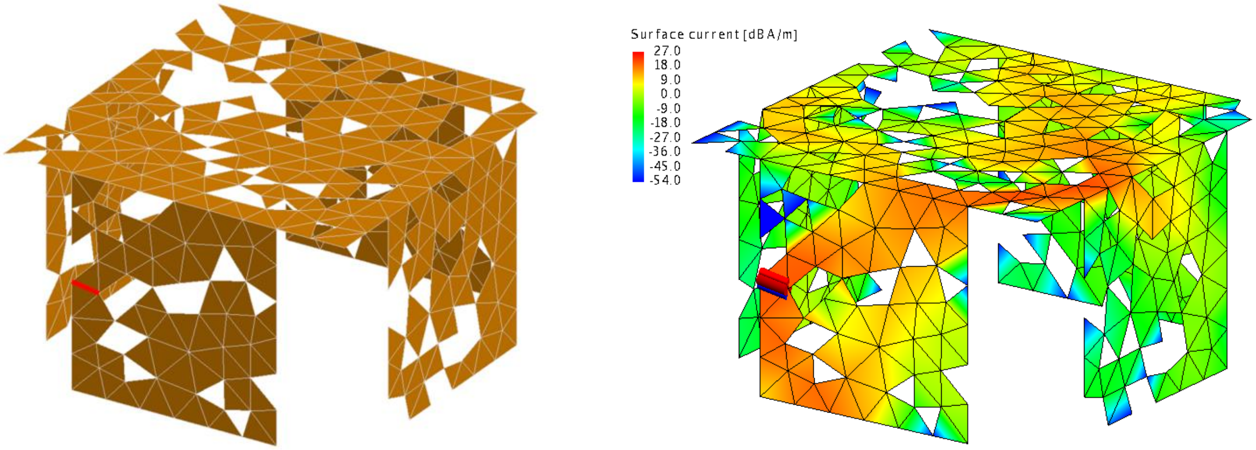

Fig.4.5-2 : (a). The geometry of the shaped antenna, and (b). Current distribution on the driven antenna.

4.6 POSSIBLE EXTENSIONS

It is known [COLL 19] that the "platform" on which an antenna that is of small or intermediate electrical size (with its required broad radiation patterns) can have a significant influence on the antenna performance. If it is possible to model the platform, plus the antenna proper, in the CEM engine, then the process just described in this chapter can tale into account the effects of the platform by using the sub-structure CMs of the antenna proper (or rather, the starting object which is shaped into the antenna) in place of the conventional CMs that have been used. If such sub-structure CMs are used the shape synthesis procedure is valid even if the platform (but not the starting object) is electrically large. The main difficulty is that an electrically large structure is computationally taxing for the MM that we need to use as the underlying CEM analysis to find the CMs.

In the example of Section 4.4 the "battery" effects were accounted for by simply designating the battery as a region which could not be altered. An alternative approach would be to use the sub-structure CM concept with the battery being Object#B, and then shape Object#A using its sub-structure CMs in the shaping process. One advantage of this is that if the interior of the starting shape (Object#A) is occupied by both conducting and dielectric material (eg. to more carefully the scattering effects of the embedded electronics), this could be accommodated in the sub-structure CM concept[104].

---

[104] Sub-structure characteristic modes will be used in Chapter 5, albeit for slightly different purposes.

The computational time to perform a complete shape synthesis described in Sections 4.2 through 4.5 is large, that the DMM approach has been exploited in the shaping manager to reduce this. A large portion of the time is spent on the eigenanalyses needed to find the CMs of each candidate shape in the population for each generation. This could be parallelized.

It is possible to augment F_{obj} with additional terms, as was done in Section 4.5, as long as such terms can be expressed purely in terms of CM quantities. The quality factor term in expression (2.2-53) thus could be used to augment F_{obj} in an effort to squeeze out some more bandwidth. However, as remarked at the end of Section 4.2.5 this might do what we ask, but decrease R_{in} for example. There is a trade-off. As [COLL 19] reminds us, for instance, "efficiency and bandwidth can be traded, but they cannot be maximised together".

4.7 CONCLUDING REMARKS

A recent authoritative paper[105] [COLL 19] based on its author's many years of practical experience identifies a number aspects related to the design of "small antennas". In particular, it refers to antennas whose applications will be in sensors that perform "monitoring, measuring and metering in almost every area of economic and social activity", within the framework of the Internet-of-Things. Several statements relevant to the present work can be extracted from [COLL 19]:

- The electrical smallness of the antenna, and sometimes even the platform, is a challenge.
- Antenna performance is a function of the shape and size of the whole platform.
- Accounting for nearby conducting objects is crucial.
- The industrial design of the platform is often "unfriendly to antennas".

The examples discussed in this chapter (and pre-emptively summarized in Section 4.1.1 at its beginning) have shown that shape-synthesis can in principle contribute significantly to the accounting of the matters bulleted above and, with the availability of the shaping tool, can do so in practice. The success, in practical terms, of the shape synthesis process, and hence the shaping manager that has been developed, is dependent on the accuracy of the CEM modelling used. Any improvements in the CEM engine used will seamlessly improve the usefulness of the shaping process. Nevertheless, some experimental work was done as a "sanity check".

---

[105] We mention [COLL 19] as a footnote here for convenience : B.S.Collins, "Practical application of small antennas in hardware platforms", *IET Microwaves, Antennas & Propagation*, Vol.13, No.11, pp.1883-1888, 2019.

An insightful comparative study of a very large number of electrically small and intermediate-size antennas was done in [SIEV 12]. Fig.4.7-1 shows an illuminating graph taken from this reference. In order to place our shape-synthesized antennas in this context we have shown “windows” within which the performance of the examples in Section 4.2 through 4.4 lie. They are “frames” instead of “dots” because we used computed or measured bandwidths with computed radiation efficiency, and radiation efficiency multiplied by a factor 0.66, as described in Appendix A, whatever combinations were available for a particular example, and so obtained more than one $B\eta_{rad}$ value for each antenna. The shape-synthesized antennas clearly have a better performance than some other published antennas, but have a lower $B\eta_{rad}$ than some others of the same electrical size. The difference between the shaped ones obtained in this chapter is that we have been able to *achieve this performance even though the antenna is constrained to lie precisely on the surface prescribed*. This is not so with any of the antennas whose $B\eta_{rad}$ points are shown on the graph.

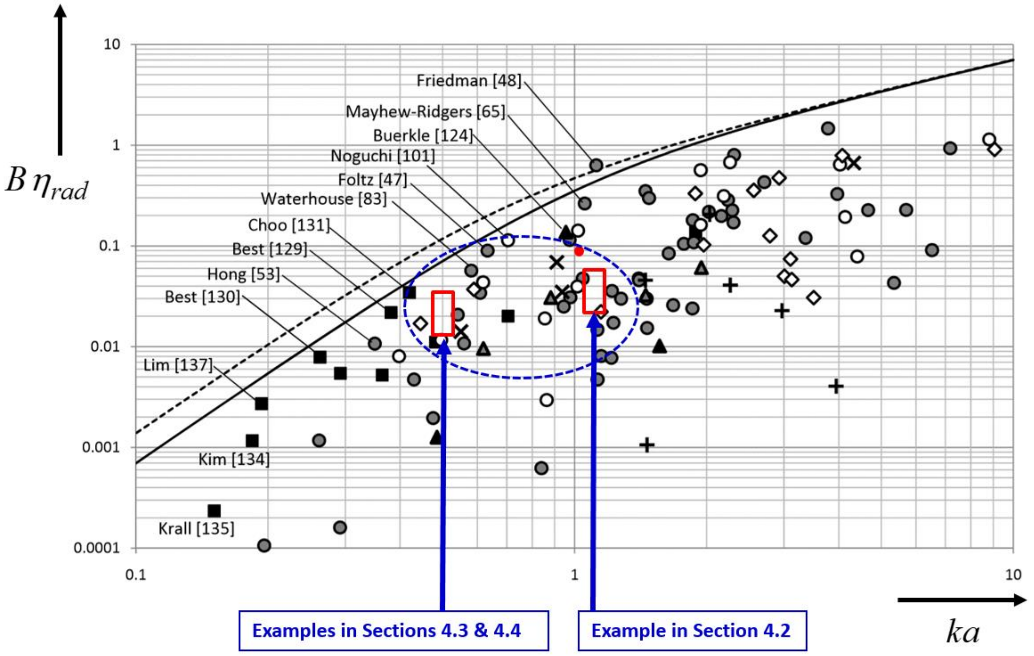

Fig.4.7-1 : Compendium of bandwidth-efficiency products ($B\eta_{rad}$) of numerous antenna designs after [SIEV 12], showing the location of this measure for the antennas shape-synthesized in Sections 4.2 through 4.4 as “red frames”. The vertical axis is the bandwidth-efficiency product and the horizontal axis is ka, with a the radius if the minimum sphere.

CHAPTER 5

The Shape Synthesis of Closely-Spaced Antennas

5.1 PRELIMINARY REMARKS

In Section 2.6.3 we referenced an existing method for the shape synthesis of single electrically-small or intermediate-size (‘single-mode’) antennas for which the feed location need only be selected after the shaping has been performed, but noted that its use had been demonstrated for planar conducting antennas only. Chapter 4 removed this geometrical restriction, and successfully extended the shape synthesis technique to that of antennas comprised of 3D conducting surfaces, for the first time. It was done using a new shape synthesis tool whose development was detailed in Chapter 3; such a facility has not been previously available.

The present chapter extends the shape synthesis work to the case of two closely-spaced antennas that operate at two different frequencies. The sub-structure characteristic mode concept is exploited in a completely new way. As in Chapter 4, we are concerned with a synthesis in which the shape of the final antenna structures is an outcome of the synthesis process, there being some starting shape that is perturbed by the synthesis procedure to produce the final antenna shapes. In addition, the selection of the feed-point of each of the two antennas must only need to be done after the shaping.

Precisely what is meant by “two closely spaced antennas” is explained in terms of the specification of the starting geometry for the synthesis process in Section 5.2. Section 5.3 points out why a simple extension of what has been done in Chapter 4 by using appropriately altered objective functions, is not necessarily an acceptable option. A new shaping prescription is then described in Section 5.4, and it is pointed out how this can be accommodated by the shaping tool developed in Chapter 3. Section 5.5 describes an example of such closely-spaced-antenna shaping and provides experimental validation. Section 5.6 concludes the chapter.

5.2 CLOSELY-SPACED ANTENNAS : STARTING GEOMETRY

We begin with a starting geometry, which consists of two conducting objects that will be referred to as Object#A and Object#B, as was done when discussing sub-structure characteristic modes in Section 2.4.3. This is depicted in Fig.5.2-1. These objects must together now be shaped to provide two antennas. We require that after shaping there must eventually be a feedpoint on Object#A that that acts as the feedport for an antenna that operates at frequency f_a, and a similar feedport on Object#B that acts as the feedport for an antenna operating at f_b. This is shown schematically in Fig.5.2-2. Without loss of generality we assume $f_a < f_b$. When the feedport on Object#A is excited we have an antenna that utilizes both Object#A and Object#B, and we will call this Antenna#A. Similar comments apply to Antenna#B.

We assume the dimensions of the starting shapes are chosen such that, *individually*, each *separate* object is electrically not too large, at f_a and f_b, respectively. But the other object may be electrically large. In other words, Object#A has a ka value[106] at frequency f_a that allows it to be a single-mode structure[107] *in a sub-structure CM sense*, even though the two objects taken together may not be sufficiently small electrically that the combined structure is single-mode *in a conventional CM sense* at f_a. Similarly, Object#B has a ka value at frequency f_b that allows it to be a single-mode structure *in a sub-structure CM sense*, even though the two objects taken together may not be sufficiently small electrically that the combined structure is single-mode *in a conventional CM sense* at f_b. Frequencies f_a and f_b could be widely separated, as long as the above conditions apply. The overall starting geometry, which includes both starting objects, is meshed[108] into a set of triangles. The mesh should be sufficiently dense to ensure accuracy of the computational electromagnetics (and so should be so at the highest frequency of interest) and to provide sufficient geometrical resolution for the shaping process.

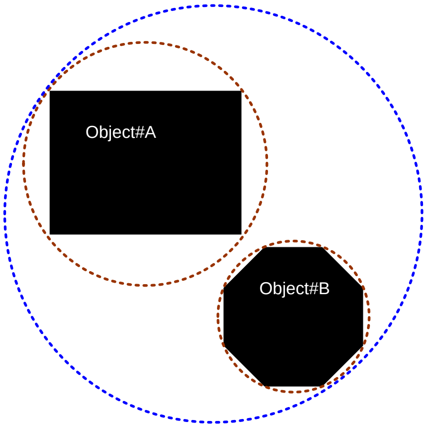

Fig.5.2-1 : Two closely-spaced starting shapes.

---

[106] We continue to use the symbol a to denote the radius of the minimum sphere surrounding each object *separately*.

[107] Recall that the shape synthesis method works when the object being shaped is "single-mode" in the sense that only one dominant CM is sufficient to describe the behavior of the antenna.

[108] All the steps outlined in this chapter are of course executed by the shaping manager described in Chapter 3.

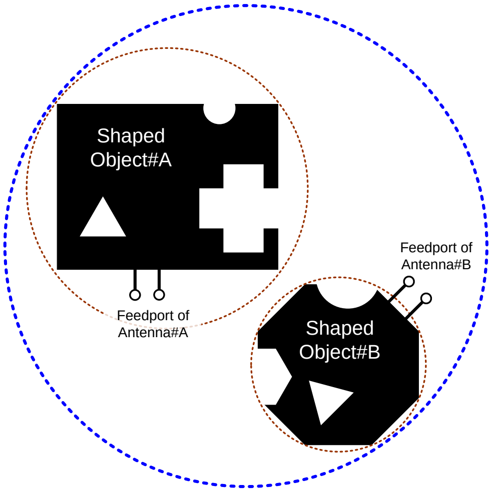

Fig.5.2-2 : Two closely-spaced shape-synthesized antennas.

5.3 OBJECTIVE FUNCTIONS

Similar to what was done in Chapter 4 when using conventional CMs, except that here we use the eigenvalues of the sub-structure CMs of Object#A and Object#B[109] respectively, we can define objective functions for Antenna#A and Antenna#B as

$$F_{obj}^{A} = \left|\lambda_1^{Asub}(f_a)\right| \tag{5.3-1}$$

and

$$F_{obj}^{B} = \left|\lambda_1^{Bsub}(f_b)\right| \tag{5.3-2}$$

We might be tempted to suggest that the closely-spaced antenna synthesis can then be done by simply defining some composite objective function such as (with w_1 and w_2 being user-selected weights)

$$F_{obj} = w_1\left|\lambda_1^{Asub}(f_a)\right| + w_2\left|\lambda_1^{Bsub}(f_b)\right| \tag{5.3-3}$$

$$F_{obj} = \underset{a,b}{Max}\left\{\left|\lambda_1^{Asub}(f_a)\right|,\left|\lambda_1^{Bsub}(f_b)\right|\right\} \tag{5.3-4}$$

or even

---

[109] Given the terminology introduced in Section 5.2, it is incorrect to talk of the sub-structure CMs of Antenna#A or Antenna#B, since these antennas will eventually "use" both objects to fulfil their duties.

$$F_{obj} = \frac{1}{2}\sqrt{\left|\lambda_1^{Asub}(f_a)\right|^2 + \left|\lambda_1^{Bsub}(f_b)\right|^2} \tag{5.3-5}$$

The latter objective functions incorporate the dominant eigenvalues of both sub-structure modes, at frequencies f_a and f_b, respectively. We could instruct the shaping manager execute the GA to shape synthesize both objects simultaneously by minimising (5.3-3), (5.3-4) or (5.3-5). The problem with this shaping prescription is that the feed locations resulting from the shaping may both lie on one of the two objects. Section 5.1 has recognized that this is not what is desired in most such two-antenna situations; we want the respective ports to end up on physically different objects. An alternative shaping prescription is needed.

5.4 SHAPING PRESCRIPTION

The alternative shaping prescription is best explained by referring to the flowchart in Fig.5.4-1. In the shaping prescription used in Chapter 4 some trial runs were first performed, and then these were followed by actual runs that eventually produced the shaped antenna. This was described in Section 3.9. A similar philosophy is used here.

The first step is to perform a trial run of the GA to shape Object#A using its dominant sub-structure eigenvalue (at f_a) to minimize $F_{obj}^A = \left|\lambda_1^{Asub}(f_a)\right|$, without altering Object#B. At the end of this trial run Object#A will have been altered. Then a trial run of the GA is performed to shape Object#B using its dominant sub-structure eigenvalue (at f_b) by minimizing $F_{obj}^B = \left|\lambda_1^{Bsub}(f_b)\right|$, without any shaping of the (now-altered) Object#A. At the end of this trial run Object#B will have been altered. In other words, both objects are now different from their starting shapes. As in Chapter 4 these trial runs will have provided “advice” on various parameter settings for the GA. Actual runs are then executed as follows : An actual run (consisting of several generations) is carried out to minimise F_{obj}^A and hence further shape Object#A without altering Object#B. An actual run (again consisting of several generations) is then carried out to minimise F_{obj}^B and hence further shape Object#B without altering the current shape of Object#A. This pair of actual runs can be called an iteration, as shown in Fig. 5.4-1. These iterations are then repeated until both of the fitness functions are satisfactorily minimised.

At the end of the shaping process the mesh density on the resulting shapes is refined if necessary, the sub-structure modes at the respective frequencies computed, and the modal currents on the objects observed. This allows one to select feedpoints in the manner described in Section 3.10.

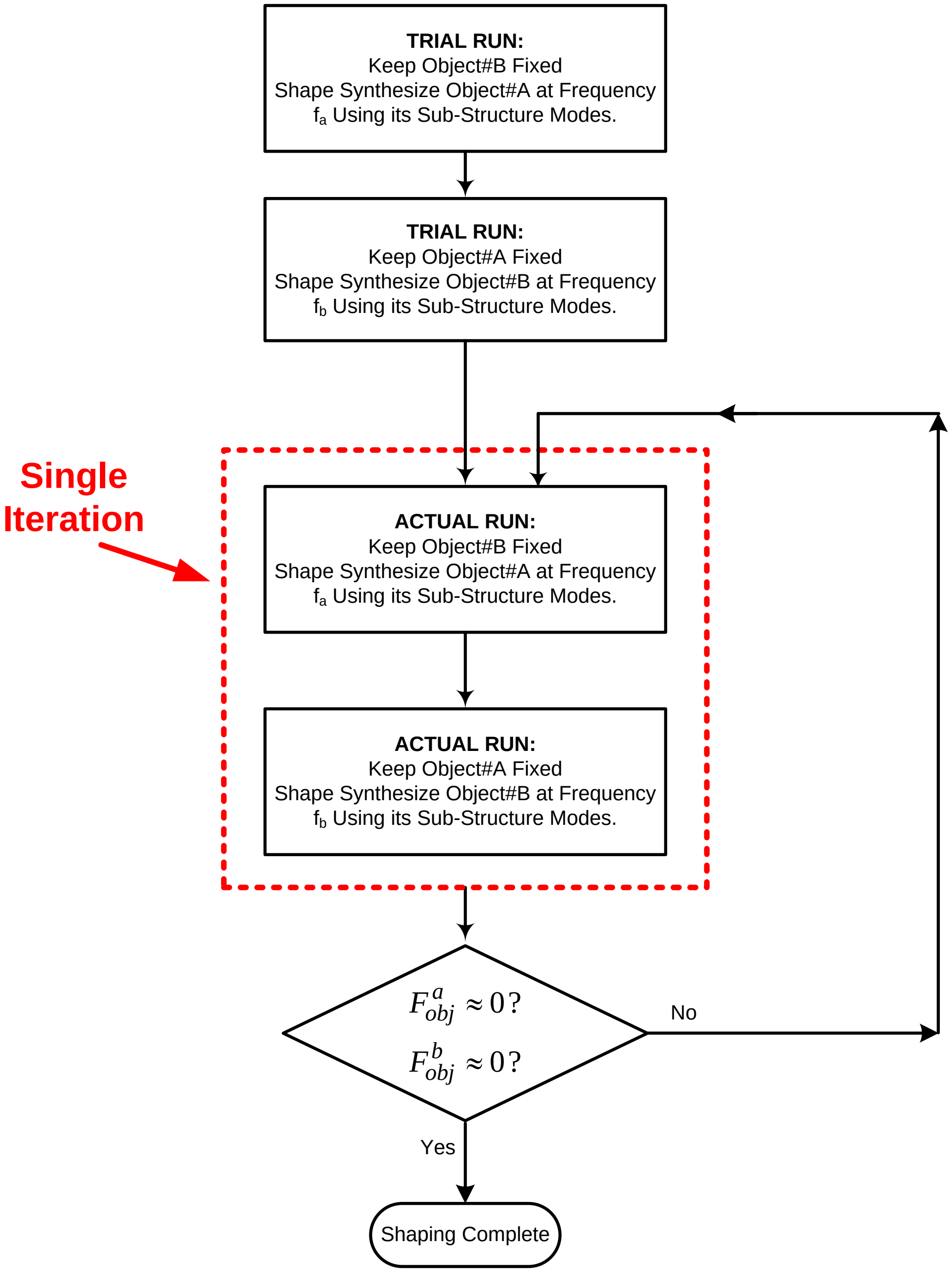

Fig. 5.4-1 : Trial Run - Flowchart#4

5.5 SHAPE SYNTHESIS EXAMPLE : TWO ANTENNAS WITH BROADSIDES PARALLEL

5.5.1 Starting Geometry & Shaping Constraints

We use the starting geometry structure in Fig.5.5-1, consisting of two parallel conducting plates (Objects #A and #B). The goal was to shape synthesize two antennas, one to operate at $f_a = 1.5GHz$ and the other at $f_b = 2.0GHz$. The dimensions were $d_a = 60\text{mm}$, $d_b = 40\text{mm}$ and $h = 24.5\text{mm}$. We again let the symbol a represent the radius of the minimum sphere, depicted by the outer (blue) circle in Fig.5.2-1, and assume $d_a \geq d_b$. Some analytical geometry then shows that the minimum sphere radius is $a = d_a / \sqrt{2}$ as long as $h \leq \sqrt{2d_b(d_a - d_b)}$. In this case, therefore, $a = 42.4\text{mm}$, and $ka = 1.33$ at f_a, whereas we have $ka = 1.78$ at f_b. It should be remembered that this minimum sphere encloses both objects.

We have enforced symmetry about the xz-plane. This was done to allow one half of the eventual shaped antenna to be placed above a conducting groundplane. There were no constraints placed on any portions of the geometry (no “disallowed” regions that may not be shaped). The starting shape was densely meshed into $N_\Delta = 844$ triangles, with 592 on Object#A and 252 on Object#B, which resulted in the initial number of degrees of freedom being $N_{\text{dof}} = 1215$.

The shape synthesis procedure outlined in Section 5.4 was used to in essence reduce the eigenvalue of the dominant sub-structure CM of Object#A (Object#B) in the presence of Object#B (Object#A) at f_a (f_b) to values close to zero.

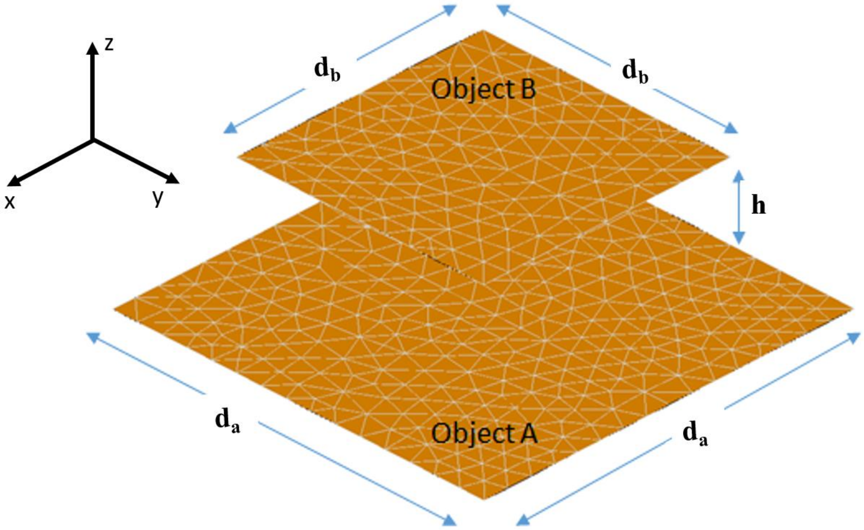

Fig.5.5-1 : Starting conductor shapes used.

5.5.2 Outcome of the Shape Synthesis Process

Since the shaping prescription is different form that used in Chapter 4, some view of how such a prescription progresses is in order. For instance, Fig.5.5-2 shows the behaviour of F^B_{obj} during the actual run of the final iteration. Fig.5.5-3 shows the value of F^A_{obj} (blue circle) and F^B_{obj} (red asterisk), versus the iteration number, at the end of the first actual run (top graph) and the second actual run (bottom graph) in each iteration. It is clear that eventually both antennas (that is, as seen in a sub-structure CM sense) become self-resonant. The shaped antennas, and the resulting feedports, are shown in Fig.5.5-2.

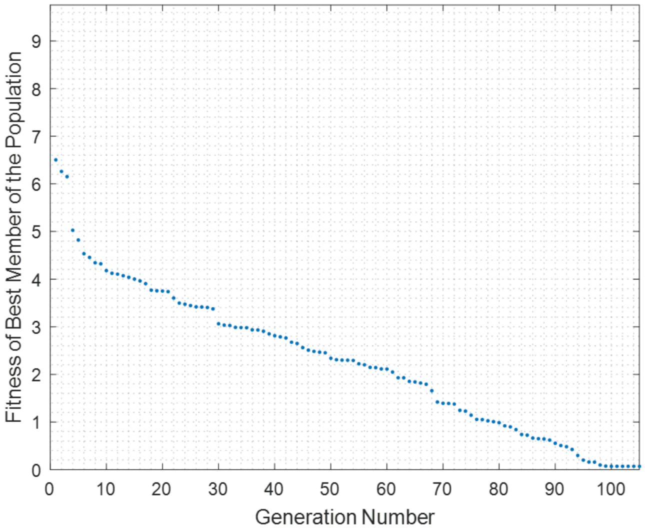

Fig.5.5-2 : Value of F^B_{obj} at the end of each iteration in Fig. 5.4-1

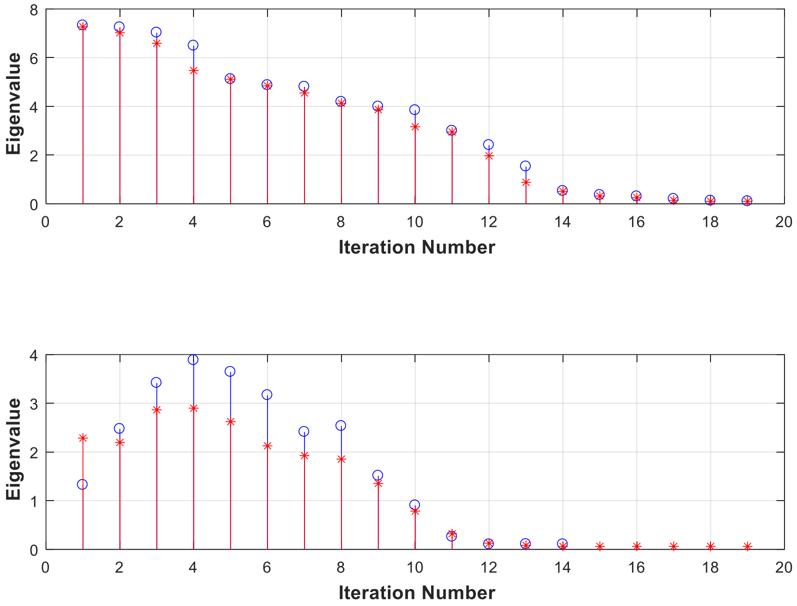

Fig.5.5-3 : The value of F_{obj}^{A} (blue circle) and F_{obj}^{B} (red asterisk), versus the iteration number, at the end of the first actual run (top graph) and the second actual run (bottom graph) in each iteration

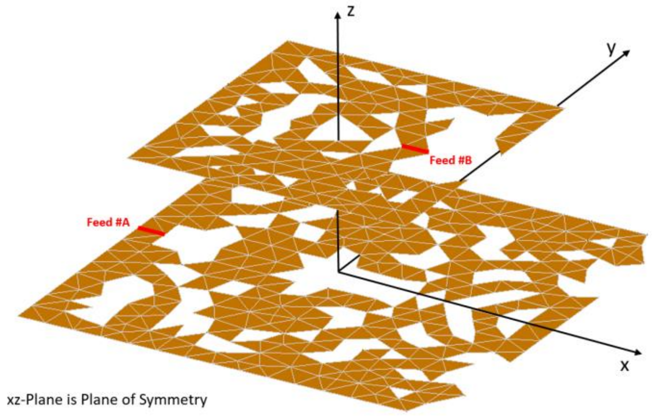

Fig.5.5-4 : Shaped geometry and feed port locations. The port labelled "Feed#A" is the feedport for Antenna#A, and similarly for Antenna#B.

5.5.3 Performance Computation & Measurement of the Shaped Antennas

The current distributions on the complete radiating structure when each of the antenna feed ports are excited in turn, with the other terminated, are shown in Fig.5.5-5 and Fig.5.5-6. It is clear that each antenna relies for its operation on both Object#A and #B. The antennas were fabricated in the same manner as that for the open cuboid in Section 4.2, and of the same material. An annotated photograph of the fabricated antenna pair is shown in Fig.5.5-7.

Two issues should be emphasized. Using this shaping prescription, the method of Section 3.10.1 does indeed ensure the feedports are on different objects, as seen by the feedports of Antenna#A and Antenna#B indicated in Fig.5.5-4 and Fig.5.5-7. Reference to the computed input impedances in Fig.5.5-8(a) and Fig.5.5-9(a) confirms that, as far as the theoretical model is concerned, the antennas are self-resonant at the desired frequencies of 1.5GHz and 2.0GHz, with $R_{in} = 43\Omega$ for Antenna#A, and $R_{in} = 46\Omega$ for Antenna#B, there. Thus the new shaping prescription does successfully achieve the goal set in Section 5.1. We note the unusual character of the impedances in Fig.5.5.9(a) due to the coupling between the objects forming the antenna.

Fig.5.5-11 gives the computed and measured $|\Gamma_{\text{in}}(f)|$ of the shaped antennas. The computed frequencies for minimum $|\Gamma_{\text{in}}(f)|$ are 1.4725 GHz and 2.0005 GHz, slightly shifted[110] from the prescribed (and obtained) self-resonance frequencies of 1.5GHz and 2.0GHz. This can be so because $|\Gamma_{\text{in}}(f)|$ does not appear in any objective function, since it would be necessary to select a feed location before shaping if we wished to do that. In most cases the minimum $|\Gamma_{\text{in}}(f)|$ does occur close to the self-resonance frequency, especially for antennas with smaller ka values. In the present case the ka values of Object#A (taken individually) is 1.3, and so the resulting structure is not as purely single-mode (in its individual sub-structure CM sense) as it would have been had it (individually) been electrically smaller. This results in the shift between the computed self-resonance frequency and frequency of minimum $|\Gamma_{\text{in}}(f)|$ for Antenna#A.

The predicted -9.54dB (VSWR = 2) bandwidths of Antenna#A and Antenna#B, extracted from the $|\Gamma_{\text{in}}(f)|$ plots, are 6.54% and 2.55%, respectively. The corrresponding measured values are[111] 1.42% and 7.3%. Furthermore, the computed and measured frequencies for minimum $|\Gamma_{\text{in}}(f)|$ for Antenna#A differ by some 150 MHz. This is attributed to fabrication errors.

---

[110] Although the computed $|\Gamma_{\text{in}}(f)|$ values there are better than -14dB.

[111] It is unclear why there is such a large difference between the measured and computed bandwidths.

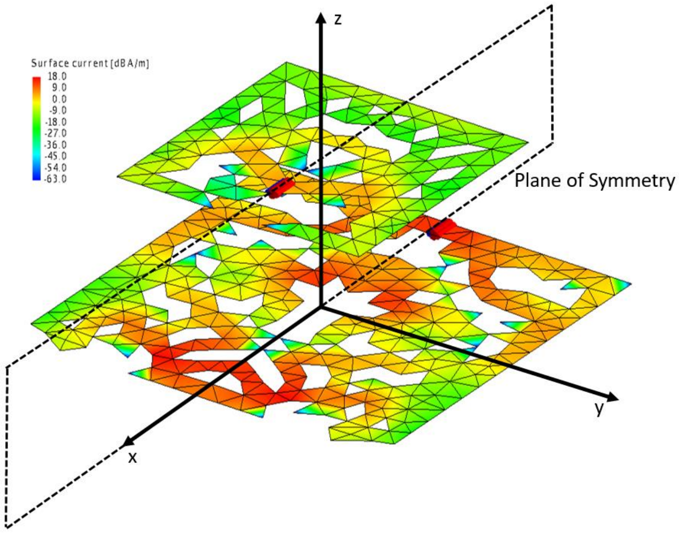

Fig.5.5-5 : Computed current distribution (at $f_a = 1.5\,\text{GHz}$) on the complete radiating structure when excited at the feed port of Antenna#A.

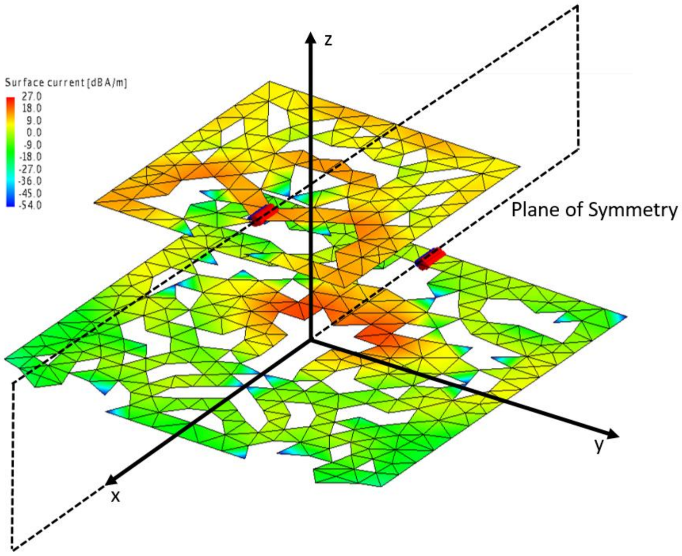

Fig.5.5-6 : Computed current distribution (at $f_b = 2.0\,\text{GHz}$) on the complete radiating structure when excited at the feed port of Antenna#B.

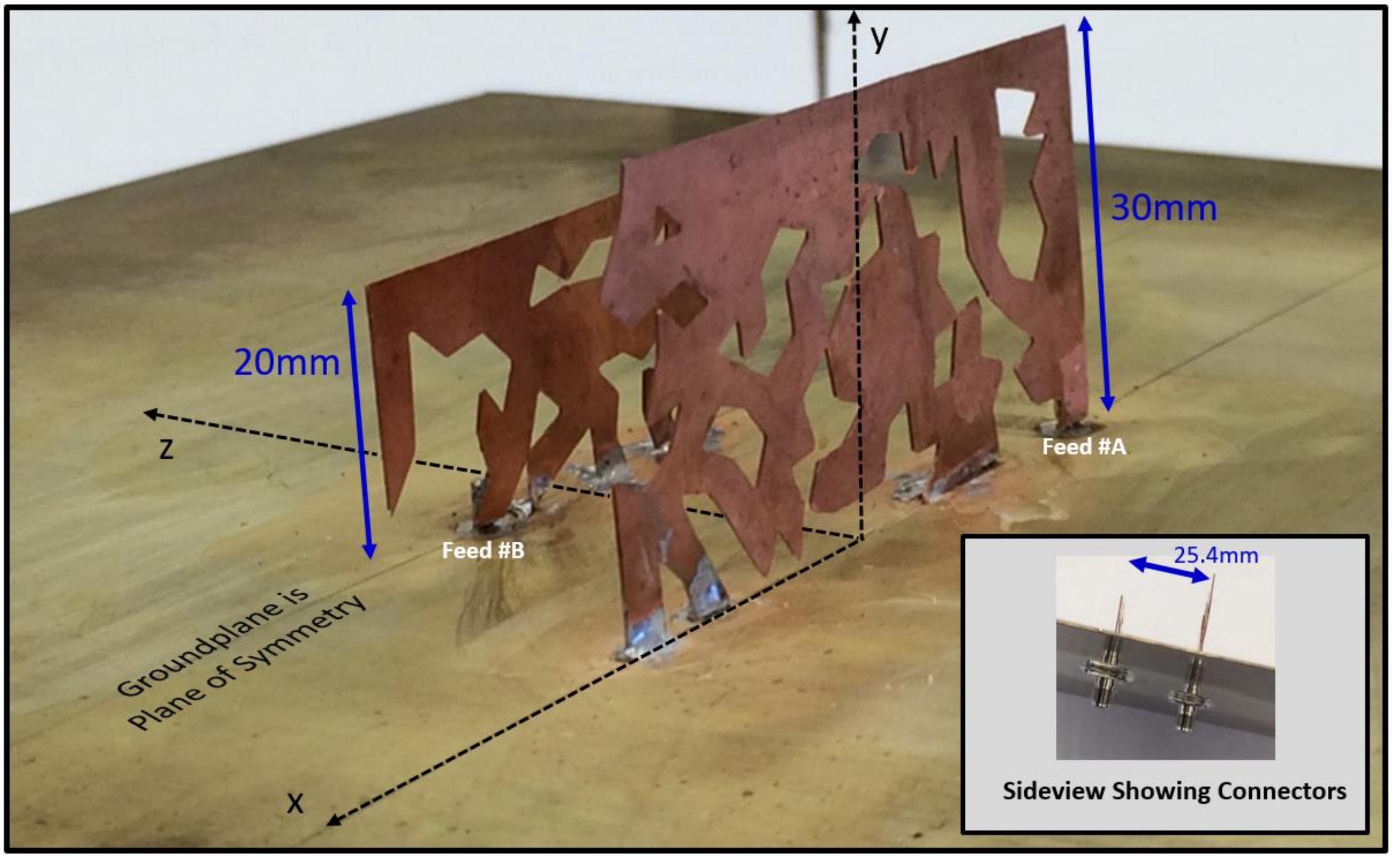

Fig.5.5-7 : Photograph of the fabricated antenna structure.

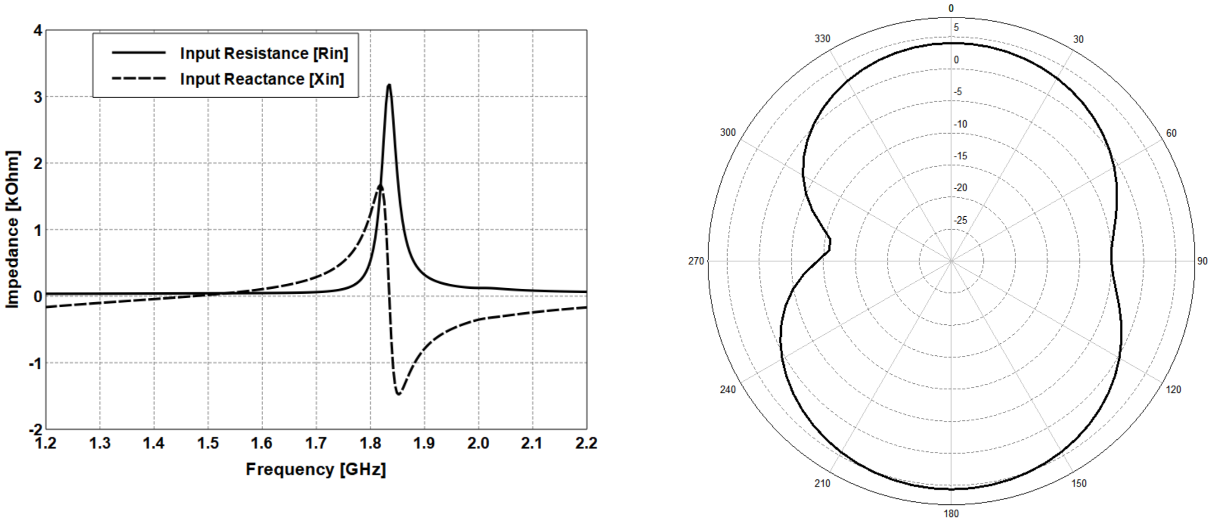

(a) (b)

Fig.5.5-8 : (a). Computed input impedance at the feed port of Antenna#A. (b). Computed total gain in the azimuth plane (xz-plane) of Antenna#A.

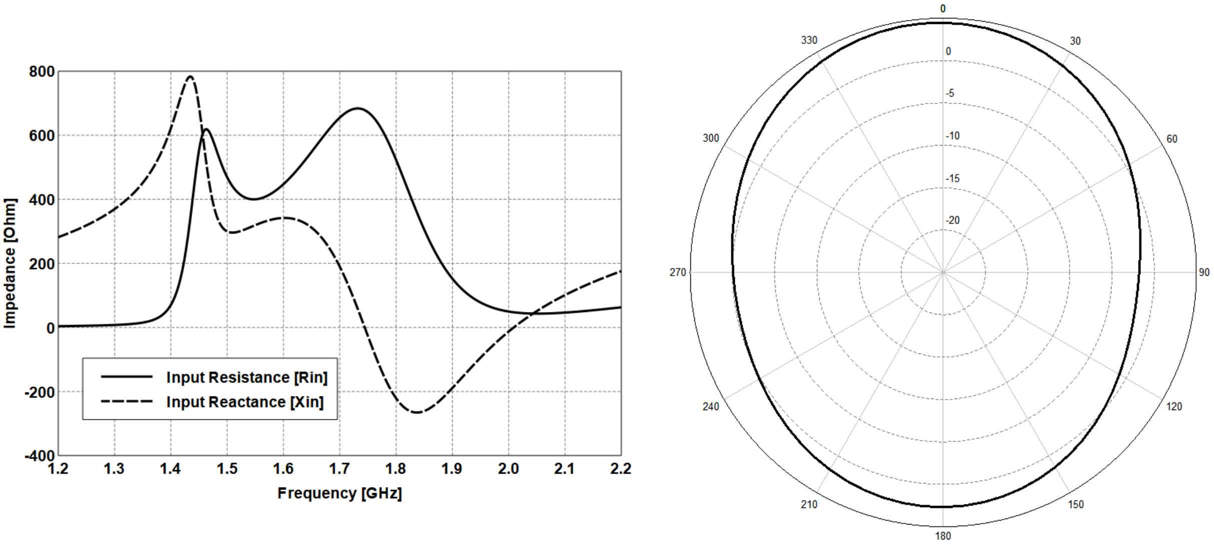

Fig.5.5-9 : (a). Computed input impedance at the feed port of Antenna#B. (b). Computed total gain in the azimuth plane (xz-plane) of Antenna#B.

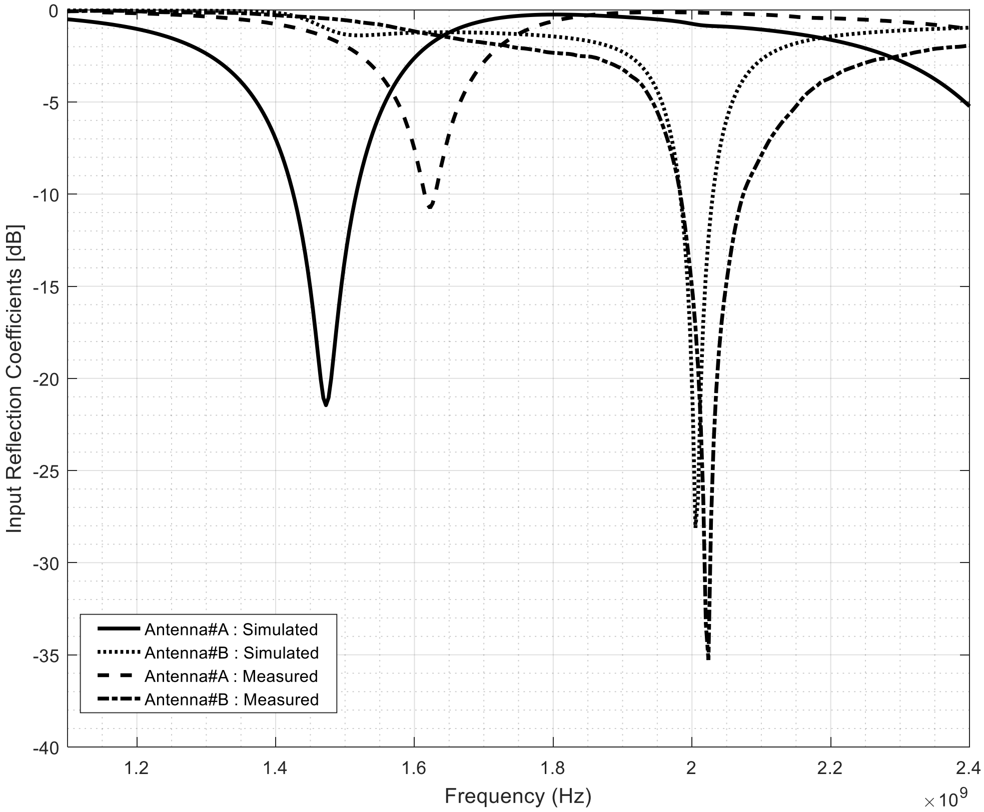

Fig.5.5-10 : Computed and measured input reflection coefficients (referenced to 50Ω) of the two antennas at their respective feed ports.

5.6 POSSIBLE EXTENTIONS

The sub-structure CM formulation in Section 2.4.3 can be extended from one involving two objects to one involving more than two objects. For example, two closely-spaced antennas on an electrically large platform, operating at different frequencies, could be shaped. The two objects to be shaped (as has been done earlier in this chapter) would be Objects #A and #B as before, and the vehicle Object#C that is not altered by shaping. As long as the ka for Objects#A and Object#B, taken individually, is sufficiently small, these will be single-mode in a sub-structure sense. And hence the shape synthesis procedure can be applied. Furthermore, one could define three objects as just suggested, where the third is not an electrically large platform, but a third antenna, operating at a third frequency, which is also to be shaped. We have not exercised the shaping tool for such cases because of the computational burden.

5.7 CONCLUDING REMARKS

At the start of Chapter 5 we stated a different two-antenna requirement, and devised a new shaping prescription to achieve this. The shaping manager developed in Chapter 3 is such that the above shaping prescription could be incorporated in a relatively routine manner. This is important, as different ones can arise for different design requirements. It was then demonstrated by an example, and some experimental backing, that the shaping prescription is able to achieve its goal. It provides self-resonance at the specified frequencies of the two closely-spaced antennas, with each antenna “leaning” on the other to achieve the desired performance at its particular operating frequency. It is a “shape-first feed-next” procedure that ensures that each of the resulting feedports is on a different object. This sort of shape synthesis has previously not been reported elsewhere.

CHAPTER 6

Sub-Structure Characteristic Mode Computation Utilizing Field-Based Hybrid Methods

6.1 GOALS OF THE CHAPTER

Chapter 3 developed the machinery for a complex computational electromagnetics-based tool capable of performing the shape synthesis of 3D conducting surface antennas through use of a full-wave method of moments approach combined with the genetic optimisation algorithm.

Using this tool, Chapter 4 demonstrated for the first time how characteristic mode concepts can be utilized to shape synthesize 3D conducting surface antennas, using the “shape-first feed-later” approach.

Chapter 5 extended the shape synthesis methods, using sub-structure characteristic modes, to the case of closely-spaced antennas operating at different frequencies. One begins with two adjacent starting structures from which two antennas are to be shaped, with the feed locations identified by the process, once shaping is complete, situated separately on each of the two structures. One of the antennas can operate at a much lower frequency than the other, since the single-mode requirement of the said shape synthesis method is preserved through use of the sub-structure instead of conventional modes. We mentioned at the end of Chapter 5 that the sub-structure approach can relatively easily be extended to the case of two structures (that must be shaped in the manner stated) are situated in the presence of a third very much (electrically) larger object, such as a platform of some sort. The question arises as to what one could do if the size of this third object, for instance, is electrically so large that a MM analysis is not feasible.

Several researchers have, in verbal discussions at engineering conferences, pondered the idea of using asymptotic methods to find the (sub-structure) characteristic modes of an object that sits on such a platform that is electrically very large. In this chapter we demonstrate, for the first time, how this can be achieved through the use of field-based hybrid MM/GTD methods. The fundamental concept is described in Section 6.2. Section 6.3 uses the method in an example. Sections 6.4 concludes the chapter.

In Section 2.4.3 the altered MM matrix for the sub-structure CM eigenvalue problems was denoted by the symbol $[Z_{\mathrm{sub}}]$, as has become customary. In the context to be discussed in the present chapter (and only for this chapter) we will alter the notation slightly in order to improve the clarity of the explanations to follow. Thus some re-stating of facts from Sections 2.4.2 and 2.4.3 will be needed.

6.2 PROPOSED IDEA

Recall from Section 2.3 that if we model the electrically perfectly conducting (PEC) structure in Fig.6.2-1(a) using an EFIE [KRIS 16] for the electric current density $\bar{J}_s$ everywhere on the structure, the MM can be used [VOLA 12] to discretize the EFIE into a matrix equation involving the MM matrix (generalized impedance matrix) $[Z]$. If the object is alone in free space, the kernel of the EFIE will be a free space Green's function, and we can write, for ease of explanation in the present paper at least, the MM matrix as $[Z]=[Z^{fs}]$. The "fs" explicitly recognizes the use of the free-space Green's function in the EFIE. It is then possible (see Section 2.4.2) to find the characteristic modes (CMs) of the structure as the solutions of the matrix eigenvalue problem $[X][J_n]=\lambda_n[R][J_n]$, with $[Z]=[R]+j[X]$. Quantities λ_n and $[J_n]$ are the eigenvalue and eigencurrent of the n-th CM, respectively. The far-zone eigenfields can be found for each eigencurrent $[J_n]$, and are mutually orthogonal over the sphere at infinity. In Section 2.4.2 we called these the *conventional* CMs of the PEC structure.

If we wish to find the CMs for a microstrip patch above an infinite groundplane, for example, an EFIE must be used that utilizes a modified Green's function to account for the presence of the infinite groundplane and substrate [CHEN15a][ALRO 15]. The unknown in the EFIE is then the $\bar{J}_s$ on the patch only. The general situation can be depicted as in Fig.6.2-1(b), where an Object#A (eg. a patch) is in the presence of an Object#B (eg. infinite groundplane), with the modified Green's function being that which gives the fields due to any current density radiating in the presence of Object#B. The EFIE unknown would be the $\bar{J}_s$ on Object#A only. Although $[Z]$ would be obtained directly in such a case, without $[Z^{\mathrm{per}}]$ being explicitly computed separately, for the purposes of comparison with what is to be discussed below, we will write it as

$$[Z]=[Z^{\mathrm{fs}}]+[Z^{\mathrm{per}}] \tag{6.2-1}$$

with the superscript "per" intended to indicate "perturbation". It is this $[Z]$ that would be used in the eigenvalue problem mentioned earlier. In order to distinguish the resulting CMs from ones found via integral equation formulations that use free space Green's functions in their kernel, we explained in Section 2.4.3

that these can be called the sub-structure CMs of the patch (say Object#A) in the presence of the infinite groundplane (say Object#B). Finding conventional CMs is not an option, as they would not make sense due to the presence of the infinitely large Object#B. Thus, albeit not often explicitly stated, whenever CMs are used in design work in such circumstances they are in fact sub-structure CMs [ALRO 17].

If the groundplane (of the microstrip patch antenna) spoken of above is of finite extent, which means that an appropriate modified Green's function in analytical form that will account for its presence is not available, sub-structure CMs can still be found. As before (and not only for the patch and groundplane situation), the EFIE uses the free space Green's function, implying that the unknown is the $\bar{J}_s$ on both Object#A and Object#B taken as a whole. But in order to be able to find the sub-structure CMs, when discretizing this EFIE using the MM, distinct expansion function subsets are purposefully located on these two objects, so that the usual MM matrix can be partitioned as[112]

$$\begin{bmatrix} [Z_{AA}] & [Z_{AB}] \\ [Z_{BA}] & [Z_{BB}] \end{bmatrix} \tag{6.2-2}$$

All block matrices in (6.2-2) are found as part of the usual MM procedure. The sub-structure CMs of Object#A in the presence of Object#B are then found from the $[Z]$ in (1), but now with [ALRO 14][ALRO 16][ALRO 18]

$$[Z^{fs}] = [Z_{AA}] \tag{6.2-3}$$

and

$$[Z^{\text{per}}] = -[Z_{AB}][Z_{BB}]^{-1}[Z_{BA}] \tag{6.2-4}$$

The above route for the sub-structure CM eigenvalue problem effectively uses a discrete form of the modified Green's function that accounts for the presence of Object#B, although this Green's function is not needed explicitly. We will, for convenience, here[113] refer to this way of finding the sub-structure CMs as the MM/MM approach; the reason for doing so will become clear later. The reader is referred to [ALRO 16] for a catalogue of the properties of sub-structure CMs; these are similar to their conventional CM counterparts. Previously [ALRO 16] the altered MM matrix for the sub-structure CM eigenvalue problems was denoted by

---

[112] Up to this point in the present chapter the notation is that used in Section 2.4, but this will now change, for reasons mentioned at the end of Section 6.1.

[113] That is, here in Chapter 6, but not elsewhere in the thesis.

the symbol $[Z_{\text{sub}}]$. In the context to be discussed in the present paper we believe the notation in (1) improves the clarity of the explanations to follow. It is also useful to reiterate that, if we were to want the conventional CMs of the entire structure (namely Object#A and Object#B viewed as a single structure) then the $[Z]$ used in the eigenvalue problem would be the complete matrix in (6.2-2). However, if the antenna proper (Object#A) were in the presence of an electrically large Object#B, such as a microstrip patch above a large but finite groundplane, the conventional CMs would lose their usefulness. There would be too many significant conventional CMs, and it would be difficult to relate these to the characteristics of the antenna proper [ALRO 18][OUTW 17]. The use of sub-structure CMs allows the insight lost from conventional CMs in such situations to be gleaned instead from the sub-structure CMs and once more aid design, as discussed in [ETHI 14,Sect.VIII], [BERN 15] and [XIAN 19], for instance.

Now suppose that Object#B is electrically very large, for instance in the case of an Object#A (antenna proper) mounted on a platform. Finding the sub-structure CMs of Object#A using the MM/MM approach may not be computationally feasible if Object#B is electrically too large. Matrix (6.2-2) might be huge even though $[Z^{fs}]=[Z_{AA}]$ is not, and finding $[Z^{\text{per}}]$ as per (6.2-4) might be computationally excessive, especially if needed at several frequencies and if the geometry of Object#A is being repeatedly altered during some design process. In this paper we wish to point out that such a dilemma can be circumvented if $[Z^{\text{per}}]$ is approximated using a MM/GTD hybrid approach. This fact could be discerned, as we have done, from the definition of sub-structure CMs. However, this has not yet been explicitly stated anywhere or example computations provided.

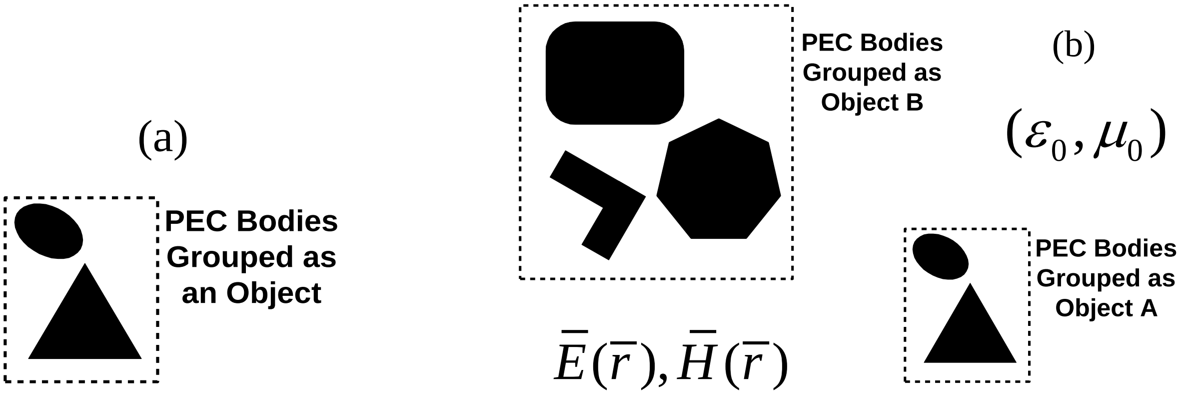

Fig.6.2-1. (a) Several PEC bodies grouped together as a single isolated object, and (b) several PEC bodies grouped as Object A and Object B.

6.3 SUB-STRUCTURE CHARACTERISTIC MODES COMPUTED USING THE MM/GTD HYBRID APPROACH

The field-based MM/GTD method was pioneered by Thiele and co-workers [EKEL 80]. A review of this, as well as current-based hybrid methods, is provided in [MEDG 91], with later enhancements described in [THER 00]. Here we make use of the field-based MM/GTD hybrid method as implemented in FEKO [JAKO 10][JAKO 97][FEKO]. In the context of the present paper Object#A is meshed and expansion functions for the unknown $\bar{J}_s$ defined on it as usually done when using the MM. In spite of the looming presence of the very large Object#B, the free space Green's function is used to determine the fields of each expansion function on Object#A over every other one (as if Object#B did not exist), and hence $[Z^{fs}]=[Z_{AA}]$ is found. These 'first-order' fields are, however, supplemented by finding the contribution of Object#B via the GTD [EKEL 80]. Each expansion function is in turn considered to be a source and the GTD-determined field perturbations over every expansion function used to supply a perturbation $[Z^{\mathrm{per}}]$ to the MM matrix. Expression (6.2-1) then gives the $[Z]$ needed in the eigenvalue problem. The reader is referred to the aforementioned references for details, and information on how the approach is actually implemented in practice. The above description is intended to elucidate the principle only.

Fig.6.3-1 shows a rectangular PEC plate (Object#A) in the vicinity of another large PEC plate arrangement (Object#B). For the numerical experiment to follow Object#B was selected to be large, but not so large that the MM/MM approach to finding the sub-structure CMs was unfeasible[114], because we wish to compare MM/MM and MM/GTD results. If we mesh both Object#A and #B and determine the sub-structure CMs of Object#A with (6.2-4) used to find $[Z^{\mathrm{per}}]$, in other words the MM/MM approach, the first three sub-structure CM eigenvalues obtained are those shown by the solid lines in Fig. 6.3-2. The corresponding eigenvalues of Object#A with Object#B absent (and hence $[Z^{\mathrm{per}}]=0$), namely the conventional CMs of Object#A alone, are shown on the same graph as dashed lines. This has been done merely to show that, as expected, the presence of Object#B has shifted the frequencies at which the CM eigenvalues are zero (the CM resonance frequencies) lower in frequency, due to its 'loading' of Object#A. We show the frequency range over which the eigenvalues are small, because the CMs with small eigenvalues are those of most importance in antenna design.

---

[114] We emphasize, however, that this is for the purposes of this numerical experiment only; the utility of the sub-structure CM computation approach developed in this chapter is precisely that it can be used when Object#B is electrically so large that a MM/MM route would not be feasible. Indeed, even for the numerical experiment in question, Object#B required 300,000 expansion functions.

If we mesh only Object#A, and use the MM/GTD approach to effectively find $[Z^{\text{per}}]$, the sub-structure CM eigenvalues are as shown as the solid lines in Fig. 6.3-3. They clearly approximate those found using the (exact) MM/MM approach well, but without the need to handle the large MM sub-matrices related to the electrically large Object#B. Observe that as the frequency increases the MM/GTD results approach the exact (MM/MM) ones increasingly closely, as anticipated when using asymptotic methods in computations. If the Object#B were not just the portion shown Fig. 6.3-1, but the whole ship in Fig. 6.3-4 from which it was extracted, then the MM/GTD approach would even more computationally attractive. We here used the Object#B in Fig. 6.3-1 simply because we wanted to demonstrate that the sub-structure CMs found via the MM/GTD approach are indeed those obtained using the computationally more demanding MM/MM one. The particular Object#B used was not so large that use of the MM/MM approach was prohibitive. It would be so of Object#B were prohibitively large for the complete structure in Fig. 6.3-4, but the MM/GTD approach would not be.

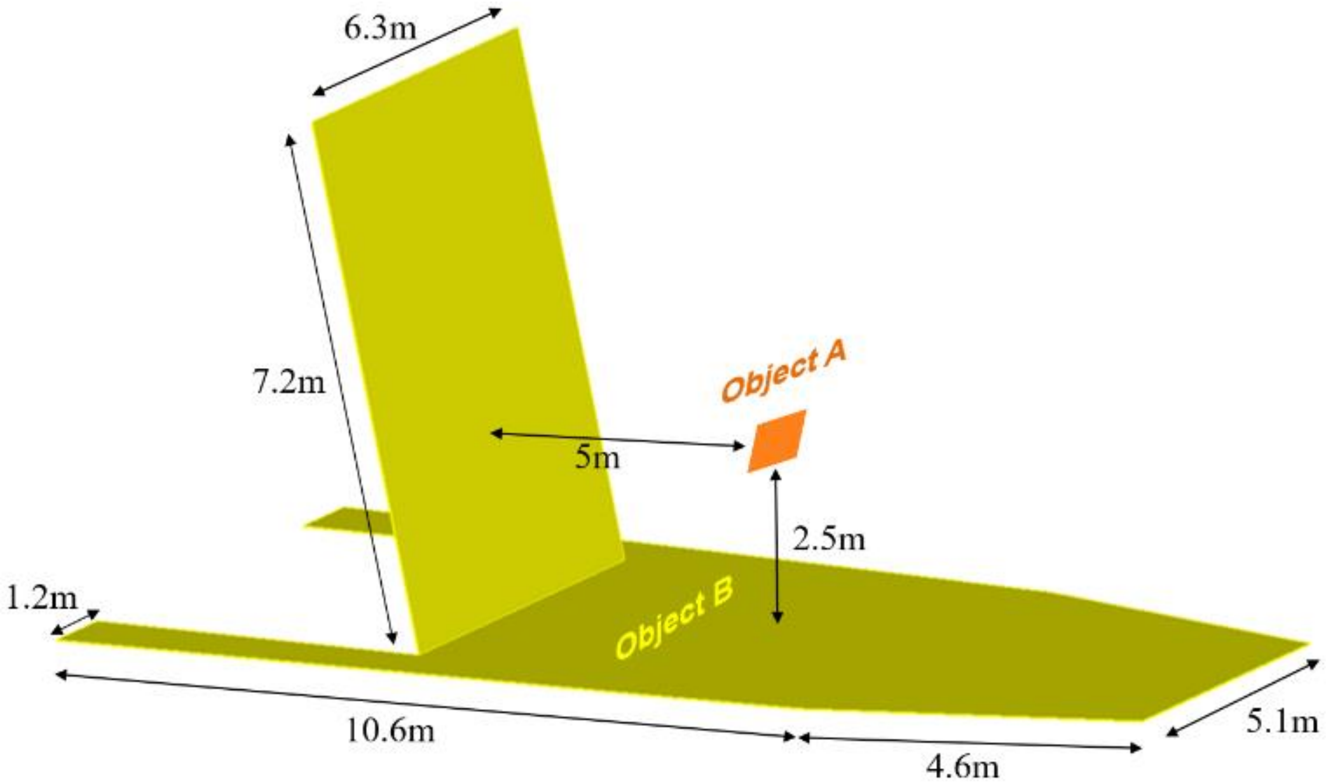

Fig.6.3-1 PEC Object#A (small plate) and Object#B (arrangement of large plates) used in this paper. The size of square PEC plate Object#A is 127.5mm per side. Object#A is shown larger than it actually is in relation to Object#B.

Ray tracing rules[115] [PAKN 16] decide which particular direct, reflected, edge-diffracted, corner-diffracted and double-diffracted contributions are included in effectively finding $[Z^{\text{per}}]$ in the MM/GTD approach. The manner in which the eigenvalues from the MM/GTD approach move closer to the exact MM/MM ones as more GTD ray types are included is demonstrated in Fig. 6.3-5. As a further check the coupling integral[116] C_{mn} [HARR 71a,Eq(22)] between the sub-structure CM far-zone fields found using the MM/GTD method was computed. The results for the first five modes are shown in Fig. 6.3-6. Theoretically[117] the value for $m \neq n$ should be zero, but are here around -40dB or lower, which is expected in actual CM computation.

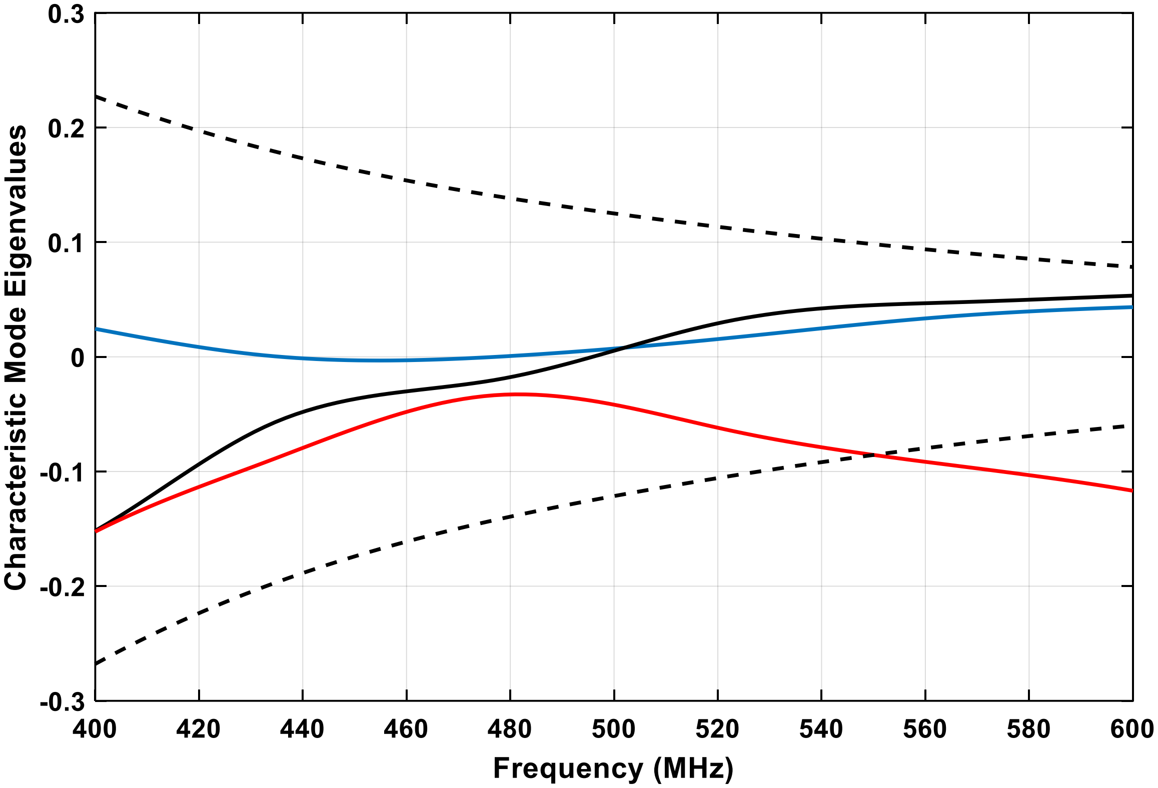

Fig.6.3-2 Eigenvalues of the 1st (——), 2nd (——) and 3rd (——) sub-structure CMs obtained using the MM/MM approach to find $[Z^{\text{per}}]$. Eigenavlues (- - -) of the first three (two of which are degenerate) conventional CMs of Object#A in the absence of Object#B.

---

[115] Briefly discussed in Section 2.3.5.

[116] Defined in Sections 2.4.2 and 2.4.3.

[117] But never precisely so numerically.

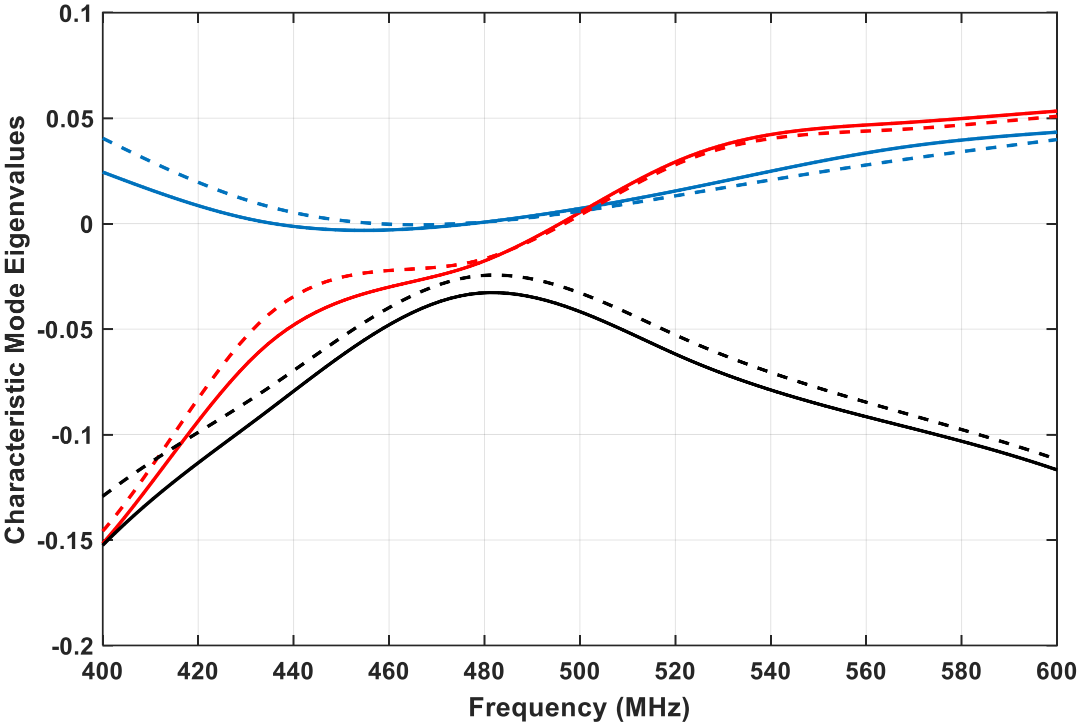

Fig.6.3-3 Eigenvalues of the 1st (blue), 2nd (red) and 3rd (black) substructure CMs computed using the MM/GTD method. Those found using the MM/MM (exact) approach to find $[Z^{\mathrm{per}}]$, as in Fig.6.3-2, are shown as dashed lines. Those found using the hybrid MM/GTD approach to find $[Z^{\mathrm{per}}]$ are shown as solid lines.

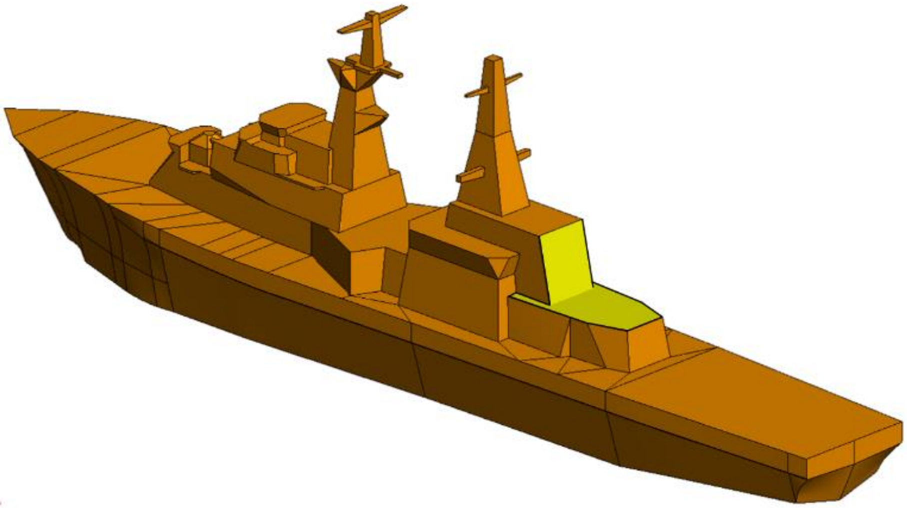

Fig.6.3-4 Ship model from which the Object#B in Fig.6.3-1 was extracted. The sections on the rest of the model are for visualisation reasons only; they do not represent the mesh needed for computational purposes using the method of moments. The ship model is courtesy of Altair Inc. [FEKO].

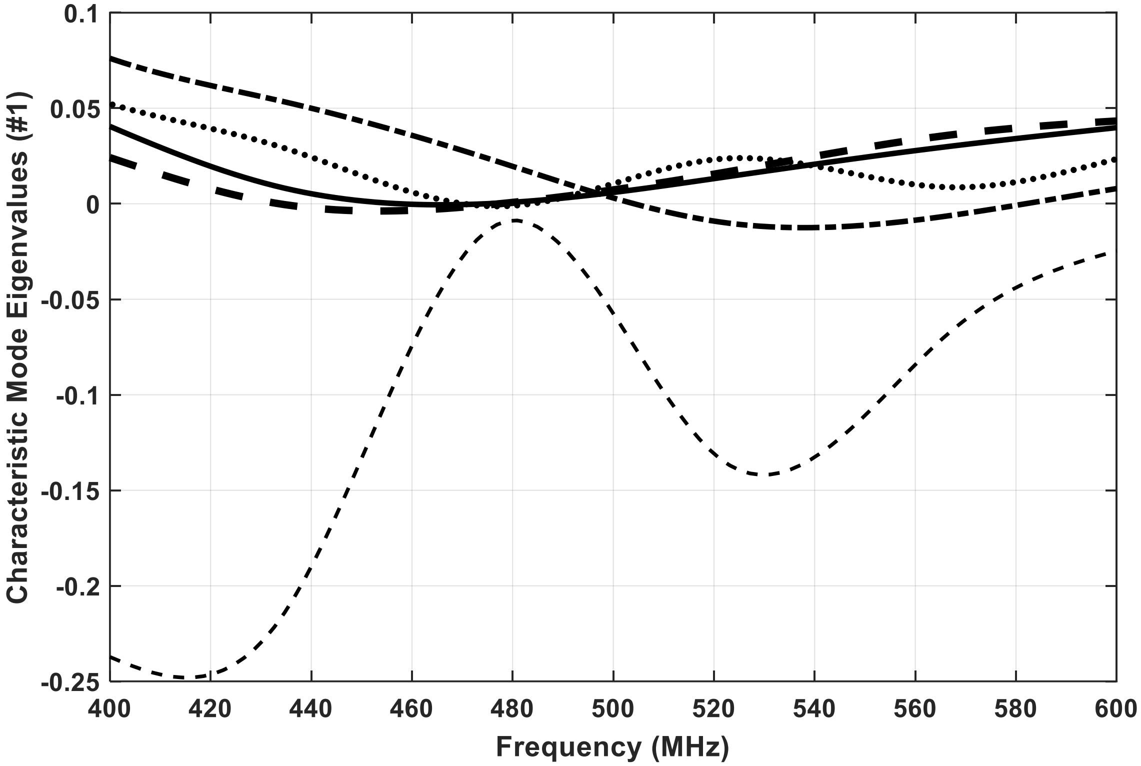

Fig.6.3-5 Eigenvalues (——) of the 1st sub-structure CM found using the MM/MM approach, and those (— —) using the hybrid MM/GTD approach (with all GTD terms included). Curve (• • •) is that with double diffraction terms removed, (▪▪▪▪) with corner diffraction contributions also removed, and (- - -) when the only GTD terms included are the direct and reflected ray terms.

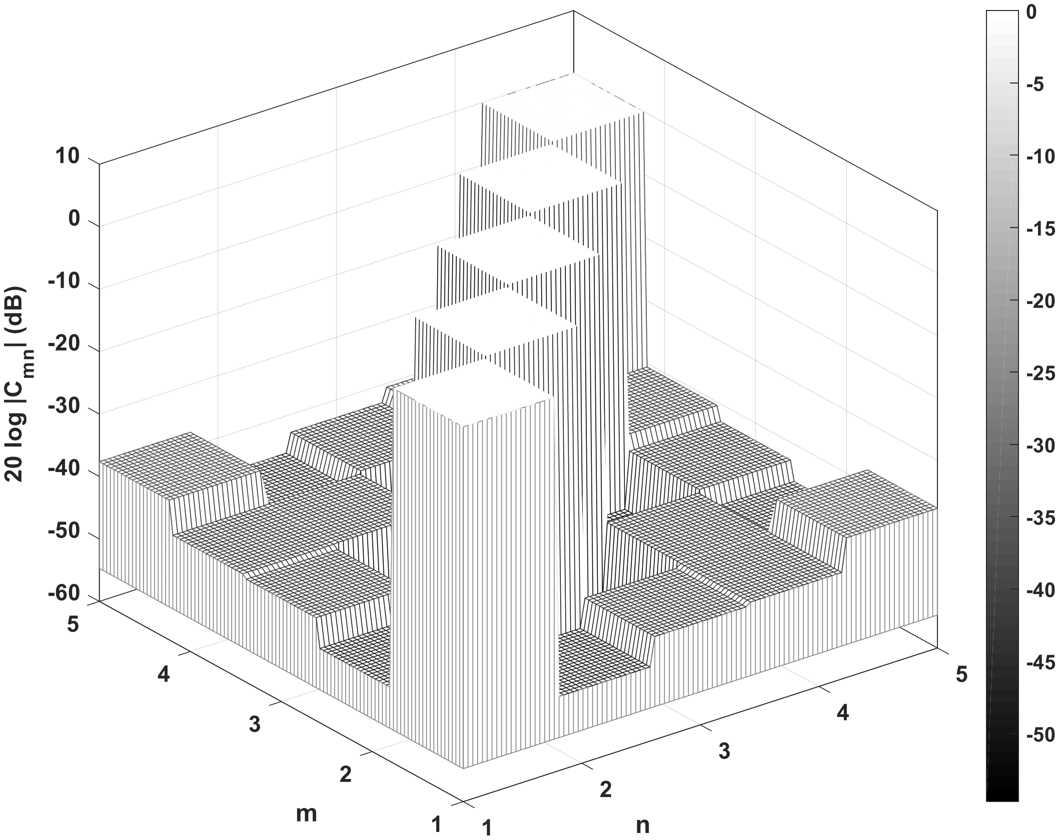

Fig.6.3-6 Magnitudes of the coupling coefficients expressed in deciBels ($20\log|C_{mn}|$) between the first five sub-structure CMs obtained when the hybrid MM/GTD approach is used to find $[Z^{\mathrm{per}}]$.

6.4 CONCLUSIONS

This chapter began with the puzzle of how to compute sub-structure CMs in a case where the antenna proper (to be shaped) is small, but the platform is electrically so large that meshing of the complete structure (radiator plus platform[118]) for sub-structure CM computation using a MM is computationally unfeasible. Essential to the solution of this problem was the important recognition, in Section 6.2, that sub-structure CMs can in fact be computed using field-based hybrid methods. Section 6.3 then confirmed, by application of this approach to an example, that it is indeed feasible to find the sub-structure CMs for some Object#A in the presence of Object#B using such an approach. This greatly extends the range of problems to which the shape synthesis methods, that are the subject of this thesis, can be applied, in a manner that has not yet been done by others.

---

[118] Object#A (radiator) plus Object#B (platform).

CHAPTER 7

General Conclusions

7.1 Contributions of the Thesis

The principal original contributions to antenna shape synthesis which have been presented in this thesis can be described as follows :

- At the start of this work only planar (1D) conducting surface antennas had been shape synthesized, either with the feed specified beforehand or using characteristic mode theory with the feed only needing to be specified after shaping. Using the work of Chapter 4, fully 3D conducting surface antennas can, and now have been, shape synthesized using characteristic mode theory with the feed only needing to be specified after shaping. Importantly, through definition of the starting geometry, the antennas can be constrained to fit on, and exploit for their operation, some required shape. The starting geometry can also be selected so that the resulting antenna is favourable as regards fabrication by some chosen method. The presence of nearby objects, such as an enclosed battery or associated circuitry, can be accounted for in the shape synthesis. In addition to shaping being done to achieve a self-resonant antenna, additional terms can be added to the objective function to obtain radiation patterns favourable in an expected wireless environment, as long as these expectations can be expressed in terms of characteristic mode quantities.

- In Chapter 5, the characteristic mode based shape synthesis procedure was extended to apply to the design of two closely-spaced antennas operating at different frequencies.

- Previously, if sub-structure modes were needed for antenna located in the vicinity of some platform structure, and sub-structure characteristic modes were needed, the platform had to be small enough (electrically) for method of moment meshing/modelling of the complete structure (antenna + platform) to be computationally feasible. With the work of Chapter 6 such sub-structure characteristic modes can now be computed for platforms of any electrical size as long as geometrical-theory-of-diffraction (GTD) modelling of the platform, and moment-method (MM) modelling of the antenna proper, is possible. We recognise that such use of the field-based hybrid MM/GTD approach to sub-structure characteristic modes computation could be inferred from the basic idea of a sub-structure mode. However, this does not yet appear to have been explicitly stated elsewhere (and so perhaps not realised), nor example computations provided. We believe this realisation might widen the scope of application of characteristic mode analysis. The use (as done here) of asymptotic methods as part of the procedure to find useful sets of characteristic modes can be viewed as one end of a classification scale in terms of which that in [SCHU 75], in which the entire object is electrically very small, lies at the opposite end.

■ The implementation of the shaping tool itself, in Chapter 3, apart from being needed to validate the shaping process, is a contribution in its own right. It has purposefully been fully implemented using commercially available software for the computational electromagnetics modelling and the optimization algorithm, and so can benefit from improvements therein. It allows the shaping prescription (eg. use of different objective functions; designation of portions of the starting geometry that may not be altered during shaping) to be adapted to new requirements that may arise.

7.2 Possible Future Work

The following possible future work might prove fruitful by exploiting more of what shaping tool synthesis has to offer:

- Apply it to antennas that have to occupy non-cuboid shapes.
- Implement the two different frequency / closely-spaced antenna technique when the two objects are mounted on an electrically large platform.

Preliminary portions of the work have been presented in two conference papers :

A.Alakhras and D.A.McNamara, "The shape optimisation of closely-spaced electrically-small antennas", *IEEE Int. Antennas & Propagat. Symp. Digest*, San Diego, USA, July 2017.

A.Alakhras and D.A.McNamara, "Further observations on the shape synthesis of closely-spaced antennas using sub-structure characteristic modes", *IEEE Int. Antennas & Propagat. Symp. Digest*, Boston, USA, July 2018.

The following are in preparation for publication as journal letters :

A.Alakhras and D.A.McNamara, "Sub-structure characteristic mode computation utilizing field-based hybrid methods".

A.Alakhras and D.A.McNamara, "The shape synthesis of three-dimensional electrically-small conducting surface antennas".

A.Alakhras and D.A.McNamara, "The shape synthesis of closely-spaced electrically-small conducting surface antennas operating at different frequencies".

There remain some issues/cases whose investigation in the future might prove useful. These have already been outlined in Section 4.6 and Section 5.6.

REFERENCES

[ADAM11] J. Adams and J. Lewis, “Conformal printing of electrically small antennas on three-dimensional surfaces,” *Advanced Materials*, Wiley & sons, Inc., 23, pp.1335–1340, 2011.

[ADAM15] J. Adams and J. Bernhard, "3D-printed spherical dipole antenna integrated on small RF node," *Electronics Letters* Vol. 51 No. 9, pp. 661–662, 2015.

[ALRO14] H. Alroughani and D .McNamara, “On the classification of characteristic modes, and the extension of sub-structure modes to include penetrable material,” in Proc. ICEAA, pp.159-162, Aruba, 2014.

[ALRO 15] H.Alroughani, “Studying microstrip patch antennas using the theory of characteristic modes”, IEEE Int. Antennas Propagation Symposium Digest, Vancouver, Canada, July 2015, pp.1476-1477.

[ALRO16] H. Alroughani and D. McNamara, “On the orthogonality properties of sub-structure characteristic modes,” *Microwave & Optical Technology Letters*, Vol.58, No.2, pp.481-486, 2016.

[ALRO18] H. Alroughani and D. McNamara, “Sorting the characteristic modes of PEC objects not electrically small,” *European Conference Antennas Propagation* (EuCAP 2018), London, UK, 2018.

[ALTS02] E. Altshuler, "Electrically small self-resonant wire antennas optimized using a genetic algorithm," *IEEE Transactions on Antennas and Propagation*, vol. 50, no. 3, pp. 297-300, 2002.

[ANTO 10] E. Antonino-Daviu and M. Ferrando-Bataller, “Modal analysis and design of band-notched UWB planar monopole antennas”, *IEEE Transactions on Antennas and Propagation*, vol.58, no.5, pp.1457–1467, 2010.

[BAND69] W. Bandler, “Optimization methods for computer-aided design*,” IEEE Transactions on Microwave Theory and Techniques, vol. MTT-17*, 1969.

[BAND88] J. Bandler and S. Chen, "Circuit optimization the state of the art," *IEEE Transactions on Microwave Theory and Techniques*, vol. 36, no. 2, pp. 424-443, 1988.

[BERN 15] T.Bernabeu-Jiménez and F.Vico-Bondia, “A 60-GHz coplanar-waveguide-fed slot-coupled rectangular DRA design using the theory of characteristic modes, “ *9th European Conference* on Antennas and Propagation, Lisbon, Portugal, April 2015.

[BEST 05] S. Best, "Low Q electrically small linear and elliptical polarized spherical dipole antenna", *IEEE Transaction on Antennas Propagation*, vol.53, no.3, pp.1047-1053, March 2005.

[CAPE 17] M. Capek and L. Jelinek et al., “Validating the characteristic mode solvers”, *IEEE Transaction on Antennas Propagation*, vol.65, no.8, pp.4134-4145, 2017.

[CHAN 77] Y. Chang and R. Harrington, “A surface formulation for characteristic modes of material bodies,” *IEEE Transactions on Antennas and Propagation*, vol. 25, no. 6, pp 789 – 795, November 1977.

[CHEN12] Y.Chen and C.Wang, “Characteristic-mode-based improvement of circularly polarized U-slot and E-shaped patch antennas”, *IEEE Antennas Wireless Propagation Letters*, vol.11, pp 1474–1477, 2012.

[CHEN15a] Y. Chen and C. Wang, “HF band shipboard antenna design using characteristic modes”, *IEEE Transactions Antennas Propagation,* vol.63, no.3, pp.1004-1013, 2015.

[CHEN15b] Y. Chen and C. Wang, *Characteristic Modes, Theory and Applications in Antenna Engineering*, (Wiley, 2015). Chap.2

[CHOO05] H. Choo and H. Ling, "Design of electrically small wire antennas using a pareto genetic algorithm," *IEEE Transactions on Antennas and Propagation*, vol. 53, no. 3, pp. 1038-1046, 2005.

[COLL 19] B. Collins, “Practical application of small antennas in hardware platforms”, *IET Microwaves, Antennas & Propagation*, vol.13, no.11, pp.1883-1888, 2019.

[DAI 16] Q. Dai and H.Gan et al., “Large-scale characteristic mode analysis with fast multipole algorithms *IEEE Transactions on Antennas and Propagation*, vol.64, no.7, pp.2608–2616, 2016.

[DENG 16] C. Deng and S. Hum, “MIMO mobile handset antenna merging characteristic modes for increased bandwidth”, *IEEE Transactions on Antennas and Propagation,* vol.64, no.7, pp.2660–2667, 2016.

[DOUG 98] M. Douglas and M. Stuchly, “A planar diversity antenna for handheld PCS devices”, *IEEE Transaction Vehicular Technology*, vol.47, no.3, pp.747-754, Aug.1998.

[EKEL80] E. Ekelman and G. Thiele, "A hybrid technique for combining the Method of Moment treatment of wire antennas with the GTD for curved surfaces," *IEEE Transactions on Antennas and Propagation*, vol. 28, no. 6, pp. 831-839, 1980.

[EREN11] A. Erentok and O. Sigmund, "Topology optimization of sub-wavelength antennas," *IEEE Transactions on Antennas and Propagation*, vol. 59, no. 1, pp. 58-69, 2011.

[ETHI 08] J. Ethier and D. McNamara, “MIMO handheld antenna design approach using characteristic mode concepts”, *Microwave Optical Technology Letters*, vol.50, no.7, pp.1724–1727, 2008.

[ETHI 12] J. Ethier and D. McNamara, "A sub-structure characteristic mode concept for antenna shape synthesis," *Electronics Letters*, vol.48, no.9, 2012.

[ETHI14] J. Ethier and D. McNamara, “Antenna shape synthesis without prior specification of the feedpoint locations,” *IEEE Transactions Antennas Propagation*, vol.62, no.10, pp.4919-4934, 2014.

[FANT69] R. Fante, “Quality factor of general ideal antennas”, *IEEE Transactions on Antennas and Propagation*, vol. AP-17, no. 2, pp. 151 – 155, 1969.

[FEKO] *FEKO*, Altair (www.altair.com).

[GARB65] R. Garbacz, “Modal expansions for resonance scattering phenomena,” *Proceedings of the IEEE*, pp. 856 – 864, 1965.

[GLAZ 09] A. Glazunov and F.Tufvesson, “Mean effective gain of antenna in a wireless channel”, *IET Microwaves, Antennas & Propagation*, vol.3, no.2, pp.214-227, 2009.

[GOUD 17] S. Goudos, "Antenna design using binary differential evolution," *IEEE*

Antennas and Propagation Magazine, pp.74-93, Feb.2017.

[GRAG 97] R. Graglia and A. Peterson, "Higher order interpolatory vector bases for computational electromagnetics", *IEEE Transactions on Antennas and Propagation*, vol.45, no.3, pp.329-342, March 1997.

[GRIF 06] L. Griffiths and C. Chung, "Broadband and multiband antenna design using the genetic algorithm to create amorphous shapes using ellipses", *IEEE Transactions Antennas and Propagation*, vol.54, no.10, pp.2776 – 2782, 2006.

[HARR61] R. Harrington, *Time-Harmonic Electromagnetic Fields*, New York, McGraw-Hill, 1961.

[HARR71a] R. Harrington and J. Mautz, "Theory of characteristic modes for conducting bodies," *IEEE Transactions on Antennas and Propagation*, vol. 19, no. 5, pp. 622-628, 1971.

[HARR71b] R. Harrington and J. Mautz, "Computation of characteristic modes for conducting bodies," *IEEE Transactions on Antennas and Propagation*, vol. AP-19, no. 5, pp. 629 – 639, 1971.

[HARR72] R. Harrington and Y. Chang, "Characteristic modes for dielectric and magnetic bodies," *IEEE Transactions on Antennas and Propagation*, vol. AP-20, no. 2, pp. 194 – 198, 1972.

[HASS 14] E. Hassan and M. Berggren,"Topology optimization of metallic antennas", *IEEE Transactions on Antennas and Propagation*, vol.62, no.5, pp.2488-2500, May 2014.

[HUAN 08] Y. Huang and K. Boyle, *Antennas from Theory to Practice* (Wiley, 2008) pp.315-317.

[HUAN15] Y. Huang, "Radiation efficiency measurements of small antennas," *Handbook of Antenna Technologies*, 2015.

[JAKO 10] U. Jakobus, "Overview of hybrid methods in FEKO: Theory and applications", Proc. ICEAA, Sydney, Australia, pp.434-437, Sept.2010.

[JAKO 97] U. Jakobus and F. Landstorfer, "A combination of current- and ray-based techniques for the efficient analysis of electrically large scattering problems", *Applied Computational Electromagnetics Society*, Monterey, California, USA, pp 748-755, March 1997.

[JELI 18] L. Jelinek and M. Capek, "Radiation efficiency cost of resonance tuning", *IEEE Transactions on Antennas and Propagation*, vol.66, no.12, pp.6716-6723, Dec.2018.

[JOHN 90] W. Johnson and R. Sharpe, "Modeling scattering from and radiation by arbitrarily shaped objects with the electric field integral equation triangular surface patch code", *Electromagnetics*, vol.10, pp.41-63, 1990.

[JOHN97] J. Johnson and Y. Rahmat-Samii, "Genetic algorithms in engineering electromagnetics", *IEEE Transactions Antennas Propagation Magazine*, vol. 39, pp. 7-21, 1997.

[JOHN99a] J. Johnson and Y.Rahmat-Samii, "Genetic algorithms and method of moments (GA/MOM) for the design of integrated antennas", *IEEE Transactions on Antennas and Propagation*, vol.47, pp.1606-1614, 1999.

[JOHN99b] J. Johnson and Y. Rahmat-Samii, "Evolutionary designs of integrated antennas using genetic algorithms and method of moments (GA/MoM)", *Electromagnetic Optimization by Genetic Algorithms* (Wiley, 1999).

[KALL 02] K. Kalliola and P. Vainikainen, "Angular power distribution and mean effective gain of mobile antenna in different propagation environnments", *IEEE Transaction Vehicular Technology*, vol.51, no.5, pp.823-838, Sept. 2002.

[KILD 07] P. Kildal and C. Orlenius, "Multipath Techniques for Handset/Terminal Antennas", Chapter 58 in : J.L.Volakis (Edit.), *Antenna Engineering Handbook* (McGraw-Hill, 2007) 4th Edition.

[KISH 14] K. Kishor, and S. Hum, "A two-port chassis-mode MIMO antenna," *IEEE Antennas and Wireless Propagation Letters,* vol. 12, pp. 690-693, 2014.

[KRIS 16] G.Kristensson, *Scattering of Electromagnetic Waves by Obstacles* (SciTech Publ., 2016)

[KRUE09] C. Kruesi and M. Tentzeris, "Design and development of a novel 3-D cubic antenna for wireless sensor networks (WSNs) and RFID applications," *IEEE Transactions on Antennas and Propagation*, vol. 57, no. 10, pp. 3293-3299, 2009.

[LI 14] H. Li and B. K.Lau, "Design of orthogonal MIMO handset antennas based on characteristic mode manipulation at frequency bands below 1GHz", *IEEE Transactions on Antennas and Propagation*, vol.62, no.5, pp.2756–5766, 2014.

[LIND 99] D. Linden and E. Altshuler, "Design of wire antennas using genetic algorithms", Chapter 8 in : Y. Rahmat-Samii and E. Michielssen (Edits.), *Electromagnetic Optimization by Genetic Algorithms* (Wiley, 1999).

[LIU 16] H. Liu and M. Yan, "Electrically small loop antenna standing on compact ground in wireless sensor package," *IEEE Antennas and Wireless Propagation Letters*, vol. 15, pp. 76-79, 2016.

[MART 11] R. Martens and D. Manteuffel, "Selective excitation of characteristic modes on small terminals," *Proceedings of the 5th European Conference on Antennas and Propagation*, Rome, pp. 2492-2496, 2011.

[MART 16] R. Martens and D. Manteuffel, "Compact multimode multielement antenna for indoor UWB massive MIMO", *IEEE Transactions on Antennas and Propagation*, vol.64, no.7, pp.2689–2697, 2016.

[MATLAB] MATLAB R2016b, Optimization Toolbox 7.5.

[MCNA 16] D.A.McNamara, *Course Notes for ELG7100 : The* Method of Moment *in Engineering Electromagnetics*, School of Electrical Engineering & Computer Science, University of Ottawa, Canada, 2016.

[MCNA 17] D.A.McNamara, *Course Notes for ELG4118 : Wave Propagation & Antennas*, School of Electrical Engineering & Computer Science, University of Ottawa, Canada, 2016.

[MEDG 91] L. Medgyesi-Mitschang and D.Wang, "Hybrid methods in computational electromagnetics - A review," *Computer Physics Communications*, vol.68, Issues 1–3, pp.76-94,1991.

[MIER 13] Z. Miers and B. Lau, "Design of bandwidth-enhanced and multiband MIMO antennas using characteristic modes," *IEEE Antennas and Wireless Propagation Letters, vol. 12, pp. 1696-1699*, 2013.

[MIRH16] S. Mirhadi and M. Soleimani, "Ultra wideband antenna design using discrete Green's functions in conjunction with binary particle swarm optimisation," *IET Microwaves, Antennas & Propagation*, vol. 10, no.2, pp.184-192, 2016.

[MITC99] M. Mitchell, *"An Introduction to Genetic Algorithms* ", 1999.

[NASS 12] I.T.Nassar and T.M.Weller, "Development of novel 3-D cube antenna for compact wireless sensor nodes", *IEEE Transactions on Antennas and Propagation*, vol.60, no.2, pp.1059-1065, Feb.2012.

[NEZA19] Z. Nezami and K. Zamanifar, "Internet of everything: structure and ingredients," *IEEE Potentials*, vol.38, no.2, pp.12-17, March/April 2019.

[OLIV12] G. Oliveri and A. Massa, "Differential evolution as applied to electromagnetics: Advances, comparisons, and applications," *European Conference on Antennas and Propagation*, Prague, pp. 3058-3059, 2012.

[OUTW 17] J.M.Outwater and J.T.Bernhard, "Using machine learning techniques to analyze characteristic mode data of electrically large structures", *National Radio Science Meeting*, San Diego, USA, July 2017.

[PAKN16] R.Paknys, *Applied Frequency-Domain Electromagnetics* (Wiley, 2016) Chapter 8.

[PEDE 97] K.I.Pedersen, P.E.Mogensen and B.H.Fleury, "Power azimuth spectrum in outdoor environments", *Electronics Letters*, vol.33, no.18, pp.1583-1584, Aug.1997.

[PETE 97] A.Peterson, S.Ray and R.Mittra, *Computational Methods for Electromagnetics* (IEEE Press, 1997).

[POPO 81] B. Popovic, "Electromagnetic field theorems", *IEE Proc*., vol.128, no.1, pp.47-63, Jan.1981.

[RAHM12] Y. Rahmat-Samii and H. Rajagopalan, "Nature-inspired optimization techniques in communication antenna designs," *Proceedings of the IEEE*, vol. 100, no. 7, pp. 2132-2144, 2012.

[RAO 82] S.M.Rao, D.R.Wilton and A.W.Glisson, "Electromagnetic scattering by surfaces of arbitrary shape", *IEEE Transactions on Antennas and Propagation*, vol.30, pp.409-418, May 1982.

[ROCC11] P. Rocca and A. Massa, "Differential evolution as applied to electromagnetics,*" IEEE Antennas and Propagation Magazine*, vol. 53, pp. 38-49, 2011.

[SALU18] M. Salucci, F.Robol, N.Anselmi, M.A.Hannan, P.Rocca, G.Olivieri, M.Donelli and A.Massa, "S-Band spline-shaped aperture-stacked patch antenna for air traffic control applications," *IEEE Transactions on Antennas and Propagation*, vol. 66, no. 8, pp. 4292-4297, 2018.

[SAUN 08] S.Saunders and A.Aragón-Zavala, "Antennas for Mobile Systems", Chap.24 in : C.A.Balanis (Edit.), *Modern Antenna Handbook* (Wiley, 2008).

[SCHU75] H. Schuman, *A Low-Frequency Expansion for the Characteristic Modes of Conducting Bodies*, PhD Dissertation, Syracuse University, USA, 1975.

[SU 18] Z. Su, K.Klionovski, R.M.Bilal and A. Shamim, "A dual band additively manufactured 3-d antenna on package with near-isotropic radiation pattern," *IEEE Transactions on Antennas and Propagation*, vol. 66, no.7, pp. 3295-3305, 2018.

[SHAR19] A. Sharif, "Low-cost inkjet-printed UHF RFID tag-based system for internet of things applications using characteristic modes," *IEEE Internet of Things Journal*, vol. 6, pp. 3962-3975, 2019.

[SIEV 12] D. Sievenpiper, "Experimental validation of performance limits and design guidelines for small antennas," *IEEE Transactions on Antennas and Propagation*, vol. 60, pp. 8-19, 2012.

[SINC 48] G.Sinclair, “Theory of models of electromagnetic systems”, Proc.IRE, Vol.36, pp.1364-1370, 1948.

[SU18] Z. Su, and A. Shamim, "A dual band additively manufactured 3-d antenna on package with near-isotropic radiation pattern," *IEEE Transactions on Antennas and Propagation*, vol. 66, pp. 3295-3305, 2018.

[TAGA 90] T.Taga, "Analysis for mean effective gain of mobile antennas in land mobile radio environments", *IEEE Transaction Vehicular Technology*, Vol.39, No.2, pp.117-131, May 1990.

[THER 00] I. Theron, and U. Jakobus, “Extensions to the hybrid method of moments / uniform GTD formulation for sources located close to a smooth surface”, *IEEE Transactions on Antennas and Propagation*,vol.48, no.6, pp.940-945, 2000.

[THOR05] B. Thors, and H. Holter, "Broadband fragmented aperture phased array element design using genetic algorithms", *IEEE Transactions Antennas propagate* vol. 53, pp. 3280-3287, 2005.

[TOIV 10] J. Toivanen and P. Ylä-Oijala, “Gradient-based shape optimization of ultra-wideband antennas parameterized using splines,” *IET Microwaves, Antennas & Propagation*, vol. 4, pp. 1406-1414, 2010.

[VOLA 12] J.Volakis and K.Sertel, *Integral Equation Methods for Electromagnetics* (SciTech Publ., 2012)

[VOLA 07] J.L.Volakis (Edit.), *Antenna Engineering Handbook* (McGraw-Hill, 2007) 4th Edition.

[WEIL97] D. Weile and E. Michielssen, "Genetic algorithm optimization applied to electromagnetics: a review," *IEEE Transactions on Antennas and Propagation*, vol. 45, pp. 343-353, 1997.

[WENG14] W. Weng and M. Chang, "Optimal design of a planar antenna using binary particle swarm optimization," *IEEE International Workshop on Electromagnetics*, Sapporo, pp. 68-69, 2014.

[WEST98] J. West and S. Ja, "Low-grazing scattering from breaking water waves using an impedance boundary MM/GTD approach," *IEEE Transactions on Antennas and Propagation*, vol. 46, pp. 93-100, 1998.

[WHEE47] H. Wheeler, “Fundamental limitations of small antennas”, *Proceedings of the IRE*, vol. 35, Issue 12, pp. 1479 – 1484, 1947.

[WHEE59] H. Wheeler, “The radian sphere around a small antenna”, *Proceedings of the IRE*, vol. 47, Issue 8, pp. 1325 – 1331, 1959.

[WHEE75] H. Wheeler,“Small antennas,” *IEEE Transactions Antennas Propagation*, vol. AP-23, pp. 462–469, 1975.

[XIAN 19] S.Xiang and B.K.Lau, “Preliminary study on differences between full- and sub-structure characteristic modes”, *IEEE Transactions on Antennas and Propagation*, pp. 1863-1864, Atlanta, USA, July 2019.

[XU14] L. Xu and S. Li, "Internet of things in industries: a survey," *IEEE Transactions on Industrial Informatics*, vol. 10, pp. 2233-2243, 2014.

[YAGH05] A. Yaghjian and S. Best, “Impedance, Bandwidth, and Q of antennas,” *IEEE Transactions on Antennas and Propagation*, vol. 53, pp. 1298 – 1324, 2005.

[YAMA09] T. Yamamoto and T. Tsukagoshi, "Efficient antenna miniaturization technique by cut off of chromosome-length in genetic algorithm," *Asia Pacific Microwave Conference*, Singapore, pp. 1837-1840, 2009.

[YAN 18] S. Yan and G. Vandenbosch, “Design of a dual-band wearable planar inverted f antenna based on characteristic mode theory”, *12th European Conf. Antennas Propagation*, London, UK, April 2018.

[YANG16a] B. Yang and J. Adams, “Systematic shape optimization of symmetric MIMO antennas using characteristic modes”, *IEEE Transactions on Antennas and Propagation*,, vol.64, pp.2668-2678, 2016.

[YANG16b] B. Yang and J. Adams, "A modal approach to shape synthesis and feed placement for planar MIMO antennas," *IEEE International Symposium on Antennas and Propagation*, Puerto Rico, pp. 15-16, 2016.

[YANG16c] B. Yang and J. Adams, "Computing and visualizing the input parameters of arbitrary planar antennas via eigenfunctions," *IEEE Transactions on Antennas and Propagation*, vol. 64, pp. 2707-2718, 2016.

[YANG16d] B. Yang and J. Adams, "Mode-based analytical models for arbitrary wire and planar antennas," *European Conference on Antennas and Propagation*, Davos, pp. 1-4, 2016.

[YANG19] B. Yang and J. Adams, "A shape-first, feed-next design approach for compact planar MIMO antennas," *Progress In Electromagnetics Research*, Vol. 77, 157–165, 2019.

APPENDIX A

Estimation of Measured Radiation Efficiency of the Shaped-Synthesized Open Cuboid Antenna of Section 4.2

As noted in Section 4.2.6 the computed radiation efficiency of $\eta_{rad}^{Computed} = 98.9\%$ is considered over-optimistic. It is relatively difficult to perform accurate measurements of the radiation efficiency of an antenna, and so a method of estimating a more realistic measurement was devised as follows. From Section 2.2.7 we know the partial directivity D_q, where q denotes either θ or ϕ, is related to the partial gain G_q though the radiation efficiency. We can write

$$G_q^{Measured} = \eta_{rad}^{Measured} D_q^{Measured}$$

and

$$G_q^{Computed} = \eta_{rad}^{Computed} D_q^{Computed}$$

It is well-known that, due to the fact that they are found using integrals of the current distribution, the far-zone fields are relatively insensitive to small details in the predicted antenna current distribution $\bar{J}_s$. The directivity is computed directly from these far zone fields, as outlined in Section 2.2.7, and so is also reliably predicted. There are only small changes in the predicted $\bar{J}_s$ between those cases where losses are included in the computation and when it is not. We therefore make the assumption that $D_q^{Measured} \approx D_q^{Computed}$.

If we take any point (θ_o, ϕ_o) on the radiation pattern, and compute $G_q^{Computed}(\theta_o, \phi_o)$, followed by a measurement $G_q^{Measured}(\theta_o, \phi_o)$, then we can use the above two expressions, and the assumption $D_q^{Measured}(\theta_o, \phi_o) \approx D_q^{Computed}(\theta_o, \phi_o)$, to write

$$\eta_{rad}^{Measured} \approx \left(\frac{G_q^{Measured}(\theta_o, \phi_o)}{G_q^{Computed}(\theta_o, \phi_o)} \right) \eta_{rad}^{Computed}$$

The pyramidal horn antenna used as a gain reference is the H-1734 broadband (0.5 GHz – 6.0 GHz) horn antenna supplied by Cobham. Although it is not a calibrated standard gain horn antenna, the nominal gains of this horn are as shown[119] in Fig.A-1. In the case in question, the computed partial ($\theta-\text{polarised}$) gain of the AUT in the selected azimuth direction was $G_{\theta}^{Computed} = -1.2\,\text{dBi}$, with the relative level on the VNA reading a value -50.8dB. We add the mismatch factor[120] of 0.05dB (determined from the computed $|\Gamma_{in}|$ of -22.7dB), to obtain a computed realised gain of $G_{\theta}^{Computed} = -1.16\,\text{dBi}$. When the AUT was substituted with the above-mentioned horn antenna, with its maximum pointed in the direction of the source antenna, the relative level on the VNA was -40.7dB. The difference in received power levels is thus 10.1dB. This implies the actual measured gain of the AUT is in fact 6.8dBi minus this 10.1dB, or in other words $G_{\theta}^{Measured} = -3.3\,\text{dBi}$. We correct this to a measured realized gain by adding the mismatch factor of 0.3dB (determined from the measured $|\Gamma_{in}|$ of -14.7dB) to obtain a measured realized gain $G_{\theta}^{Measured} = -3.0\,\text{dBi}$. It then follows that

$$\eta_{rad}^{Measured} \approx 10^{(-3.0+1.16)/10}\ \eta_{rad}^{Computed} = 0.66\ \eta_{rad}^{Computed} = 0.65$$

This is possibly a pessimistic estimate, but it at least bounds the radiation efficiency as $65\% < \eta_{rad} < 98.9\%$.

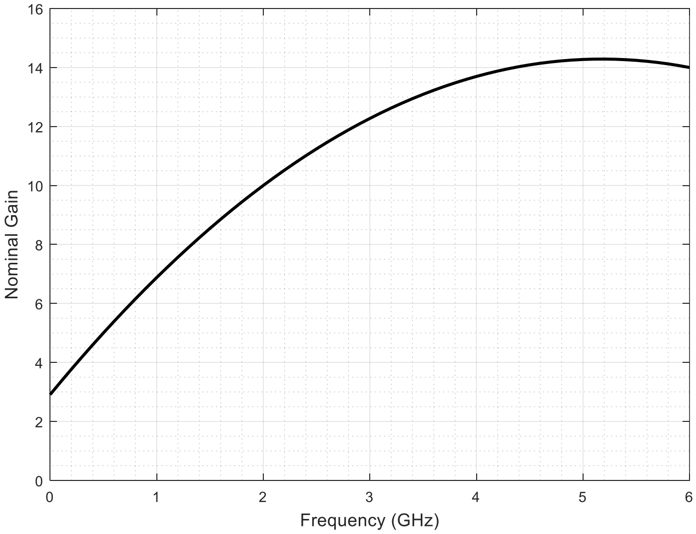

Fig.A-1 : Curve of the nominal gains (dBi) of the horn antenna used as a gain reference.

---

[119] Data accessed from www.cobham.com on 15 August 2019.

[120] The factor $1-|\Gamma_{in}|^2$.